

Supporting information on:

Subtle hydrogen bonds: Benchmarking with OH stretching fundamentals of vicinal diols in the gas phase

Beppo Hartwig^a, Martin A. Suhm^{a*}

a Institut für Physikalische Chemie, Georg-August-Universität Göttingen, Tammannstr. 6, 37077 Göttingen, Germany. E-mail: msuhm@gwdg.de

Contents

1	Experimental Parameters	1
2	Computational Details	2
2.1	Example Inputs	2
2.2	Energetic Comparison	3
2.2.1	$n_D = 0$: Primary-Primary	3
2.2.2	$n_D = 1$: Primary-Secondary	4
2.2.3	$n_D = 2$: Primary-Tertiary	6
2.2.4	$n_D = 2$: Secondary-Secondary	6
2.2.5	$n_D = 3$: Secondary-Tertiary	10
2.2.6	$n_D = 4$: Tertiary-Tertiary	11
2.3	Anharmonic Calculations	13
3	Correlation Plots	15
3.1	Assigned Correlation	15
3.2	M and M'	19
3.3	Error Evaluation	20
4	Assignments	22
4.1	Detailed Explanation	22
4.1.1	Methyl substitutions and model testing	22

4.1.2	Other hydrogen contacts (to π -clouds and F)	24
4.1.3	Cyclic systems	27
4.1.4	Fully substituted systems	30
4.2	List of Assignments	32
4.2.1	$n_D = 0$: Primary-Primary	32
4.2.2	$n_D = 1$: Primary-Secondary	32
4.2.3	$n_D = 2$: Primary-Tertiary	34
4.2.4	$n_D = 2$: Secondary-Secondary	35
4.2.5	$n_D = 3$: Secondary-Tertiary	37
4.2.6	$n_D = 4$: Tertiary-Tertiary	38
4.3	Fit Parameters	39
5	Structures	42
5.1	$n_D = 0$: Primary-Primary	42
5.2	$n_D = 1$: Primary-Secondary	42
5.3	$n_D = 2$: Primary-Tertiary	45
5.4	$n_D = 2$: Secondary-Secondary	45
5.5	$n_D = 3$: Secondary-Tertiary	48
5.6	$n_D = 4$: Tertiary-Tertiary	48
	References	51

1 Experimental Parameters

All experimental spectra (ASCII files) in the $3560 \text{ cm}^{-1} - 3700 \text{ cm}^{-1}$ wavenumber range are provided in Ref. [1].

Tab. S1: Overview of the experimental conditions of all shown spectra. T_S is the saturator temperature, T_N the nozzle temperature, d_N the distance of the laser from the nozzle, N the number of averaged exposures, t_{exp} the length of each exposure, p_B the backing pressure and Ar in He the fraction of argon in helium.

compound	T_S / K	T_N / K	d_N / mm	$N \times t_{\text{exp}}$ / min	p_B / bar	Ar in He / %
0-0 ^[2]	315	325	2.0	10×10	1.0	0
0-M	315	325	1.5	9×10	1.4	0
	315	325	1.5	10×10	1.4	6
	315	325	1.5	10×10	1.4	14
0-F	330	340	1.0	8×4	0.35	0
0-V	325	335	1.5	21×4	1.4	0
0-Ph	355	375	1.0	9×4	0.35	0
	355	375	1.0	11×4	0.35	15
	355	375	1.0	14×4	0.35	27
0-MM	315	325	1.25	12×4	1.0	0
rM-M	315	325	1.0	12×4	0.8	0
M-MM	315	325	0.75	5×3	0.35	0
MM-MM	300	300	1.5	12×12	1.2	0
t4-4	325	345	0.5	17×3	0.35	0
t5-5	350	360	1.5	15×4	1.4	0
t6-6 ^[2]	375	395	1.25	8×4	1.4	0
	375	395	1.25	10×4	1.4	2.5
	375	395	1.25	17×4	1.4	10
c6-6	355	370	1.25	7×4	1.4	0
	355	370	2.0	10×4	1.4	0
t7-7	355	375	1.5	12×4	1.4	0
CP-MM	325	345	1.0	7×4	0.35	0
CP-CP	395	415	1.0	8×4	0.35	0

2 Computational Details

2.1 Example Inputs

Tab. S2: Example inputs for the ORCA 4.2.1 calculations at the B3LYP level of computation. For BP86 and PBE the RI-J approximation was used for the analytical frequency calculations. The numerical frequency calculations are used to compute the Raman activities, while the analytical frequencies are used for the comparison to the experimental spectra.

type of calculation	input
optimisation + analytical frequency calculation	!B3LYP D3BJ abc UseSym ma-def2-TZVP TightOpt TightSCF Freq Grid5 NoFinalGrid Mass2016 %method SymThresh 5.0e-2 end
optimisation + numerical frequency calculation	!B3LYP D3BJ abc UseSym RIJCOSX def2/J ma-def2-TZVP TightOpt TightSCF NumFreq Grid5 NoFinalGrid GridX4 Mass2016 %method SymThresh 5.0e-2 end %elprop Polar 1 end
nudged-elastic band scan	!NEB-CI B3LYP D3BJ abc ma-def2-TZVP TightSCF Grid5 NoFinalGrid Mass2016 %neb NEB_End_XYZFile "XXXX.xyz" SpringType DOF PerpSpring cosTan Tol_MaxF_CI 2.e-3 Tol_RMSF_CI 1.e-3 Tol_Scale 10.0 Local true Nimages 12 end
transition state optimisation	!B3LYP D3BJ abc ma-def2-TZVP SlowConv OptTS TightSCF Grid5 NoFinalGrid Freq Mass2016 %geom Calc_Hess true Recalc_Hess 3 end

2.2 Energetic Comparison

2.2.1 $n_D = 0$: Primary-Primary

Tab. S3: Comparison of our computational results for 0-0. Relative electronic energies (ΔE_{el}) and zero point corrected energies (ΔE_0) are given. All values are given in kJ mol^{-1} . Conformers highlighted in bold text are assigned in the experimental Raman data. A general overview of other computational data can be found in the ESI of Ref. [2]. The corresponding structures can be found in Fig. S22.

method	conformer		0-0	0-0'
	ΔE_{el}	ΔE_0		
BP86/maTZ	ΔE_{el}	0	0	0.13
	ΔE_0	0	0	0.49
PBE/maTZ	ΔE_{el}	0	0	0.15
	ΔE_0	0	0	0.49
PBE0/maTZ	ΔE_{el}	0	0	1.08
	ΔE_0	0	0	1.34
B3LYP/maTZ	ΔE_{el}	0	0	1.21
	ΔE_0	0	0	1.49

2.2.2 $n_D = 1$: Primary-Secondary

Tab. S4: Comparison of our computational data with those of Lockley *et al.*^[3], Lovas *et al.*^[4], Lomas and co-workers^[5,6], Kollipost^[7] and Arenas *et al.*^[8] for 0-M. The values given by Arenas *et al.* have been converted from cm^{-1} to kJ mol^{-1} . Relative electronic energies (ΔE_{el}) and zero point corrected energies (ΔE_0) are given. All values are given in kJ mol^{-1} . Conformers highlighted in bold text are assigned in the experimental Raman data. Lovas *et al.*^[4] experimentally observe the same conformers as we do while Arenas *et al.*^[8] are missing 0-Mb'. 0-Ma and 0-Mb were initially observed by Caminati^[9] and later extended by the global minimum structure 0-M by Lockley *et al.*^[3]. Our nomenclature corresponds to that used originally by Vazquez *et al.*^[10] in the following way: 0-M=tG'g, 0-Ma=gG't, 0-M'=g'G'g, 0-Ma'=gG'g', 0-Mb=g'Gt, 0-Mb'=g'Gg, 0-Mc=tGg' and 0-Mc'=gGg'. The corresponding structures can be found in Fig. S23.

conformer		0-M	0-Ma	0-M'	0-Ma'	0-Mb	0-Mb'	0-Mc	0-Mc'
method									
BP86/maTZ	ΔE_{el}	0.57	0.74	0	0.14	2.08	3.30	4.76	3.87
	ΔE_0	0.14	0.14	0	0.04	1.91	3.26	4.41	3.94
PBE/maTZ	ΔE_{el}	0.54	0.85	0	0.30	2.39	3.69	5.07	4.30
	ΔE_0	0.13	0.23	0	0.17	2.22	3.63	4.72	4.36
PBE0/maTZ	ΔE_{el}	0	0.34	0.42	0.78	1.88	3.84	4.28	4.58
	ΔE_0	0	0.17	0.77	1.01	2.16	4.19	4.33	4.99
B3LYP/maTZ	ΔE_{el}	0	0.34	0.53	1.10	1.94	3.84	4.18	4.60
	ΔE_0	0	0.22	0.90	1.40	2.23	4.20	4.22	5.04
HF/6-31G ^[3]	ΔE_{el}	0	0.79	4.68	-	2.21	7.34	4.16	8.57
PBE0/6-311+G(d,p) ^[5]	ΔE_0	0	0.36	1.08	1.62	2.09	4.37	-	-
PBE0/6-311+G(d,p) ^[6]	ΔE_0	0	0.17	1.29	1.75	2.47	4.79	4.38	5.86
B3LYP-D3(BJ)/6-311+G(2d,p) ^[7]	ΔE_{el}	0	0.3	0.4	0.9	1.8	-	3.9	-
	ΔE_0	0	0.1	0.7	1.3	2.1	-	4.0	-
MP2/6-311++G** ^[3]	ΔE_{el}	0	0.87	-	-	1.85	-	-	-
MP2/aVTZ ^[4]	ΔE_0	0	0.89	1.37	2.75	2.54	4.49	4.17	5.75
MP2/aVTZ ^[8]	ΔE_0	0	1.00	1.04	2.55	2.30	-	4.04	-

Tab. S5: Comparison of our computational data for 0-F. Relative electronic energies (ΔE_{el}) and zero point corrected energies (ΔE_0) are given. All values are given in kJ mol^{-1} . Conformers highlighted in bold text are assigned in the experimental Raman data. The corresponding structures can be found in Fig. S24.

conformer		0-F'	0-F	0-Fa'	0-Fa	0-Fb	0-Fc
method							
BP86/maTZ	ΔE_{el}	0	3.62	5.88	8.55	9.53	9.00
	ΔE_0	0	2.26	4.80	6.99	7.83	7.62
PBE/maTZ	ΔE_{el}	0	3.38	5.73	8.34	9.20	8.82
	ΔE_0	0	2.04	4.66	6.79	7.51	7.45
PBE0/maTZ	ΔE_{el}	0	2.36	5.81	7.38	7.61	7.56
	ΔE_0	0	1.11	4.74	5.94	5.91	6.17
B3LYP/maTZ	ΔE_{el}	0	1.99	5.72	7.19	7.61	7.52
	ΔE_0	0	0.78	4.70	5.76	5.88	6.09

Tab. S6: Comparison of our computational data for 0-V. Relative electronic energies (ΔE_{el}) and zero point corrected energies (ΔE_0) are given. All values are given in kJ mol^{-1} . Conformers highlighted in bold text are assigned in the experimental Raman data. The corresponding structures can be found in Fig. S25.

conformer		0-V	0-Va	0-Vb	0-V'	0-Vc	0-Va'	0-Vd	0-Vb'	0-Vc'
method										
BP86/maTZ	ΔE_{el}	0.93	2.26	1.91	0	5.25	3.31	6.51	4.55	6.40
	ΔE_0	0	1.30	1.36	0.19	4.22	2.56	5.19	4.00	6.34
PBE/maTZ	ΔE_{el}	0.46	1.76	1.68	0	4.44	2.68	5.93	3.78	6.16
	ΔE_0	0	1.25	1.59	0.62	3.89	2.40	5.10	3.71	6.54
PBE0/maTZ	ΔE_{el}	0.67	1.05	1.89	0	3.60	2.97	5.59	4.00	6.91
	ΔE_0	0	0.42	1.61	0.37	2.81	2.51	4.50	3.62	7.05
B3LYP/maTZ	ΔE_{el}	0	1.22	1.29	1.08	3.88	3.59	5.02	4.84	4.37
	ΔE_0	0	1.26	1.66	2.04	3.68	3.80	4.52	4.60	4.88

Tab. S7: Comparison of our computational data for 0-Ph with those of Lomas^[6]. The value marked with \dagger is for benzene as a solvent since in Lomas calculations this conformer was not found to be stable in the gas phase. Relative electronic energies (ΔE_{el}) and zero point corrected energies (ΔE_0) are given. All values are given in kJ mol^{-1} . Conformers highlighted in bold text are assigned in the experimental Raman data. The corresponding structures can be found in Fig. S26.

conformer		0-Ph	0-Pha	0-Ph'	0-Pha'	0-Phb	0-Phc	0-Phd	0-Phc
method									
BP86/maTZ	ΔE_{el}	0	4.10	3.02	1.19	5.00	5.58	5.45	
	ΔE_0	0	3.91	3.36	2.26	5.11	5.41	5.01	
PBE/maTZ	ΔE_{el}	0	3.81	2.78	1.85	5.38	6.29	5.55	
	ΔE_0	0	3.67	3.11	2.86	5.47	6.11	5.47	
PBE0/maTZ	ΔE_{el}	0	3.41	3.57	2.11	5.65	5.83	7.15	
	ΔE_0	0	3.23	3.81	3.11	5.77	5.66	6.01	
B3LYP/maTZ	ΔE_{el}	0	3.73	3.92	3.25	5.50	5.89	6.84	
	ΔE_0	0	3.46	4.08	4.22	5.60	5.74	5.75	
PBE0/6-311+G(d,p) ^[6]	ΔE_0	0	3.30	4.52	4.95	6.59	7.10	7.43 [†]	

2.2.3 $n_D = 2$: Primary-Tertiary

Tab. S8: Comparison of our computational results for 0-MM. 0-MM* converges to 0-MM for all functionals besides B3LYP. Relative electronic energies (ΔE_{el}) and zero point corrected energies (ΔE_0) are given. All values are given in kJ mol^{-1} . Conformers highlighted in bold text are assigned in the experimental Raman data. The corresponding structures can be found in Fig. S27.

method	conformer	0-MM	0-MM'	0-MMa	0-MMa'	0-MM*
	BP86/maTZ	ΔE_{el}	0.08	0	2.30	1.18
	ΔE_0	0	0.39	2.21	1.52	-
PBE/maTZ	ΔE_{el}	0.06	0	2.10	1.11	-
	ΔE_0	0	0.39	2.05	1.48	-
PBE0/maTZ	ΔE_{el}	0	0.76	1.73	1.76	-
	ΔE_0	0	1.19	1.72	2.15	-
B3LYP/maTZ	ΔE_{el}	0	0.89	1.53	1.69	3.63
	ΔE_0	0	1.30	1.47	2.08	3.00

2.2.4 $n_D = 2$: Secondary-Secondary

Tab. S9: Comparison of our computational results for t4-4. Relative electronic energies (ΔE_{el}) and zero point corrected energies (ΔE_0) are given. All values are given in kJ mol^{-1} . Conformers highlighted in bold text are assigned in the experimental Raman data. The corresponding structures can be found in Fig. S29.

method	conformer	t4-4	t4-4'	t4-4*	t4-4t	t4-4at	t4-4bt
	BP86/maTZ	ΔE_{el}	0.76	0	2.48	4.22	1.29
	ΔE_0	0.35	0	1.34	2.67	1.35	3.03
PBE/maTZ	ΔE_{el}	0.71	0	2.36	4.12	1.35	3.56
	ΔE_0	0.29	0	1.42	2.50	1.39	3.00
PBE0/maTZ	ΔE_{el}	0.17	0	2.36	4.12	1.35	3.66
	ΔE_0	0	0.20	1.56	2.64	1.88	3.31
B3LYP/maTZ	ΔE_{el}	0.01	0	2.04	3.64	2.05	3.72
	ΔE_0	0	0.41	1.39	2.47	2.48	3.55

Tab. S10: Comparison of our computational results for t5-5. Relative electronic energies (ΔE_{el}) and zero point corrected energies (ΔE_0) are given. All values are given in kJ mol^{-1} . Conformers highlighted in bold text are assigned in the experimental Raman data. The corresponding structures can be found in Fig. S30.

method	conformer	t5-5	t5-5'	t5-5t	t5-5at	t5-5bt	t5-5*	t5-5ct	t5-5dt
		BP86/maTZ	ΔE_{el}	0	0.07	2.25	2.19	3.50	3.72
	ΔE_0	0	0.33	1.72	1.51	2.67	2.46	3.38	5.06
PBE/maTZ	ΔE_{el}	0	0.12	2.94	2.88	4.18	3.70	4.81	7.02
	ΔE_0	0	0.38	2.40	2.16	3.37	2.49	4.17	5.89
PBE0/maTZ	ΔE_{el}	0	0.79	3.41	3.92	4.12	4.19	6.09	7.85
	ΔE_0	0	1.01	3.07	3.42	3.53	2.93	5.39	6.81
B3LYP/maTZ	ΔE_{el}	0	0.97	2.47	2.93	3.20	3.78	5.42	7.15
	ΔE_0	0	1.24	2.13	2.48	2.57	2.62	4.76	6.14

Tab. S11: Comparison of our computational results for t6-6 and those of Paoloni *et al.*^[11]. Relative electronic energies (ΔE_{el}) and harmonically (also for Ref. [11]) zero point corrected energies (ΔE_0) are given. All values are given in kJ mol^{-1} . Conformers highlighted in bold text are assigned in the experimental Raman data. A general overview of other computational data can be found in the ESI of Ref. [2]. The corresponding structures can be found in Fig. S31.

method	conformer	t6-6	t6-6'
		BP86/maTZ	ΔE_{el}
	ΔE_0	0.42	0
PBE/maTZ	ΔE_{el}	0.82	0
	ΔE_0	0.36	0
PBE0/maTZ	ΔE_{el}	0	0.07
	ΔE_0	0	0.47
B3LYP/maTZ	ΔE_{el}	0	0.31
	ΔE_0	0	0.75
B3LYP-D3(BJ)/jul-cc-pVDZ ^[11]	ΔE_{el}	0	0.31
	ΔE_0	0	0.72
B2PLYP-D3(BJ)/jun-cc-pVTZ ^[11]	ΔE_0	0	1.11

Tab. S12: Comparison of our computational results for c6-6 with those of Lomas^[6]. Relative electronic energies (ΔE_{el}) and zero point corrected energies (ΔE_0) are given. All values are given in kJ mol^{-1} . Conformers highlighted in bold text are assigned in the experimental Raman data. The corresponding structures can be found in Fig. S32.

method \ conformer		c6-6	c6-6'	c6-6a	c6-6a'
		BP86/maTZ	ΔE_{el}	0	0.88
	ΔE_0	0	1.07	2.79	2.59
PBE/maTZ	ΔE_{el}	0	0.94	3.13	2.77
	ΔE_0	0	1.12	2.88	2.91
PBE0/maTZ	ΔE_{el}	0	1.63	3.09	4.01
	ΔE_0	0	1.77	2.79	4.09
B3LYP/maTZ	ΔE_{el}	0	1.53	2.82	4.23
	ΔE_0	0	1.64	2.54	4.38
PBE0/6-311+G(d,p) ^[6]	ΔE_0	0	1.95	2.49	5.09

Tab. S13: Comparison of our computational results for t7-7. Relative electronic energies (ΔE_{el}) and zero point corrected energies (ΔE_0) are given. All values are given in kJ mol^{-1} . Conformers highlighted in bold text are assigned in the experimental Raman data. The corresponding structures can be found in Fig. S33.

method \ conformer		t7-7	t7-7'	t7-7a	t7-7b	t7-7c	t7-7a'	t7-7b'
		BP86/maTZ	ΔE_{el}	0.85	0	2.53	2.80	3.30
	ΔE_0	0.47	0	2.14	2.50	2.77	1.81	3.80
PBE/maTZ	ΔE_{el}	0.78	0	2.54	2.79	3.31	1.80	3.54
	ΔE_0	0.42	0	2.16	2.53	2.79	1.83	3.93
PBE0/maTZ	ΔE_{el}	0	0.14	1.92	2.30	2.61	2.22	4.61
	ΔE_0	0	0.42	1.90	2.47	2.47	2.62	5.30
B3LYP/maTZ	ΔE_{el}	0	0.38	1.81	1.82	2.57	2.02	4.88
	ΔE_0	0	0.71	1.79	1.98	2.43	2.43	5.55

Tab. S14: Comparison of our computational data with those of Wang *et al.*^[12], Jesus *et al.*^[13,14], Paul *et al.*^[15], Lomas^[6] and Paoloni *et al.*^[11] for rM-M. The values given by Paul *et al.* and Paoloni *et al.* have been converted from cm^{-1} to kJ mol^{-1} . The values marked with ‡ are saddle points at their respective level of computation. Relative electronic energies (ΔE_{el}) and harmonically (also for Ref. [11], where we find discrepancies between main text and supplementary information, we use the supplementary information) zero point corrected energies (ΔE_0) are given. All values are given in kJ mol^{-1} . Conformers highlighted in bold text are assigned in the experimental Raman data. The corresponding structures can be found in Fig. S28.

method \ conformer		rM-M	rM-M'	rM-Ma	rM-M*	rM-Ma'
BP86/maTZ	ΔE_{el}	1.35	0	4.19	5.97 [‡]	4.48
	ΔE_0	0.83	0	3.64	3.64 [‡]	4.15
PBE/maTZ	ΔE_{el}	1.30	0	4.26	5.93 [‡]	4.73
	ΔE_0	0.81	0	3.71	4.10 [‡]	4.41
PBE0/maTZ	ΔE_{el}	0.27	0	3.10	5.58 [‡]	4.44
	ΔE_0	0	0.16	2.73	3.90 [‡]	4.25
B3LYP/maTZ	ΔE_{el}	0	0.06	3.01	4.72	4.26
	ΔE_0	0	0.52	2.81	3.41	4.28
HF/6-311G ^[15]	ΔE_{el}	0	5.59	2.00	-	7.12
PBE0/6-311+G(d,p) ^[6]	ΔE_0	0	1.14	2.95	4.31 [‡]	4.83
B3LYP/6-31G* ^[12]	ΔE_{el}	1.79	2.96	0.42	3.03	0
B3LYP/6-311++G** ^[13,14]	ΔE_0	0	1.67	3.13	3.60 [‡]	5.10
B3LYP-D3(BJ)/jul-cc-pVDZ ^[11]	ΔE_{el}	0	0.19	3.56	4.47	4.74
	ΔE_0	0	0.54	3.04	3.67	4.33
B2PLYP-D3(BJ)/jun-cc-pVTZ ^[11]	ΔE_0	0	0.90	2.91	-	4.46
MP2/6-311++G** ^[14]	ΔE_0	0	2.07	2.86	4.21 [‡]	5.50
MP2/6-311++G** ^[15]	ΔE_{el}	0	1.40	2.87	-	5.89

2.2.5 $n_D = 3$: Secondary-Tertiary**Tab. S15:** Comparison of our computational results for M-MM. Relative electronic energies (ΔE_{el}) and zero point corrected energies (ΔE_0) are given. All values are given in kJ mol^{-1} . Conformers highlighted in bold text are assigned in the experimental Raman data. The corresponding structures can be found in Fig. S34.

conformer		M-MM	M-MM'	M-MMa	M-MMa'	M-MMb	M-MMc	M-MMb'
method								
BP86/maTZ	ΔE_{el}	0.65	0	3.35	1.53	3.39	4.51	4.07
	ΔE_0	0.16	0	2.8	1.55	3.01	3.94	3.91
PBE/maTZ	ΔE_{el}	0.60	0	3.26	1.57	3.13	4.45	4.03
	ΔE_0	0.16	0	2.74	1.60	2.77	3.86	3.88
PBE0/maTZ	ΔE_{el}	0	0.27	2.47	1.78	2.30	3.68	4.03
	ΔE_0	0	0.68	2.35	2.20	2.33	3.44	4.25
B3LYP/maTZ	ΔE_{el}	0	0.47	2.28	1.97	2.51	3.85	4.17
	ΔE_0	0	0.87	2.15	2.41	2.48	3.59	4.34

conformer		M-MMc'
method		
BP86/maTZ	ΔE_{el}	3.67
	ΔE_0	3.63
PBE/maTZ	ΔE_{el}	3.72
	ΔE_0	3.67
PBE0/maTZ	ΔE_{el}	3.83
	ΔE_0	4.14
B3LYP/maTZ	ΔE_{el}	4.20
	ΔE_0	4.47

2.2.6 $n_D = 4$: Tertiary-Tertiary

Tab. S16: Comparison of our computational results for MM-MM with those of Dahlqvist *et al.*^[16], Olschewski *et al.*^[17] and Lomas *et al.*^[18]. The values given by Lomas have been converted from kcal mol⁻¹ to kJ mol⁻¹ and those from Olschewski from cm⁻¹ to kJ mol⁻¹. Relative electronic energies (ΔE_{el}) and zero point corrected energies (ΔE_0) are given. All values are given in kJ mol⁻¹. Conformers highlighted in bold text are assigned in the experimental Raman data. The corresponding structures can be found in Fig. S35.

method \ conformer		MM-MM	MM-MM'
BP86/maTZ	ΔE_{el}	0.57	0
	ΔE_0	0.08	0
PBE/maTZ	ΔE_{el}	0.45	0
	ΔE_0	0	0.03
PBE0/maTZ	ΔE_{el}	0	1.08
	ΔE_0	0	0.96
B3LYP/maTZ	ΔE_{el}	0	0.67
	ΔE_0	0	1.16
HF/6-311G** ^[16]	ΔE_{el}	0	3.4
B3LYP/6-311++G** ^[17]	ΔE_{el}	0	0.60
PBE0/cc-pVTZ//B3LYP/6-311+G(d,p) ^[18]	ΔE_0	0	1.88
MP2/6-311G** ^[16]	ΔE_{el}	0	3.4

Tab. S17: Comparison of our computational results for CP-MM. Relative electronic energies (ΔE_{el}) and zero point corrected energies (ΔE_0) are given. All values are given in kJ mol^{-1} . Conformers highlighted in bold text are assigned in the experimental Raman data. The corresponding structures can be found in Fig. S36.

conformer		CP-MM	CP-MM'	CP-MMa	CP-MMb	CP-MMa'	CP-MMb'
method							
BP86/maTZ	ΔE_{el}	1.22	0	1.76	1.73	0.60	1.88
	ΔE_0	0.59	0	1.17	1.17	0.51	1.59
PBE/maTZ	ΔE_{el}	1.11	0	1.87	1.93	0.83	2.02
	ΔE_0	0.48	0	1.26	1.34	0.71	1.72
PBE0/maTZ	ΔE_{el}	0.41	0	1.04	1.32	0.97	1.80
	ΔE_0	0	0.21	0.69	1.02	1.07	1.77
B3LYP/maTZ	ΔE_{el}	0.13	0	0.75	1.24	0.97	1.44
	ΔE_0	0	0.49	0.65	1.26	1.35	1.68

conformer		CP-MMc	CP-MMt	CP-MMat	CP-MMbt	CP-MMct
method						
BP86/maTZ	ΔE_{el}	3.81	8.63	9.58	7.14	7.47
	ΔE_0	2.99	6.51	7.00	5.95	5.84
PBE/maTZ	ΔE_{el}	3.80	8.23	9.06	7.56	7.37
	ΔE_0	2.99	6.14	6.53	5.79	5.72
PBE0/maTZ	ΔE_{el}	3.30	6.97	7.66	6.87	6.97
	ΔE_0	2.65	5.21	5.35	5.40	5.53
B3LYP/maTZ	ΔE_{el}	3.15	6.23	7.07	6.26	6.33
	ΔE_0	2.81	4.80	5.06	5.10	5.20

Tab. S18: Comparison of our computational results for CP-CP. The values marked with ‡ correspond to a transition state. Relative electronic energies (ΔE_{el}) and zero point corrected energies (ΔE_0) are given. All values are given in kJ mol^{-1} . Conformers highlighted in bold text are assigned in the experimental Raman data. The corresponding structures can be found in Fig. S37.

conformer		CP-CP'	CP-CPa'	CP-CP	CP-CPa	CP-CPb'	CP-CPc'	CP-CPb
method								
BP86/maTZ	ΔE_{el}	0	1.41	3.44	4.24	2.96	3.47	5.74
	ΔE_0	0	1.14	2.46	3.25	2.53	3.22	4.52
PBE/maTZ	ΔE_{el}	0	1.38	3.44	4.07	3.05	3.69	5.73
	ΔE_0	0	1.12	2.46	3.11	2.64	3.37	4.54
PBE0/maTZ	ΔE_{el}	0	1.08	2.91	3.46	3.00	4.19 [‡]	5.02
	ΔE_0	0	0.79	1.96	2.41	2.56	3.80 [‡]	3.81
B3LYP/maTZ	ΔE_{el}	0	0.84	2.75	3.20	2.69	3.75	4.81
	ΔE_0	0	0.59	1.81	2.13	2.21	3.40	3.60

conformer		CP-CPc
method		
BP86/maTZ	ΔE_{el}	6.73
	ΔE_0	5.56
PBE/maTZ	ΔE_{el}	6.91
	ΔE_0	5.69
PBE0/maTZ	ΔE_{el}	6.46
	ΔE_0	5.26
B3LYP/maTZ	ΔE_{el}	5.93
	ΔE_0	4.76

2.3 Anharmonic Calculations

Tab. S19: Comparison of our experimental wavenumbers and the anharmonic calculations of Barone and co-workers^[11] for *trans*-cyclohexane-1,2-diol. $\tilde{\nu}_{\text{LM}}$ are based on a Local-Mode approach and $\tilde{\nu}_{\text{VPT2}}$ on Vibrational Perturbation Theory of Second Order. The Local-Mode approach was conducted at the B3LYP/TZVP level of theory while a composite scheme was used for VPT2 where the harmonic force fields are computed at the B2PLYP-D3(BJ)/jun-cc-pVTZ level and the anharmonic force fields are computed at the B3LYP-D3(BJ)/jul-cc-pVTZ level of theory. It should be noted that for XH stretching vibrations the PCM (polarizable continuum model) was not used. The differences of the anharmonic calculations ($\Delta\tilde{\nu}_{\text{LM}}/\Delta\tilde{\nu}_{\text{VPT2}}$) are also given. All values are given in cm^{-1} .

method		Jet-Raman ^[2]	$\tilde{\nu}_{\text{LM}}^{\text{[11]}}$	$ \Delta\tilde{\nu}_{\text{LM}} $	$\tilde{\nu}_{\text{VPT2}}^{\text{[11]}}$	$ \Delta\tilde{\nu}_{\text{VPT2}} $
conformer						
t6-6 ₁		3628	3620.2	7.8	3602.3	25.7
t6-6 ₂		3667	3660.5	6.5	3651.7	15.3
t6-6' ₁		3616	3603.4	12.6	3580.5	35.5
t6-6' ₂		3628	3622.5	5.5	3602.1	25.9

Tab. S20: Comparison of our experimental wavenumbers as well as FT-IR matrix^[14] results and the anharmonic calculations of Barone and co-workers^[11] for *rac*-butane-2,3-diol. $\tilde{\nu}_{\text{LM}}$ are based on a Local-Mode approach and $\tilde{\nu}_{\text{VPT2}}$ on Vibrational Perturbation Theory of Second Order. The Local-Mode approach was conducted at the B3LYP/TZVP level of theory while a composite scheme was used for VPT2 where the harmonic force fields are computed at the B2PLYP-D3(BJ)/jun-cc-pVTZ level and the anharmonic force fields are computed at the B3LYP-D3(BJ)/jul-cc-pVTZ level of theory. It should be noted that for XH stretching vibrations the PCM (polarizable continuum model) was not used. The differences of the anharmonic calculations ($\Delta\tilde{\nu}_{\text{LM}}/\Delta\tilde{\nu}_{\text{VPT2}}$) relative to the jet data are also given. All values are given in cm^{-1} . Our jet data also illustrate the importance of reliable reference data given that the matrix effects can be quite large and not uniform.

conformer \ method	Jet-Raman	FT-IR/Ar ^[14]	FT-IR/Xe ^[14]	$\tilde{\nu}_{\text{LM}}^{\text{[11]}}$	$ \Delta\tilde{\nu}_{\text{LM}} $	$\tilde{\nu}_{\text{VPT2}}^{\text{[11]}}$	$ \Delta\tilde{\nu}_{\text{VPT2}} $
rM-M ₁	3622	3607	3597	3555.4	66.6	3600.3	21.7
rM-M ₂	3673	3657	3640	3664.8	8.2	3652.4	20.6
rM-M' ₁	3607	-	-	3520.1	86.9	3571.5	35.5
rM-M' ₂	3630	-	-	3578.9	51.1	3603.7	26.3
rM-Ma ₁	3610	3602	3587	3548.7	61.3	3585.0	25.0
rM-Ma ₂	3673	3654	3633	3641.8	31.2	3655.2	17.5
rM-M ₁ [*]	-	-	-	-	-	-	-
rM-M ₂ [*]	-	-	-	-	-	-	-
rM-Ma' ₁	3598	-	-	3515.9	82.1	3583.2	14.8
rM-Ma' ₂	3661	-	-	3647.1	13.9	3649.9	11.1

Tab. S21: Results of a VPT2^[19] calculation for the t5-5 conformer with GAUSSIAN16 (REVISION A.03)^[20] at the B3LYP-D3(BJ)/def2-TZVP level of computation. ω_i are the respective calculated harmonic frequencies, $\tilde{\nu}_i$ the anharmonic frequencies and $x_{i,44}$ the coupling constants for the bound OH mode and $x_{i,45}$ the ones for the free OH mode. Modes 18 – 32 are ring breathing vibrations. Significant off-diagonal constants may indicate spectrally identifiable hot transitions, if the coupling mode remains thermally populated in the jet. It should be kept in mind that a nozzle temperature of 360 K (see Tab. S1) provides an upper limit of about 2% for the involvement of such hot bands.

mode	18	19	21	23	29	32	44	45
$\omega_i / \text{cm}^{-1}$	1075.236	1110.600	1173.130	1235.281	1356.468	1438.726	3783.942	3813.614
$\tilde{\nu}_i / \text{cm}^{-1}$	1050.540	1082.496	1149.484	1205.165	1322.233	1401.172	3605.346	3635.292
$x_{i,44} / \text{cm}^{-1}$	-1.657	0.012	-0.551	-1.211	-0.303	-0.917	-86.031	0.211
$x_{i,45} / \text{cm}^{-1}$	-2.930	-1.100	-1.581	-3.095	-1.833	-3.05	0.211	-85.567

3 Correlation Plots

3.1 Assigned Correlation

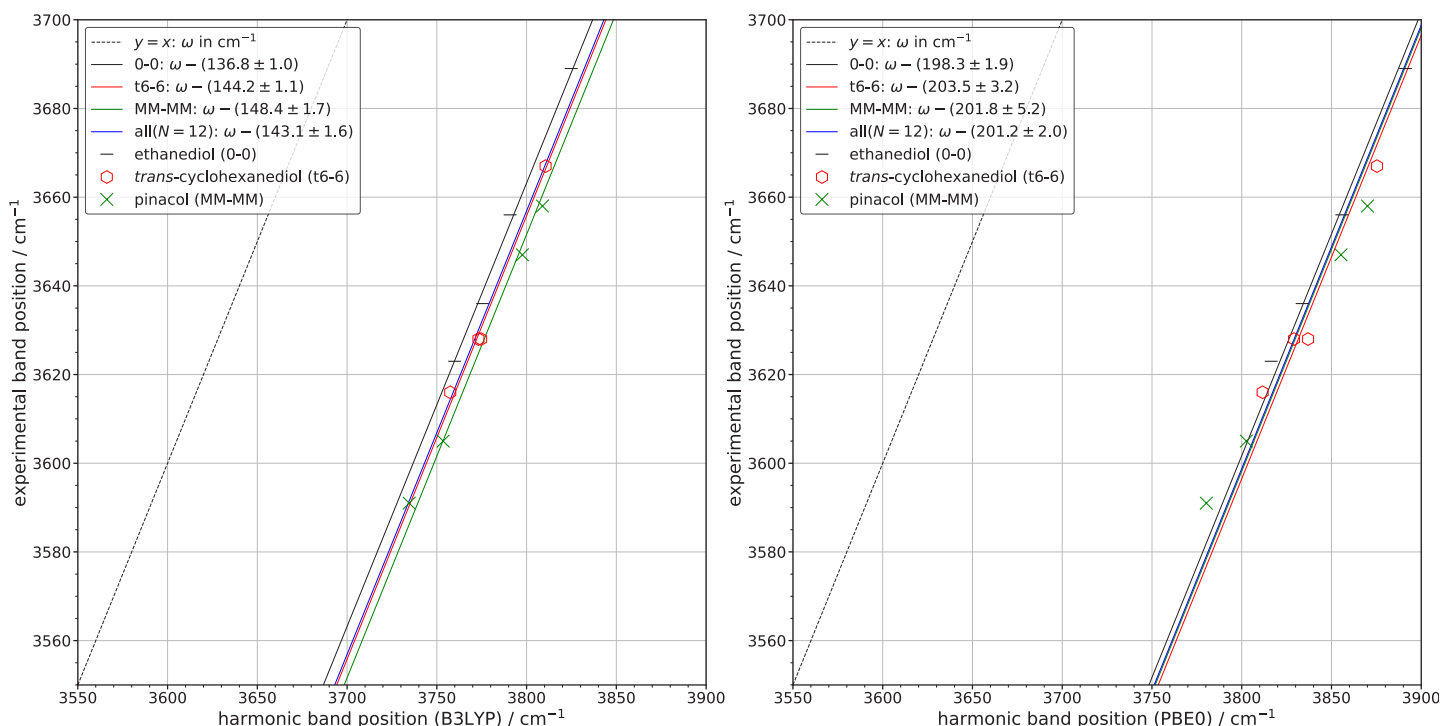


Fig. S1: Correlation plots comparing B3LYP (left) and PBE0 (right) assuming $h = 1$ in contrast to Fig. 5 of the main text discussing the assignments of three symmetrically substituted diols (section 4.2 of the main text). Differently shifted OH fundamentals are difficult to accommodate in a $h = 1$ model for PBE0.

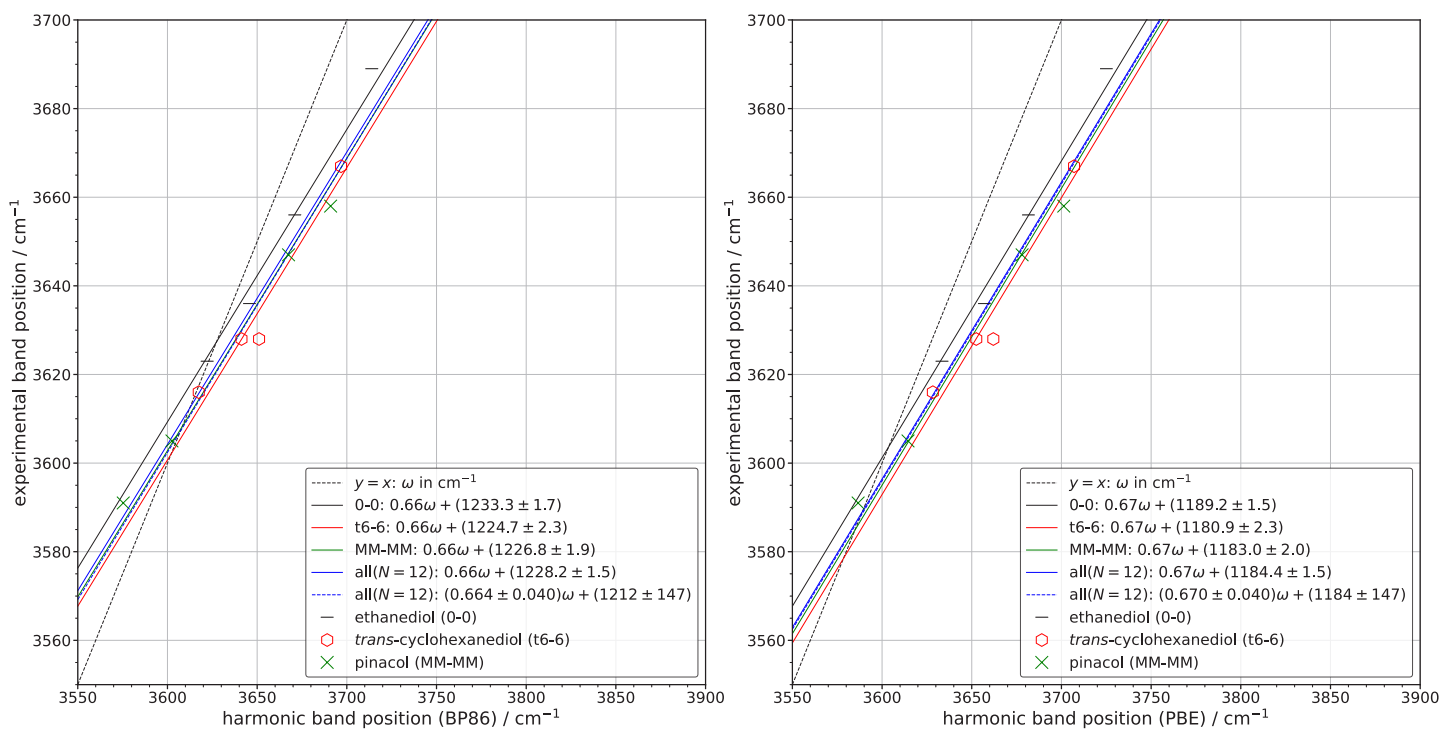


Fig. S2: Correlation plots comparing BP86 (left) and PBE (right) similar to Fig. 5 from the main text discussing the assignments of three symmetrically substituted diols (section 4.2 of the main text).

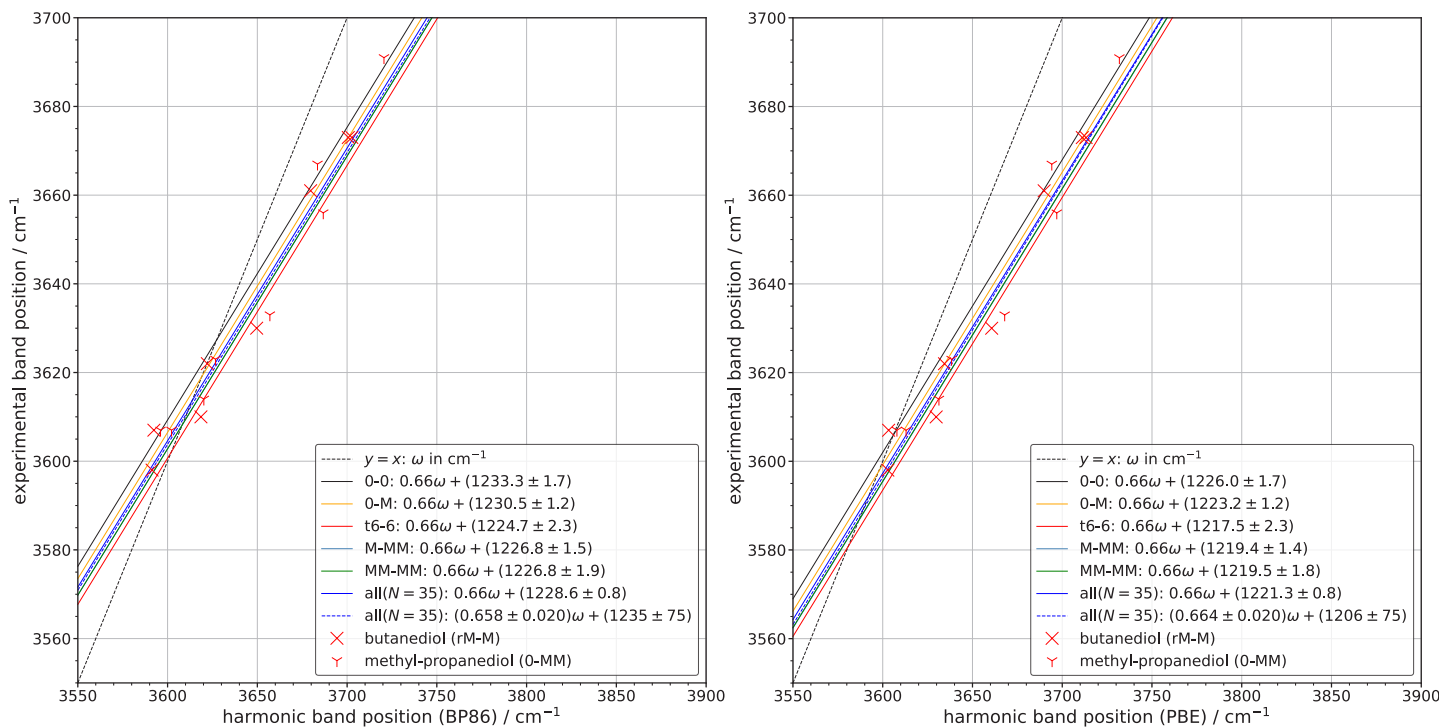


Fig. S3: Correlation plots comparing BP86 (left) and PBE (right) similar to Fig. 6 from the main text discussing a series of methyl substitutions (section 4.4 of the main text).

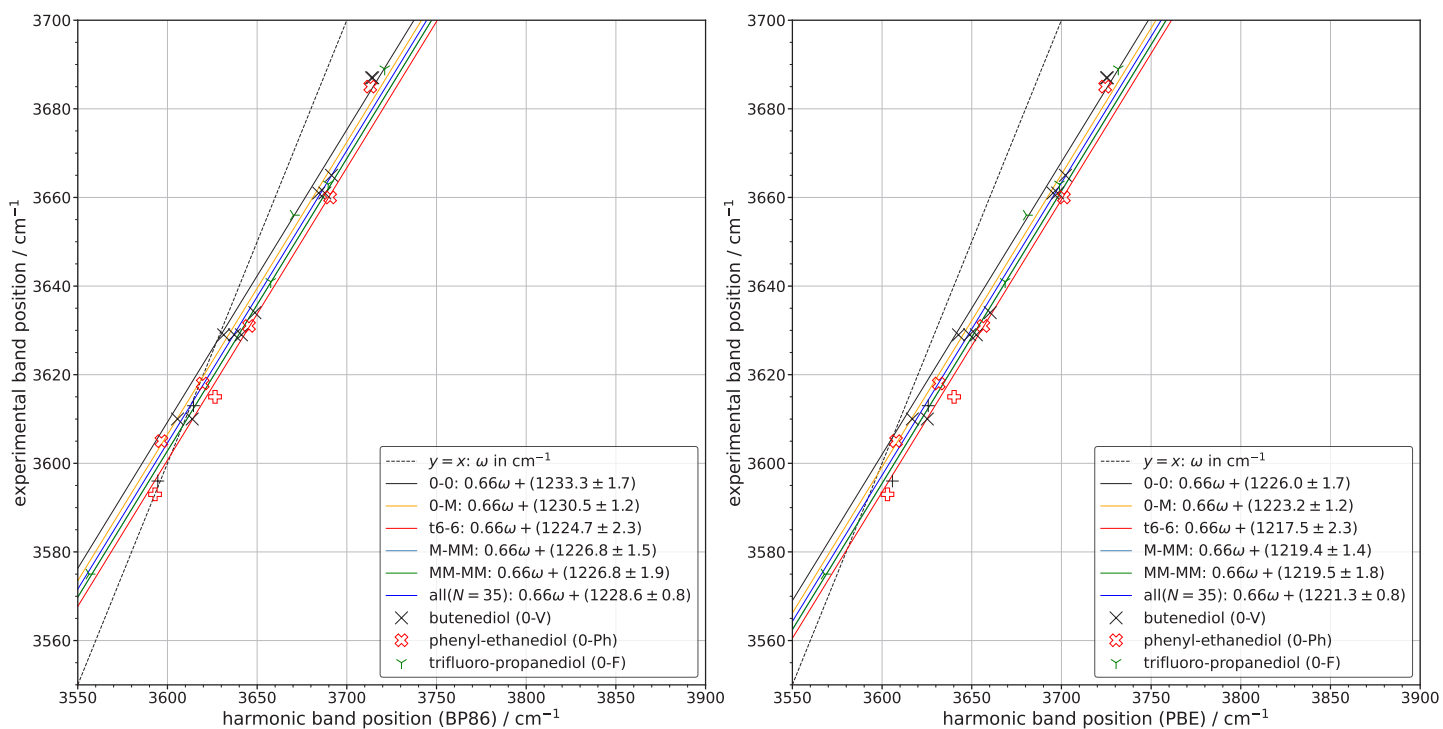


Fig. S4: Correlation plots comparing BP86 (left) and PBE (right) similar to Fig. 7 from the main text discussing systems with non oxygen hydrogen bond contacts (section 4.5 of the main text).

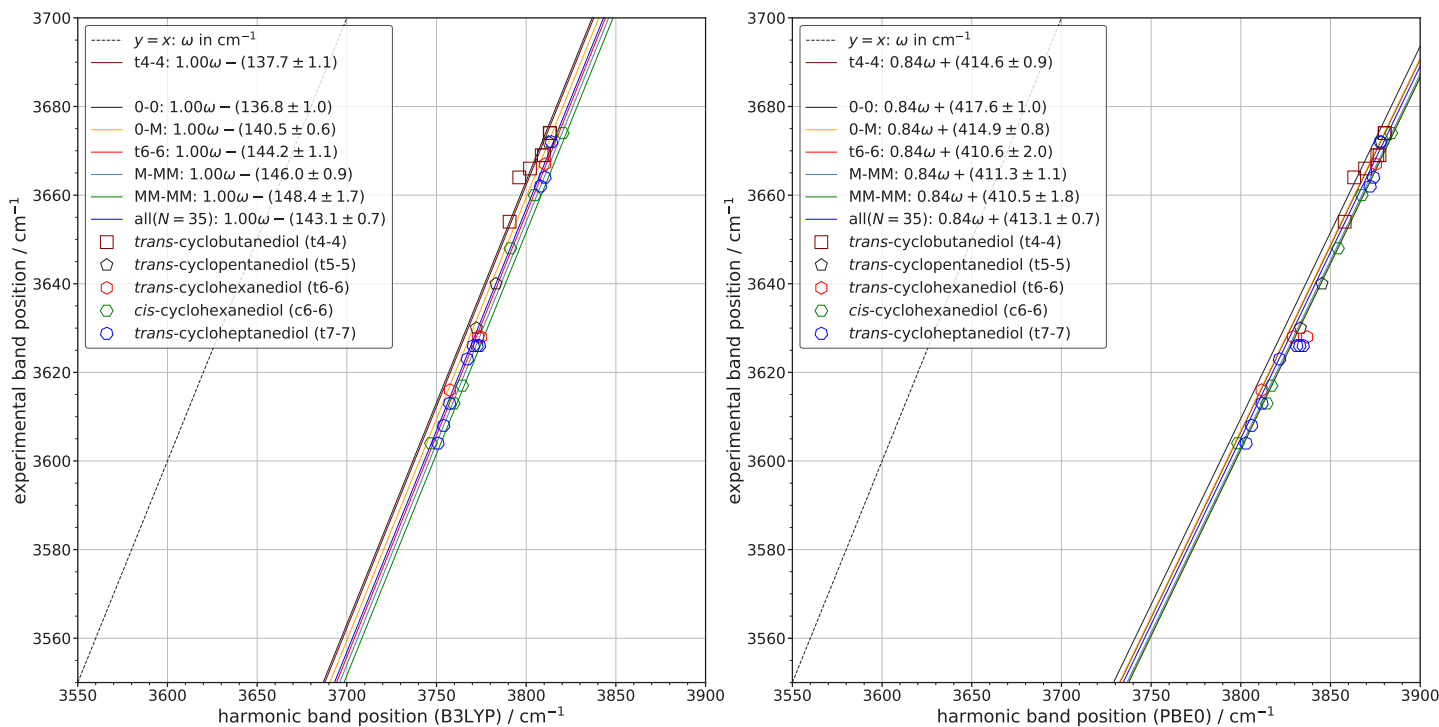


Fig. S5: Correlation plots comparing B3LYP (left) and PBE0 (right) discussing the assignments of the cyclic systems (section 4.6 of the main text).

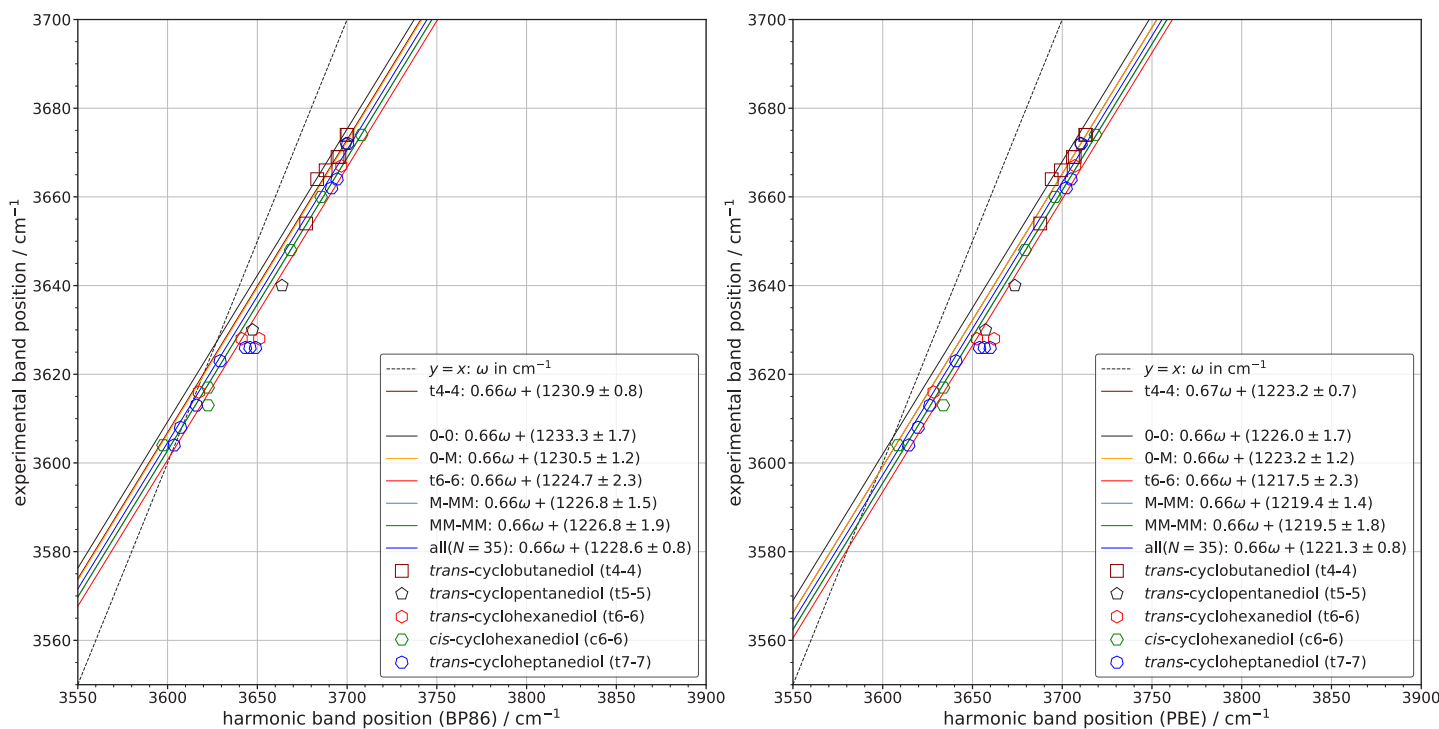


Fig. S6: Correlation plots comparing BP86 (left) and PBE (right) similar to Fig. S5 discussing the cyclic system (section 4.6 of the main text).

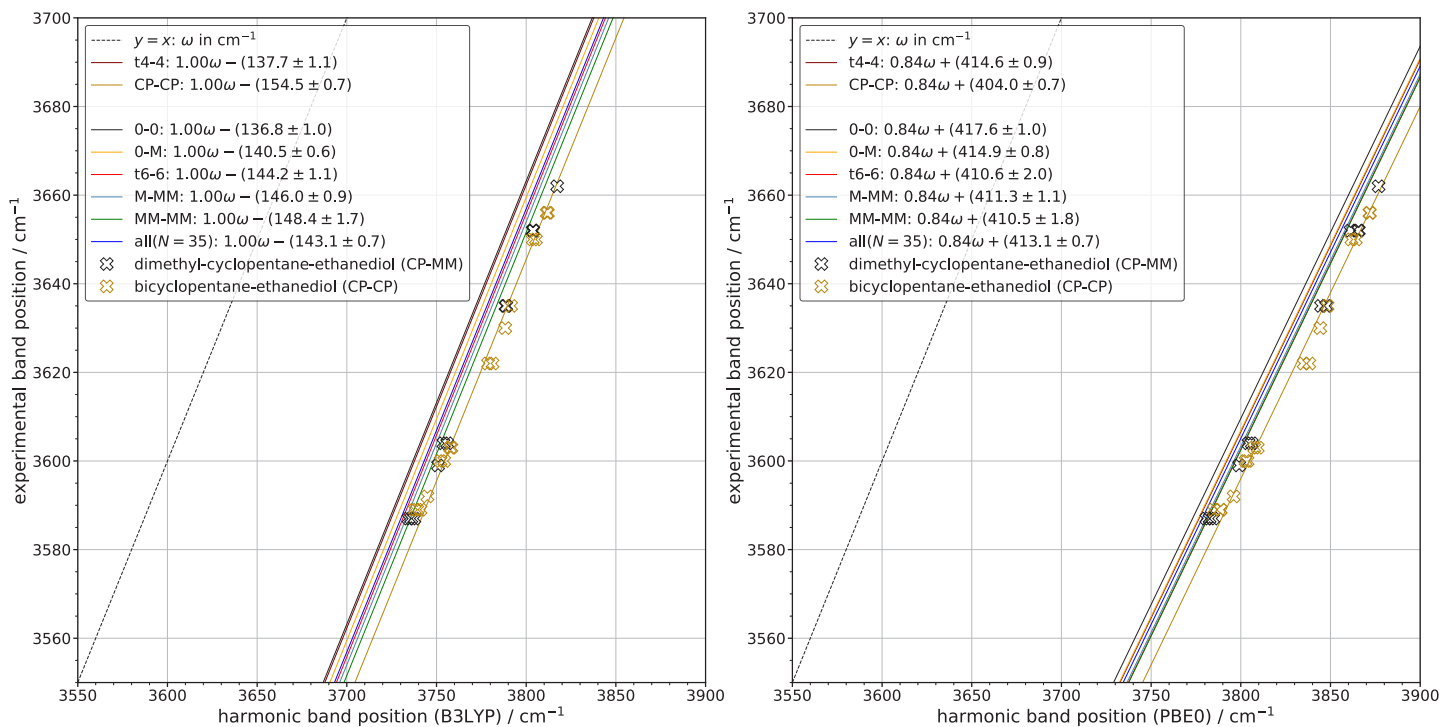


Fig. S7: Correlation plots comparing B3LYP (left) and PBE0 (right) discussing fully substituted systems (section 4.7 of the main text).

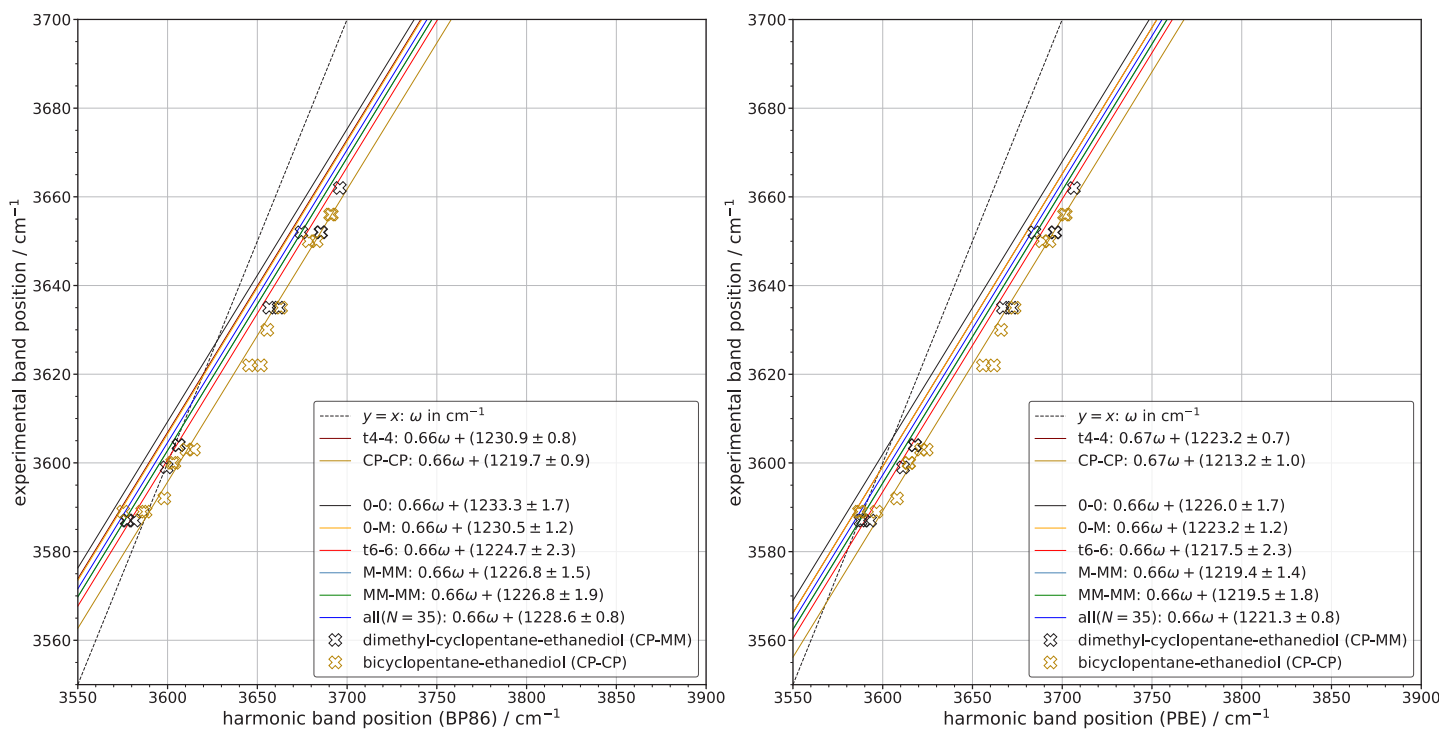


Fig. S8: Correlation plots comparing BP86 (left) and PBE (right) similar to Fig. S7 discussing fully substituted systems (section 4.7 of the main text).

3.2 M and M'

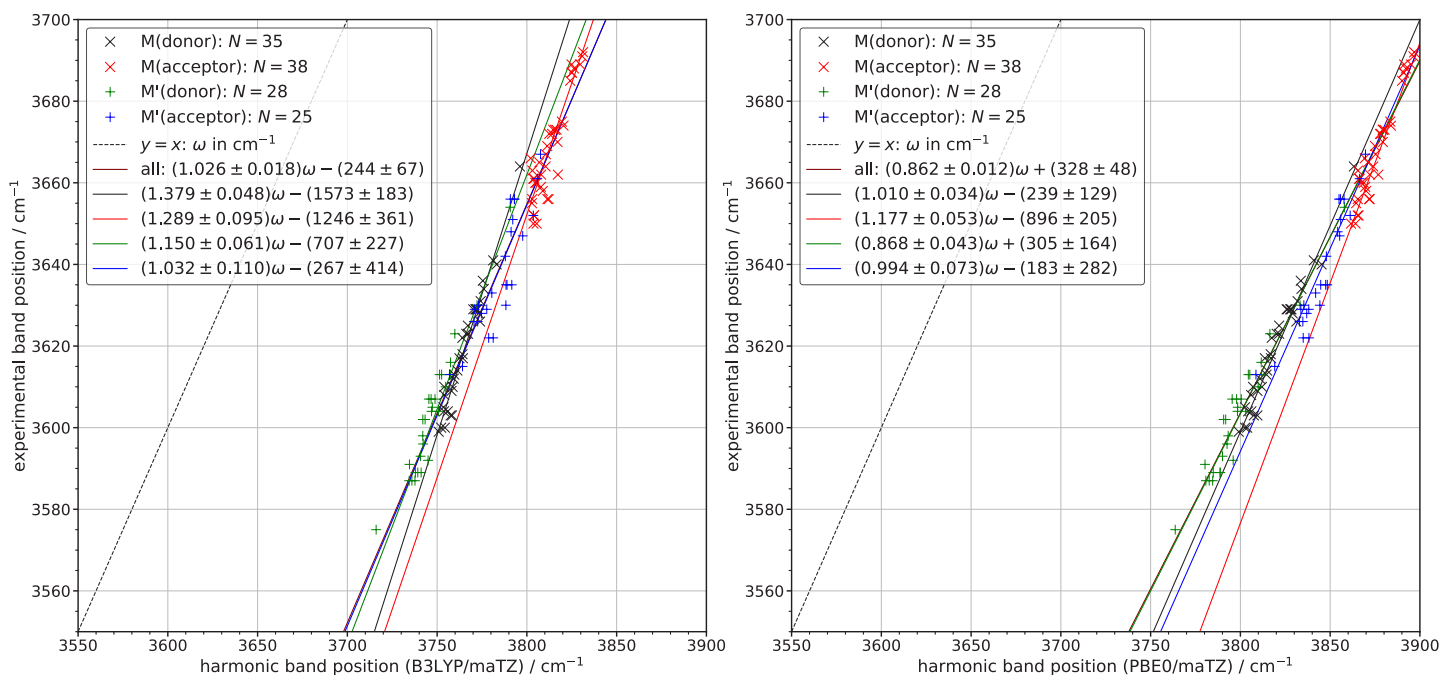


Fig. S9: Correlation plots of the primed hydrogen bond donors (green) and acceptors (blue) as well as the unprimed hydrogen bond donors (black) and acceptors (red) of conformers comparing B3LYP (left) and PBE0 (right). The plot shows the individual contributions to Fig. 30 of the main text. N indicates the number of bands for each sub class. 2-parameter fits with resulting large and correlated errors (σ) for each sub class are shown in their corresponding colour as well as an all fits in brown, hidden behind nearly coincident individual fits ($N = 126$). In case of B3LYP h is consistently above 1 and M conformers require a steeper slope than M' ones. Additionally, donors yield a larger h in their respective M and M' family. In case of PBE0 the opposite is found where acceptors yield higher h values than the corresponding donors. Furthermore, h is closer to 1 for PBE0 for the different sub classes than was the case for the all-fit of the main text ($h = 0.835$, see Fig. 10) as well as for an all fit for the 4 classes. It should be kept in mind that the all fit of the main text only involves bands of the training set ($N = 35$). As indicated by the errors, a division into sub classes is more helpful for PBE0. In case of PBE0, a more physical sign for a_2 is found except for M'(donor). For both functionals, higher h slopes are obtained for all sub class fits than for the all fit variant.

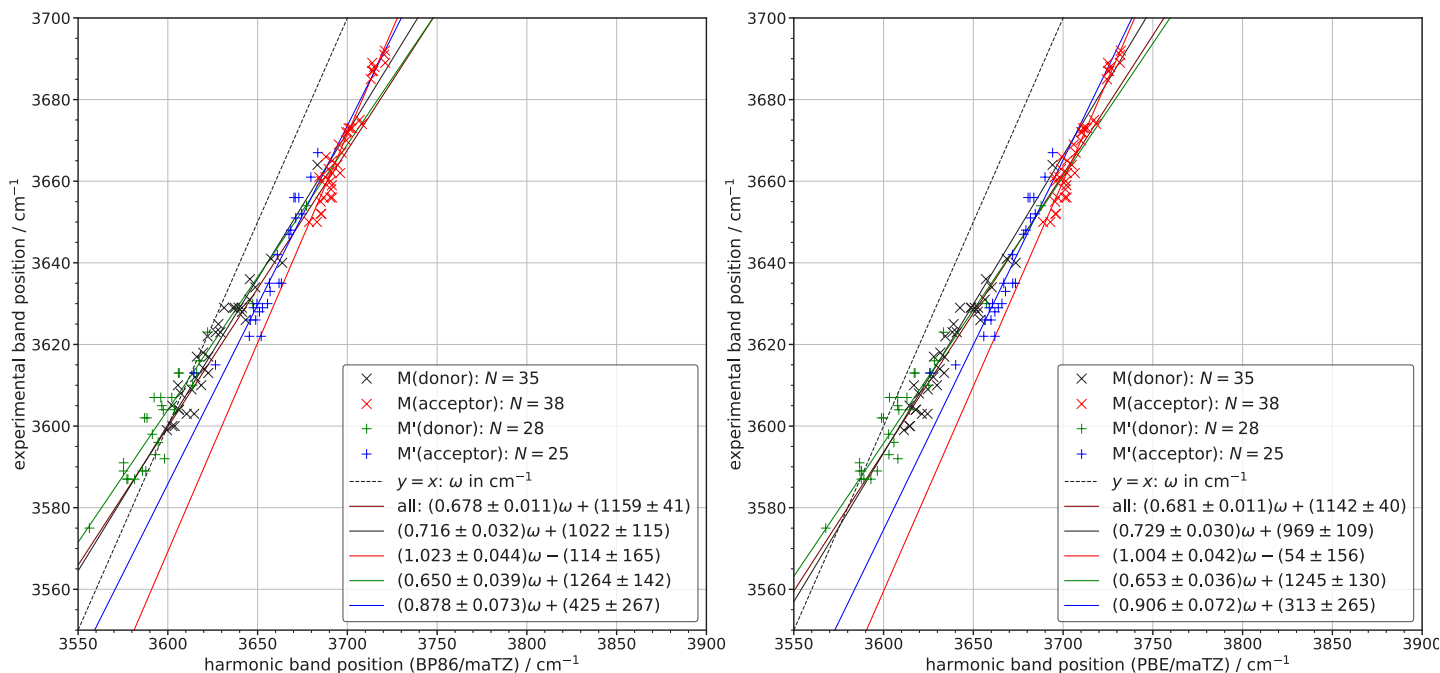


Fig. S10: Correlation plots of the primed hydrogen bond donors (green) and acceptors (blue) as well as the unprimed hydrogen bond donors (black) and acceptors (red) of conformers comparing BP86 (left) and PBE (right). The plot shows the individual contributions to Fig. 30 (PBE only, arbitrarily) of the main text. N indicates the number of bands for each sub class. BP86 and PBE behave similarly, hence BP86 is not included in the main text for simplicity. Fits with errors (σ) for each sub class are shown in their corresponding colour as well as an all fit in brown ($N = 126$). As can be seen from the fit parameters, BP86 and PBE behave quite similarly. As was the case for PBE0, h is higher for the acceptor bonds than for the donor bonds. Additionally, h is in general closer to 1 than the previous all fits (BP86: 0.658; PBE: 0.664, see Fig. S3) as well as an all fit for the 4 sub classes. It should be kept in mind that the all fit of the main text only involves bands of the training set ($N = 35$). In case of M(acceptor) the physical (but hardly significant) sign for a_2 is found. The error bars indicate that a division into sub classes is favourable for both GGAs in comparison to B3LYP (see Fig. S9).

3.3 Error Evaluation

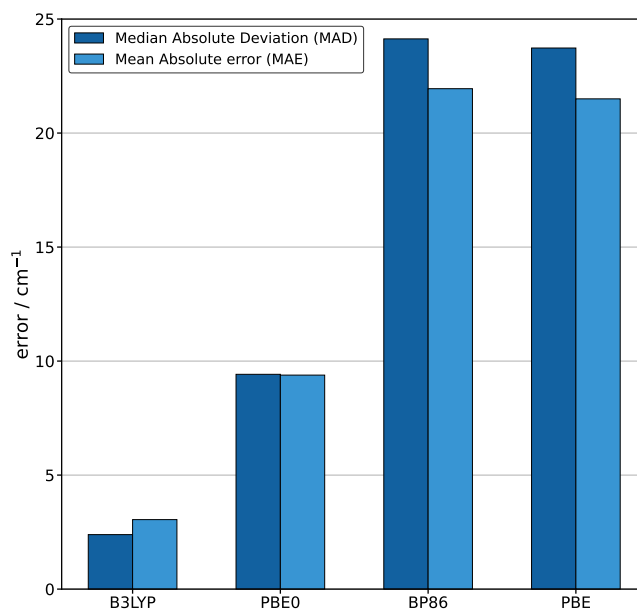


Fig. S11: Unnormalised Median Absolute Deviation (MAD) and Mean Absolute Error (MAE) of the intramolecular hydrogen bond shifts (OH wavenumber differences) for the four tested functionals. Normalised errors can be found in Fig. S12.

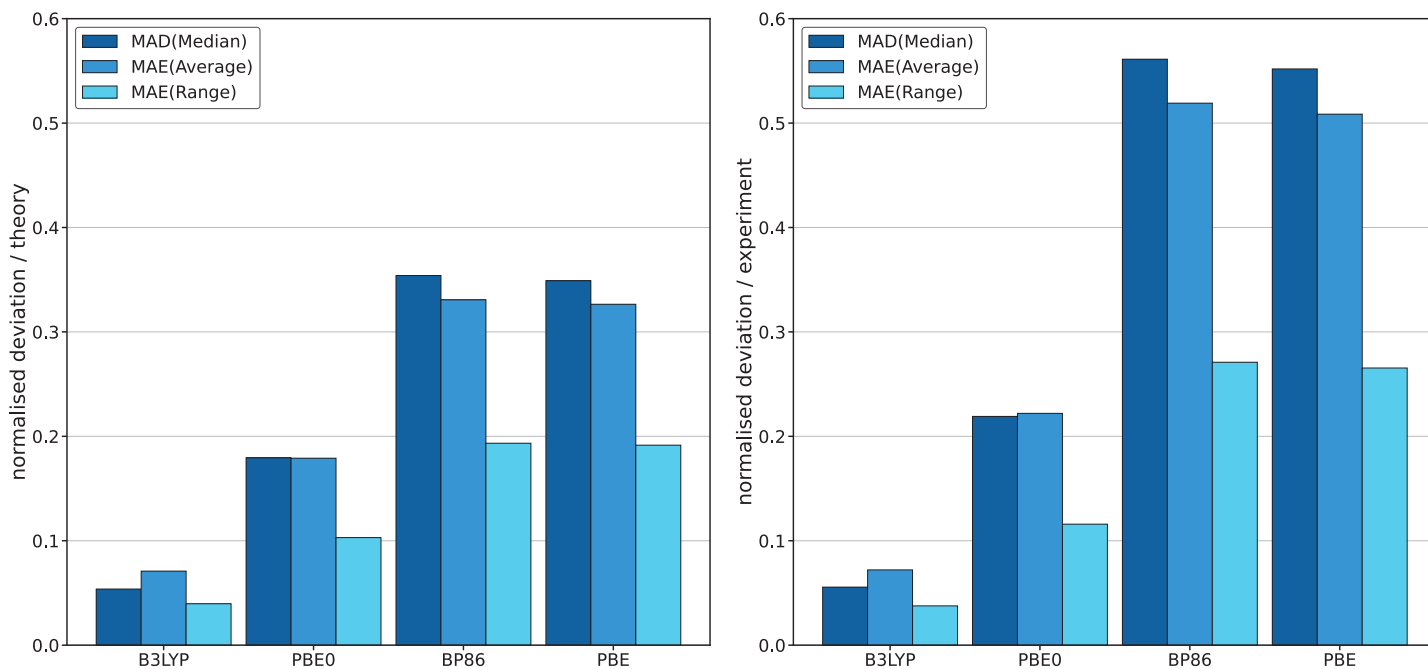


Fig. S12: Normalised deviations of the experimental intramolecular hydrogen bond shifts (OH wavenumber differences) from the predicted ones are shown based on the respective theoretical method (left) used as reference and the experimental data (right) used as reference. The Median Absolute Deviation (MAD) and Mean Absolute Error (MAE) are shown. In parentheses the normalisation method is shown where range indicates the difference between the maximum and minimum of the data. The fact that the error increases substantially when the experimental data is used for normalisation in case of the GGAs again highlights their lacklustre predictive capabilities. The MAE is computed with PYTHON 3 as `numpy.average(numpy.abs(Exp-Theo))` and MAD as `numpy.median(numpy.abs(Exp-Theo))` and subsequently normalised by dividing with `numpy.average(Exp)` (Average), `numpy.median(Exp)` or `np.max((Exp))-np.min((Exp))` (Range) in case of the plot on the right while theoretical data is used for normalisation on the left. Unnormalised errors can be found in Fig S11.

4 Assignments

4.1 Detailed Explanation

Here we provide detailed explanations how the assignments were achieved in section 4 of the main text. Supporting energy matrices as well as experimental and simulated spectra at the B3LYP/maTZ level of computation are shown.

4.1.1 Methyl substitutions and model testing

As can be seen from Fig. S13 (left), 0-M and 0-Ma are almost iso-energetic so that 0-Ma would only partially convert to 0-M under jet conditions despite a low barrier. Similarly, 0-M' converts to 0-M. Unlike 0-Ma there are no other conformers converting to 0-M' which is also the case for 0-Ma'. Analogous to 0-M, 0-Mb is the lowest member of another family of easily interconverting isomers, including 0-Mc and 0-Mb'. There are also no conformers that easily convert to 0-Mb'. As with all primed/unprimed pairs investigated in section 4.1.1, 0-Mc' converts to 0-Mc.

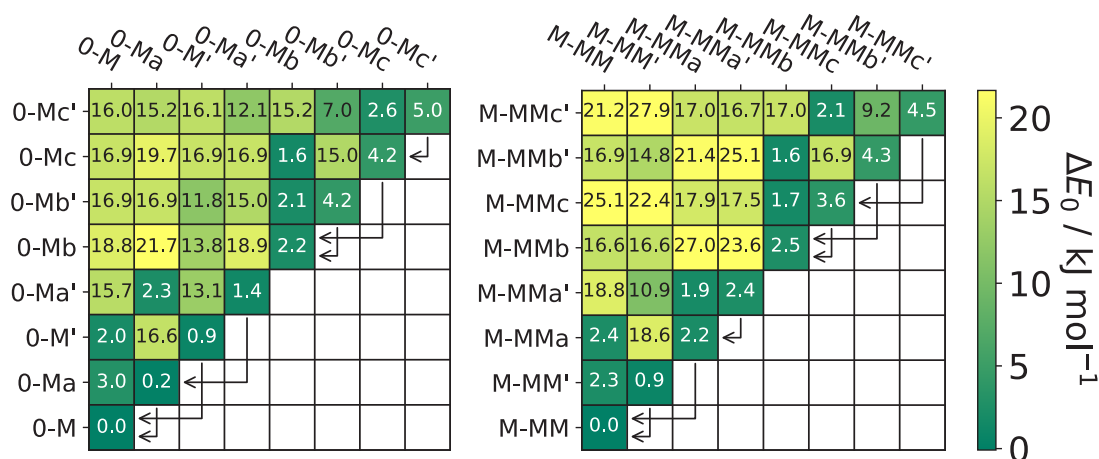


Fig. S13: Overview of the relative zero point corrected energies (diagonal) of the different conformers and barriers for the corresponding interconversion (off-diagonal) at the B3LYP/maTZ level of computation for propanediol (0-M) and methyl-butanediol (M-MM). Barriers are given relative to the meta-stable conformer.

0-M has been previously investigated by jet FTIR spectroscopy^[7], where five conformations could be assigned despite spectral overlap of the rotational contours surviving the jet cooling. The sum of 0-Ma and 0-Mb was shown to have a combined abundance comparable to that of the global minimum 0-M structure, whereas 0-M' and 0-Ma' had a lower abundance. To further investigate the complex relaxation behaviour of 0-M we recorded additional Raman spectra with argon mixed in helium as can be seen in Fig. S15. 0-M can be easily identified in the spectrum since it does not change with varying argon content. Similarly, it is to be expected that 0-Mb should remain fairly constant, which can be seen for the non-overlapping band in the spectrum. In case of 0-M', 0-Ma', 0-Mb' and 0-Mc' no conformers can easily relax towards them and therefore they should decrease quickly in intensity because no conformers can replenish their population. On the other hand, 0-Ma and 0-Mc should decrease more slowly in intensity although 0-Mc only profits from the small population of 0-Mc'. A sharp decrease can be observed for 0-M' although for the free OH mode an overlap with water makes a direct interpretation difficult. The free OH mode of 0-Mb' also overlaps with 0-M' but is expected to behave similarly. The bound OH mode of 0-M' also overlaps with those of 0-Ma' and 0-Mc', which both behave in a similar way as 0-M'. 0-Ma decreases rather slowly in comparison as expected although an overlap with 0-Ma' and 0-Mb for the bound OH mode may skew the picture. Considering that 0-Mb should remain constant and 0-Ma' decreases quickly the general interpretation should still hold.

rac-Butane-2,3-diol (rM-M) is more symmetric than 0-M and its conformational landscape is less complicated as can be seen from Fig. S14. Yet again, the unprimed/primed pairs readily relax towards the energetically

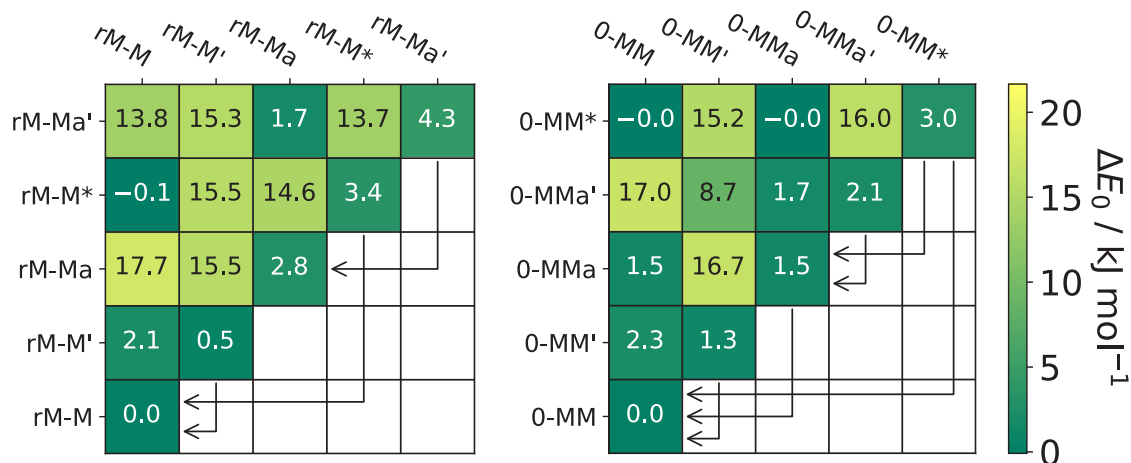


Fig. S14: Overview of the relative zero point corrected energies (diagonal) of the different conformers and barriers for the corresponding interconversion (off-diagonal) at the B3LYP/maTZ level of computation for butanediol (rM-M) and methyl-propanediol (0-MM). Barriers are given relative to the meta-stable conformer.

favourable unprimed variants. rM-M* also effectively relaxes towards rM-M without a barrier. In the cases of rM-M', rM-M* and rM-Ma' no mechanisms exist to replenish their populations.

Fig. S15 includes the B3LYP based results for rM-M. The predictions for rM-M as well as rM-Ma' fit very well to the experimental spectrum. As for t6-6 relative to 0-0, a downshift of rM-M relative to 0-M can be observed. Given that the simulated intensities of rM-Ma' fit quite well for the free and bound OH mode it seems likely that rM-M*, which would otherwise coincide with the free OH mode, mostly relaxes. Since rM-M* is only stable at the B3LYP level, it will not be assigned. Furthermore, the bound OH vibrations of rM-M' and rM-Ma are not well predicted in terms of their band positions. However the general intensity pattern is well reproduced. As predicted by the barriers some relaxation is taking place with rM-M' whereas hardly any can be observed by rM-Ma relative to the simulated spectrum. In comparison to the bound OH modes of rM-M' and rM-Ma the free ones fit rather well. The shoulder towards lower wavenumbers of the free OH vibration of rM-M is likely caused by rM-Ma.

2-Methyl-propane-1,2-diol (0-MM) has the same overall degree of substitution ($n_D = 2$) as rM-M (or t6-6). The conformational landscape of 0-MM is somewhat similar to rM-M with some key differences (see Fig. S14). The unprimed/primed pairs behave the same whereas 0-MMa now also has an efficient pathway to relax to 0-MM. Furthermore, not only 0-MM* but also 0-MMa can readily interconvert to 0-MM. Due to this 0-MMa is expected to somewhat relax but both 0-MMa' and 0-MM* may replenish its population. An energetic comparison with other tested functionals can be found in Tab S8. Again, the stability of primed conformers is overestimated by the GGAs. 0-MM* also converges to 0-MM for all functionals besides B3LYP.

The experimental spectrum of 0-MM as well as a simulation based on the B3LYP correlation for t6-6 is shown in Fig. S15. The predictions seem to fit reasonably well, indicating that the overall degree of substitution is more important than the substitution pattern. However, other than for rM-M, a general downshift cannot be observed relative to 0-M. As was the case for rM-M, the lowest conformation 0-MM is predicted best whereas the shift between the OH modes for 0-MM' is again overestimated and underestimated for 0-MMa. As expected from the barrier calculations, strong relaxation can be observed for 0-MM' while only some can be observed for 0-MMa relative to the predicted intensities. Given the two very efficient pathways for 0-MM*, it rather completely relaxes towards more stable conformers. 0-MMa' also considerably interconverts but a band of similar size as for rM-M can be found that fits the free OH mode. An overlap of the bound OH mode with the bound OH mode of 0-MM' can explain the broadening in the experimental spectrum.

The secondary-tertiary substitution pattern ($n_D = 3$) is realised by methyl-butanediol (M-MM). In terms of its symmetry it is analogous to 0-M which results in a very similar conformational landscape as can be seen looking at Fig. S13 (right). The B3LYP energetic ordering varies slightly but the barriers are very similar. Therefore we expect a similar relaxation behaviour. The other tested functionals also behave similarly as they did for 0-M as can be seen from Tab. S15.

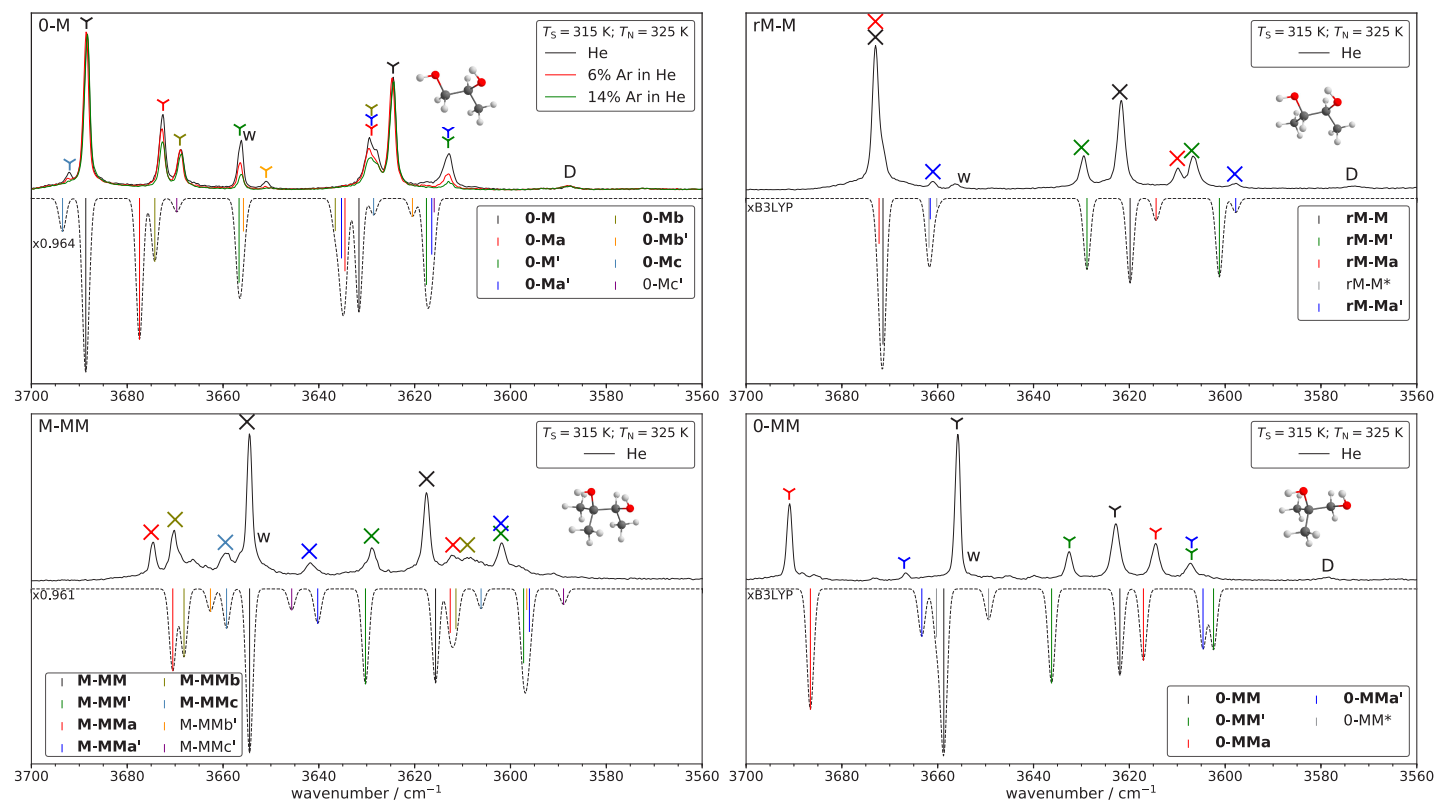


Fig. S15: Experimental spectra (plotted upwards) and simulated spectra (plotted downwards) of propanediol (0-M), butanediol (rM-M), methyl-propanediol (0-MM) and methyl-butanol (M-MM). To investigate the relaxation behaviour, different admixtures of argon to helium were used in case of 0-M. Saturator (T_S) and nozzle temperatures (T_N) are provided. The simulation is based on B3LYP calculations and Boltzmann weighted according to T_N and the relative energies given in Figs. S13 and S14. Wavenumber scaling factors for the free OH mode for the most stable conformer are also given. xB3LYP indicates that the B3LYP fit ($n_D = 2$) was used to simulate the spectrum (see Tab. S38).

When comparing the experimental spectrum of M-MM to the other methyl substitutions in Fig. S15 a general downshift relative to 0-M can again be observed. It also appears that the spectrum is similar to that of 0-MM. The 0-MM and M-MM OH modes are at very similar positions and M-MMa is shifted above the free OH mode of M-MM albeit not as strongly as for 0-MMa. Furthermore, the rather broad bands where the bound OH modes of M-MMa, M-MMb and M-MMc are predicted make a proper assignment difficult. Since B3LYP appears to underestimate the separation of M-MMa and M-MMb, as was already the case for 0-Ma and 0-Mb, it is assumed that the two broad maxima correspond to these conformers with some additional unresolved broadening by M-MMc. Analogous to 0-Mb' and 0-Mc' these conformations likely do not play a role in the spectrum.

4.1.2 Other hydrogen contacts (to π -clouds and F)

An energetic overview for 3-butene-1,2-diol (0-V) is shown in Fig. S16a indicating a rather high conformational complexity. Unlike the previously discussed methyl substituted systems only one conformer (0-Vd) has an efficient relaxation pathway to the most stable 0-V conformer although some conversion of 0-Va' and 0-Vc' to the ground state may take place. On the other hand, 0-Vc and 0-Va' are expected to convert easily to 0-Va. The only remaining efficient pathway is expected to be from 0-Vb' to 0-Vc. For 0-Vb, 0-V', 0-Va' and 0-Vb' no or little conversion to the two lowest energy conformations is to be expected. A comparison of all tested functionals can be found in Tab S6. In case of the GGAs as well as PBE0 zero point correction changes the energetic order quite substantially. Additionally they also predict 0-V and 0-V' to be very close in energy which is not reflected in the experimental spectrum.

The predictions based on the B3LYP correlation derived for $n_D = 1$, as well as the experimental spectrum for 0-V are shown in Fig. S17. The bands for the two most stable conformers can be easily identified although some overlap with other conformers is to be expected. The overlap of the free OH mode of 0-Va and 0-Vb does

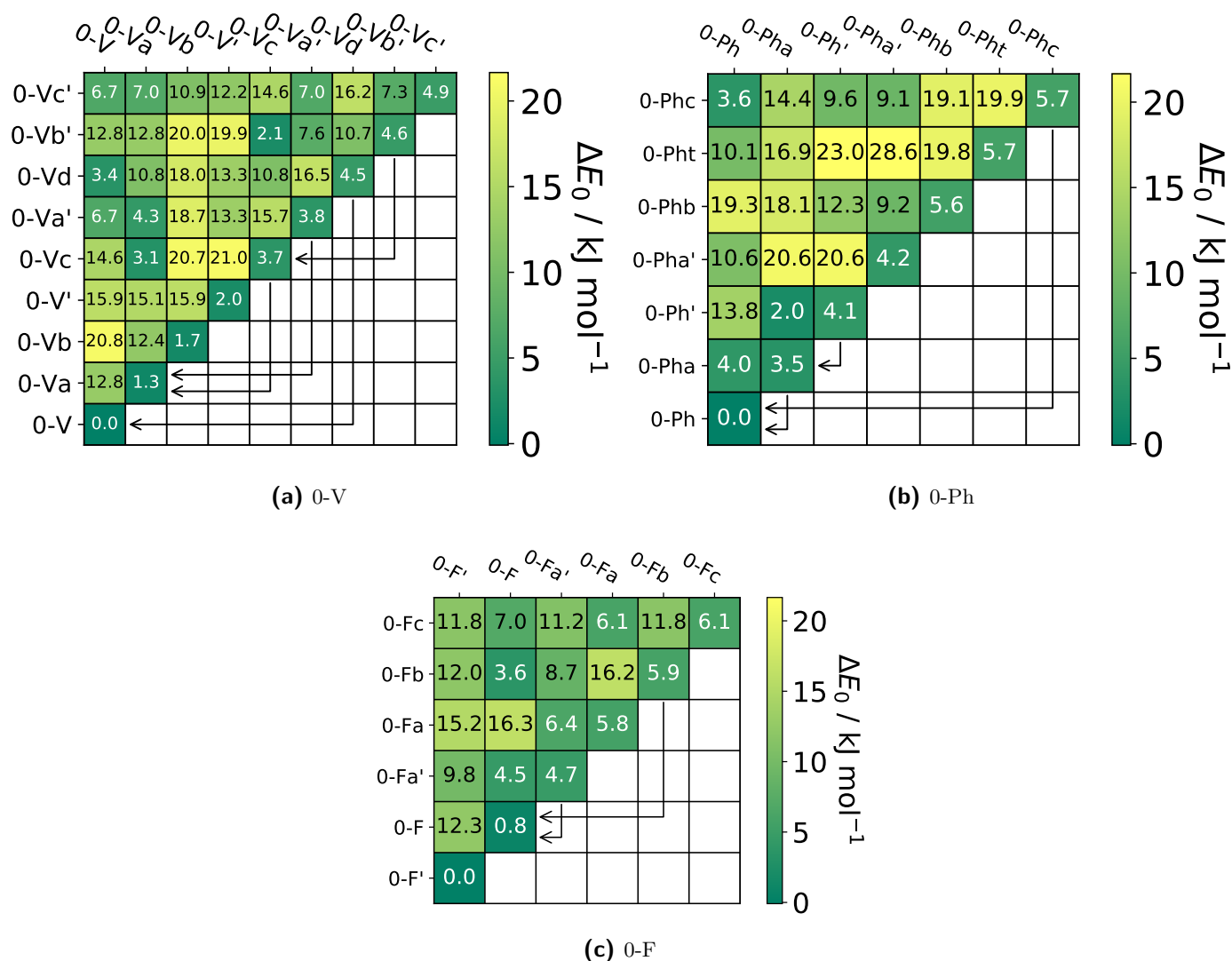


Fig. S16: Overview of the relative zero point corrected energies (diagonal) of the different conformers and barriers for the corresponding interconversion (off-diagonal) at the B3LYP/maTZ level of computation for 3-butene-1,2-diol (0-V), 1-phenyl-ethane-1,2-diol (0-Ph) and 3,3,3-trifluoro-propane-1,2-diol (0-F). Barriers are given relative to the meta-stable conformer.

not quite correspond to the experimental intensity which may be caused by the rather broad nature of the band including a pronounced low wavenumber shoulder. This may also explain the low experimental intensity of the bound OH-mode of 0-V. This band also overlaps with 0-Vb and 0-Vc' which are not expected to relax much whereas 0-Vc is expected to relax to 0-Va. Around the predicted free OH-mode of 0-V' many other bands also cluster. 0-Vb' and 0-Vc' can likely be disregarded in this discussion. 0-Va' and 0-Vd can easily relax and match the small band around 3610 cm^{-1} . The band around 3613 cm^{-1} can therefore be assigned to free OH mode of 0-V' which is not expected to relax at all. The remaining lowest lying band can be assigned to the bound OH mode. The rather large discrepancy between the predicted and the experimental band position in this case is probably due to a direct contact towards the vinyl group whereas for other conformers it is not directly involved in the hydrogen bonding. Since 0-Vd appears to strongly relax, judging from its bound OH-mode, this should also be the case for its free mode. This is also to be expected of 0-Vc which overlaps with the previously mentioned band. Therefore, the signal near 3687 cm^{-1} is also accounted for.

Phenyl-ethanediol (0-Ph) exhibits less conformational complexity than 0-V as can be seen from Fig. S16b. It is also the first system where a conformer with an anti-periplanar orientation may become relevant. 0-Pha and 0-Phc can both relax towards the most stable 0-Ph conformer. Besides a possible relaxation of 0-Ph' to 0-Pha no other efficient pathways for interconversion are predicted. 0-Ph' can therefore likely be discarded for the interpretation of the spectra. A comparison of all tested functionals as well as the results by Lomas^[6] can be found in Tab.

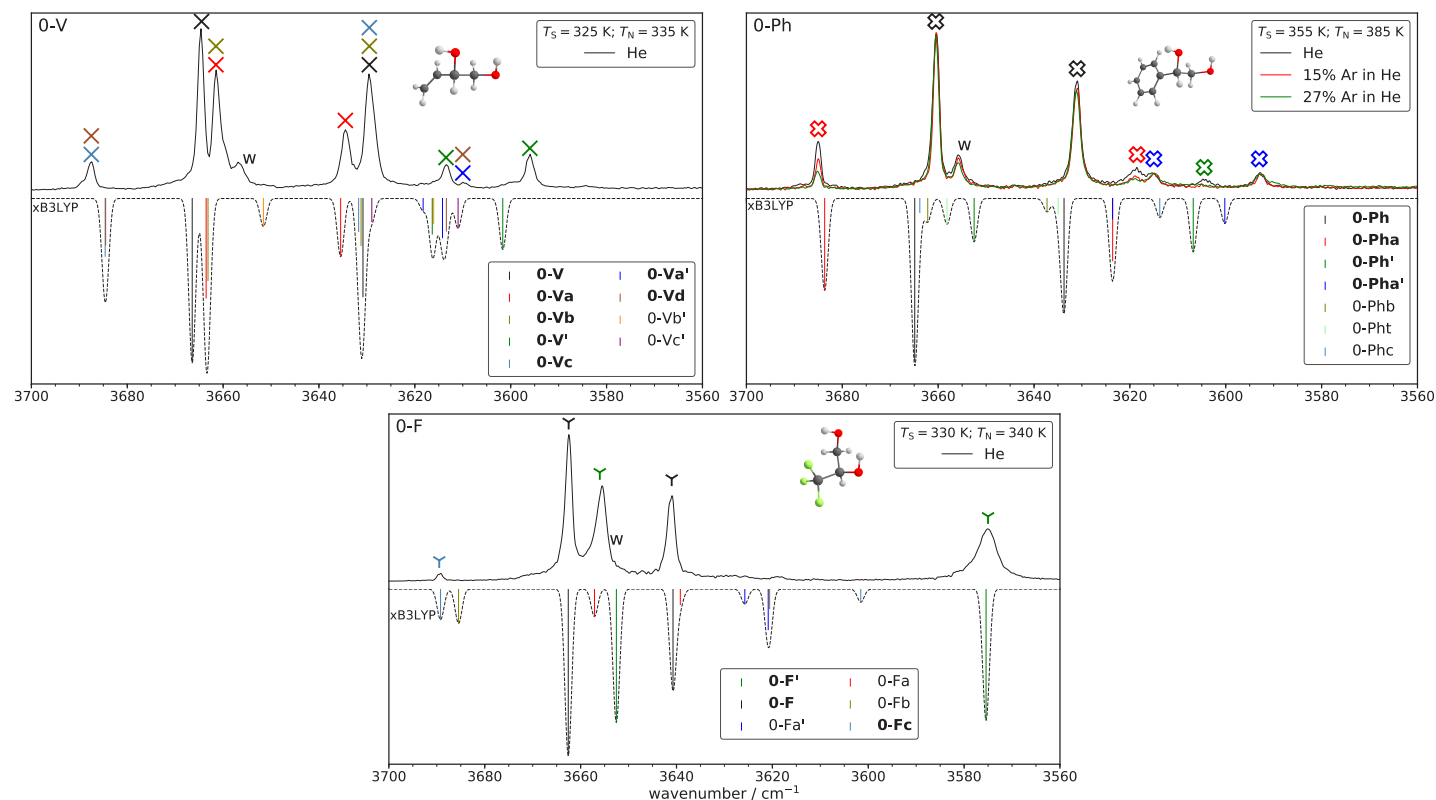


Fig. S17: Experimental spectra (plotted upwards) and simulated spectra (plotted downwards) of butenediol (0-V), phenylethanol (0-Ph) and trifluoro-propanediol (0-F). To investigate the relaxation behaviour, different admixtures of argon to helium were used in case of 0-Ph. Saturator (T_S) and nozzle temperatures (T_N) are provided. The simulation is based on B3LYP calculations and Boltzmann weighted according to T_N and the relative energies given in Fig. S16. xB3LYP indicates that the B3LYP fit ($n_D = 1$) was used to simulate the spectrum (see Tab. S38).

S7. Noticeably B3LYP reverses the order of 0-Ph' and 0-Pha' in comparison to the other tested functionals. However, given the high relaxation propensity of 0-Ph', the experiment does not allow for a direct comparison. Furthermore the results by Lomas^[6] agree with the energetic order predicted by B3LYP with the exception of 0-Phc only being predicted to be stable in benzene.

The Raman spectrum of the 0-Ph conformation is again predicted very well, whereas the assignment of the bound OH mode of 0-Pha is not as clear (see Fig. S17). However, the barriers indicate that 0-Pha should relax fairly easily, in line with the experimental free OH mode intensity evolution. Therefore, the broad band at around 3618 cm^{-1} , which matches the relaxation behaviour, can be assigned to the bound OH mode of 0-Pha. 0-Phb and 0-Pht either overlap with other more intense bands/water or are just not present in sufficient amounts. 0-Phc can also easily relax and considering its high energy should not be observed. The broad band at 3605 cm^{-1} can be assigned to 0-Ph' which is predicted to easily relax, matching experiment. The free OH mode of 0-Ph' may be present as a small shoulder of the water band which also quickly vanishes when Ar is added. The two remaining bands at 3615 cm^{-1} and 3593 cm^{-1} can be assigned to 0-Pha' which is not expected to relax at all, in harmony with experiment. The predicted intensities also fit quite well. The rather large deviation of the absolute band positions are again caused by a direct involvement of the π -system in the hydrogen bond arrangement as was the case for 0-V'. Both 0-V' and 0-Pha' share the same structural motif (see Fig. S25 and S26).

The conformational landscape of trifluoro-propanediol (0-F) differs considerably from that of propanediol (cf. Fig. S16c vs. Fig. S13). In contrast to all other studied systems a primed variant (0-F') is now the most stable conformer which also directly involves a hydrogen bond (or rather contact) towards a fluorine atom. 0-F follows only slightly higher in energy. All other conformers are significantly higher in energy, somewhat reminiscent of 0-Ph (cf. Fig. S16b). No efficient relaxation pathway to the most stable conformer 0-F' exists whereas both 0-Fa' and 0-Fb are expected to easily (and 0-Fc partially) convert to 0-F. Some inefficient relaxation may also take place from 0-Fa to 0-Fa' and from 0-Fc to 0-Fa. Unlike most other systems the GGAs yield the same energetic order as the hybrid functionals do, as documented in Tab. S5.

Looking at the predicted spectra in Fig. S16c perhaps somewhat surprisingly both 0-F' and 0-F fit well to the dominant experimental bands. Despite the hydrogen contact to fluorine in 0-F', the deviations appear to be less pronounced than for π contacts in 0-V' and 0-Pha'. All other conformers besides 0-F' have favourably aligned O-H and C-F dipoles rather than actual hydrogen bonds/contacts. Furthermore the spectrum indicates that 0-Fa' extensively relaxes to 0-F. 0-Fa may convert to 0-Fa' but since the latter cannot be observed at all this seems not to be the case. Furthermore, 0-Fa would also overlap with 0-F' and 0-F. 0-Fb readily relaxes to 0-F and given that the bound OH mode cannot be observed the free OH mode should not be observed either. Therefore, the band around 3689 cm^{-1} can be assigned to 0-Fc which is not expected to easily relax. The fact that the bound OH mode of 0-Fc cannot be observed can be rationalised by the fact that the predicted intensity of the free OH mode is considerably higher.

4.1.3 Cyclic systems

As mentioned in the main text the rather stretched shortest hydrogen bond or hydrogen contact of t4-4 leads to energetically relevant conformers without something resembling a hydrogen bond. A divide between axial and equatorial is also no longer possible. Furthermore, the barriers associated with these conformations can also be overcome more easily under jet conditions as can be seen in Fig. S18a. Significant relaxation is to be expected although the excessive width of pathways between t and non t conformations may reduce the relaxation propensity, such that the lowest conformations with and without t labels are expected to be significantly populated. Additionally, the pathway of t4-4t to t4-4* led to the same optimised transition state, based on the converged climbing image, as was found for t4-4* to t4-4. In case of the transition of t4-4t to t4-4* this would lead to a negative electronic energy barrier which excludes this transition state from actually belonging to this pathway. Only the pathways from t4-4* to t4-4' and t4-4at to t4-4t are associated with significant barriers where relaxation may be restricted. The GGAs again predict the t4-4' conformer to be more stable in conflict with the experimental spectrum (see Tab. S9). Additionally t4-4at is predicted to be very close in energy to t4-4* for BP86, PBE and PBE0, unlike B3LYP.

As can be seen from Fig. S19 the derived B3LYP $n_D = 2$ correlation shows some significant deviations from the experimental spectrum in case of t4-4. This deviation can be attributed to the uniquely high ring strain of this system in comparison to the others. However, the two most intense experimental bands can be matched with the most stable t4-4 conformer. Considering that t4-4bt is expected to relax significantly towards other conformers the simulated intensities match quite well for t4-4. The two bands at 3669 cm^{-1} and 3674 cm^{-1} can then be assigned to the t4-4* and t4-4t conformers respectively. Comparing the experimental intensities to the predictions also indicates that both t4-4t and t4-4* significantly relax as the calculated barriers would suggest. The band at 3654 cm^{-1} can be assigned to the free OH mode of t4-4' with some significant overlap of a water band. The water band can be clearly distinguished by monitoring the bands over many exposures. However, the bound OH mode of t4-4' and the band at lower wavenumbers of t4-4at cannot straightforwardly be assigned. The band at 3645 cm^{-1} could possibly be assigned to the bound OH mode of t4-4' which would indicate that B3LYP underestimates the separation between the two t4-4' bands. Over multiple exposures the signal 3645 cm^{-1} behaves like all others (besides water) making it unlikely that it is caused by an impurity. t4-4at may overlap with the free OH mode of t4-4' or it could explain the rather high baseline in between the signals at 3645 cm^{-1} and 3654 cm^{-1} .

In case of t5-5 a distinction between di-axial and di-equatorial is possible again. However, opposite to t6-6 a conversion to or from di-axial conformations is energetically feasible under jet conditions as can be seen from Fig. S18b. Di-axial conformers are designated with a t in Fig. S18b. Barriers overall are quite low and some degree of relaxation is expected for all species. Unlike t4-4 in case of t5-5 all tested functionals predict the t5-5 conformer to be the most stable one (see Tab. S10). However the GGAs predict t5-5 and t5-5' very close in energy which is not reflected in the experimental spectrum.

The B3LYP correlation fits reasonably well but many signals exist in very close proximity which makes a clear assignment difficult as can be seen from Fig. S19. The most stable conformer can be easily identified as the two most intense bands at 3672 cm^{-1} and 3639 cm^{-1} . Considering that t5-5' is expected to relax very efficiently the band at 3630 cm^{-1} can be assigned to the more intense OH mode, while the other is not visible. The four bands around 3652 cm^{-1} may be assigned according to their relative order. The signals at 3654 cm^{-1} and 3650 cm^{-1} can

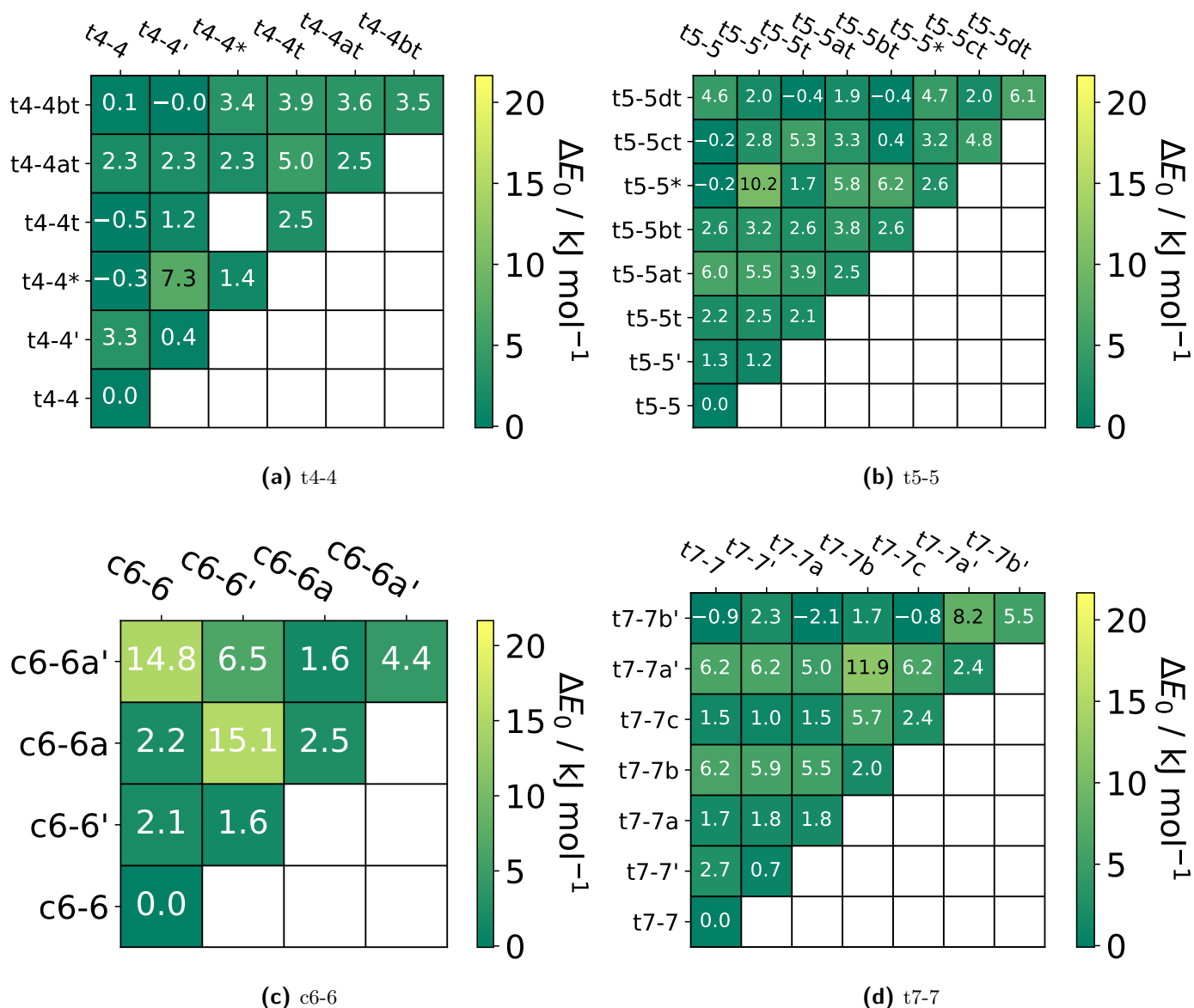


Fig. S18: Overview of the relative zero point corrected energies (diagonal) of the different conformers and barriers for the corresponding interconversion (off-diagonal) at the B3LYP/maTZ level of computation for *trans*-cyclobutanediol (t4-4). Barriers are given relative to the meta-stable conformer.

be assigned to t5-5ct. The most intense band can be assigned to t5-5t and the band at 3647 cm^{-1} to t5-5ta where both OH modes overlap. However, the experimental intensities do not match the predictions especially since t5-5t and t5-5ct are expected to relax significantly whereas t5-5ta is not. The signal at 3662 cm^{-1} can be assigned to t5-5t which matches the relative intensity of the previously assigned band. Much less clear is the identification of the bands at 3665 cm^{-1} and 3669 cm^{-1} . In both cases an overlap of t5-5* and t5-5bt could fit. Furthermore VPT2^[19] calculations done with Gaussian 16 (Revision A.03)^[20] also reveal that a few ring breathing vibrations may serve as hot band bases for the free OH mode of t5-5, while the same vibrations would lead to non resolved hot bands for the bound OH mode. The corresponding harmonic and anharmonic wavenumbers as well as the coupling constants can be found in Tab. S21. Additionally, for t5-5bt significant relaxation is to be expected which also does not fit to the experimental intensities. Overall there are some serious problems in assigning the bands when di-axial conformations are involved which also extends to the intensity and hence also the calculated barriers. Therefore, we restrict ourselves to the safe assignments of t5-5 and t5-5'.

Conformationally, c6-6 is comparatively simple compared to most other studied diols as can be seen from Fig. S18c. The conformers c6-6' and c6-6a can easily relax to the most stable c6-6 species, as can c6-6a' via c6-6a. A comparison of our energetic results with those of Lomas^[6] can be found in Tab. S12. Lomas' results are in line

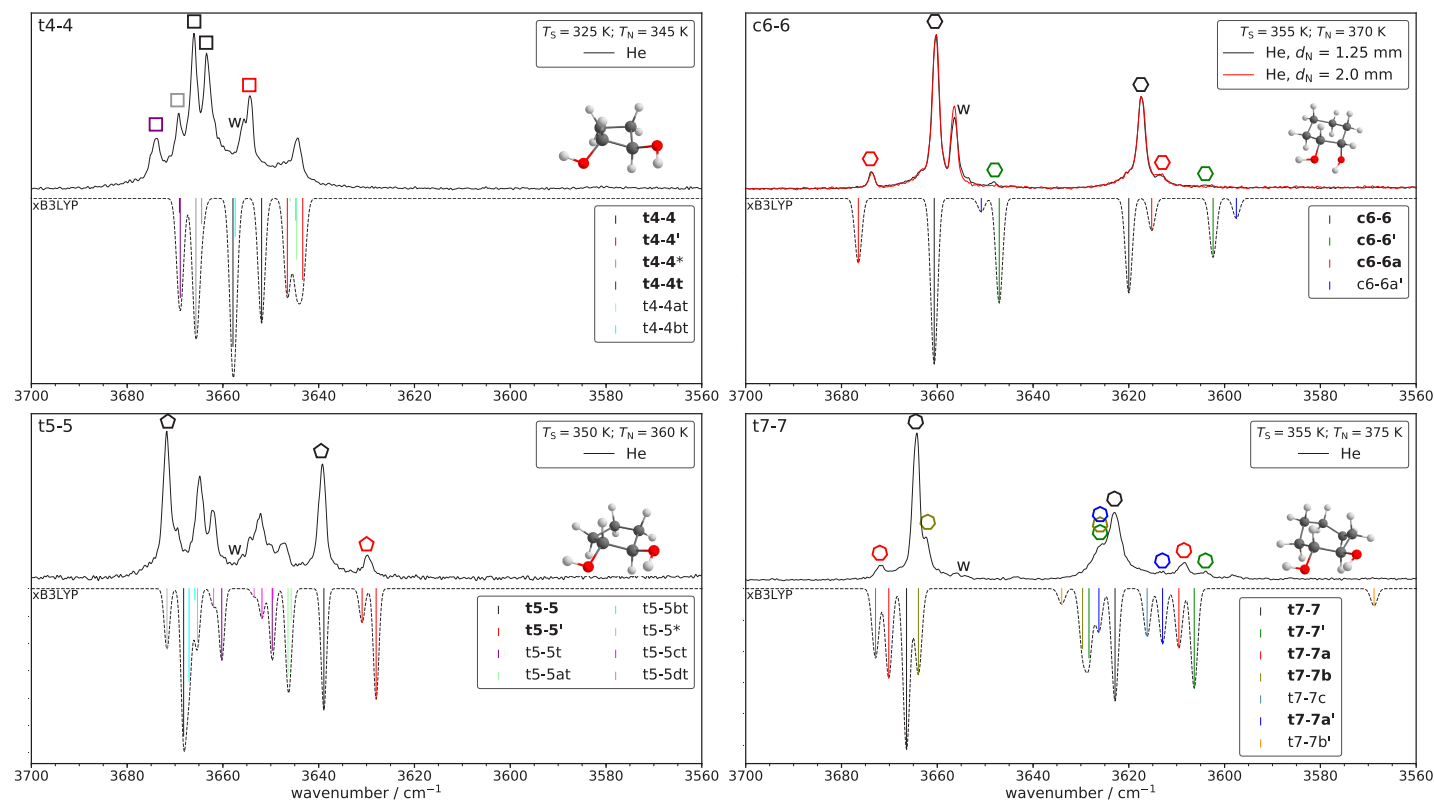


Fig. S19: Experimental spectra (plotted upwards) and simulated spectra (plotted downwards) of *trans*-cyclobutanediol (t4-4), *trans*-cyclopentanediol (t5-5), *cis*-cyclohexanediol (c6-6) and *trans*-cycloheptanediol (t7-7). To investigate the relaxation behaviour, different nozzle distances were used in case of c6-6. Saturator (T_S) and nozzle temperatures (T_N) are provided. The simulation is based on B3LYP calculations and Boltzmann weighted according to T_N and the relative energies given in Fig. S18. xB3LYP indicates that the B3LYP fit ($n_D = 2$) was used to simulate the spectrum (see Tab. S38).

with our hybrid functional calculations. The GGAs predict c6-6a and c6-6a' very close in energy which is not reflected in the experimental spectra.

The most stable conformer c6-6 can be easily identified in the experimental spectrum (see Fig. S19). c6-6' is barely visible at a nozzle distance of $d_N = 1.25 \text{ mm}$ and vanishes at a distance of $d_N = 2.0 \text{ mm}$ which is in line with the low computed barrier. c6-6a on the other hand appears to be frozen in its population which is not in line with a barrier of 2.2 kJ mol^{-1} . This may be explained in terms of the width of the barriers. In case of c6-6/c6-6' the hydrogen bond acceptor changes orientation, whereas in case of c6-6/c6-6a the hydrogen bond donor and acceptor change position (axial donor for c6-6, equatorial donor for c6-6a) which results in a widened barrier. This would lead to less tunneling assisted barrier crossing and could result in a freezing of the c6-6a population. B3LYP/maTZ may also be inadequate to describe such a relaxation pathway. c6-6a' expectedly fully relaxes early on in the expansion and is not visible. Overall, the derived B3LYP correlation agrees well with the experimental results, indicating that axial-equatorial hydrogen bonds do not hamper the predictive capabilities in this case.

Similarly to t6-6 di-axial conformations are not energetically feasible in case of t7-7, as can be seen from Fig. S18d. t7-7' and t7-7a can both easily relax to the most stable t7-7 conformer and strong relaxation is expected in the experimental spectrum. This is also expected for t7-7c and t7-7b' although for both species one relaxation pathway is inefficient. For t7-7b and t7-7a' on the other hand little to no conversion to other conformers is to be expected. As was the case for t4-4, t7-7' is predicted to be the global minimum for the GGAs as can be seen from Tab. S13.

The derived correlation for B3LYP fits reasonably well to the experimental spectrum as Fig. S19 shows. The most stable conformer can once again be easily spotted, although the bound OH mode is significantly broader than the free OH mode. Since t7-7c has many channels to easily relax it will not be present in significant amounts and the band around 3672 cm^{-1} can therefore be assigned to t7-7a. Consistent with the transition state calculations and the observed intensity in relation to the predicted population at the nozzle, t7-7a relaxes significantly. t7-7b

should remain largely unchanged in terms of intensity which is also reflected in the experimental spectrum. In either case it is visible as a shoulder of $t7-7$ (3662 cm^{-1} and 3626 cm^{-1}). The band around 3608 cm^{-1} could potentially belong to the bound OH mode of $t7-7a$ or $t7-7'$. If this band belonged to $t7-7'$ the signal at 3626 cm^{-1} would be expected to be larger therefore it likely belongs to $t7-7a$. The band intensity is also in line with the free OH mode of $t7-7a$. Hence, the smaller band at 3604 cm^{-1} can be assigned to $t7-7'$. Lastly the band at 3613 cm^{-1} can be tentatively assigned to $t7-7a'$ where little relaxation is expected. However, in view of this the predicted intensity is overestimated.

4.1.4 Fully substituted systems

The energetics of CP-MM are shown in Fig. S20a. CP-MM is another example where t conformers are energetically relevant (CP-MMt is shown in Fig. S36). The conformational landscape is significantly more complex than in all other studied systems. Furthermore, the t and non- t conformers constitute different families that cannot interconvert easily. Within the t family strong relaxation towards the most stable CP-MMt conformer is expected. Non- t species are expected to accumulate in CP-MM. CP-MMb' stands out due to the fact that only a single energetically feasible pathway exists out of the 5 possible ones. An overestimation of the stability of primed conformers can again be found for the GGAs (see Tab. S17). However for the hybrid functionals CP-MM is only the most stable conformer after zero point correction. Additionally there is a strong mismatch for t type conformers where CP-MMbt and CP-MMct are more stable than CP-MMt and CP-MMat in case of the GGAs.

The free OH band of the most stable CP-MM conformer can easily be identified when looking at Fig. S21 but also overlaps with CP-MMa and CP-MMb'. The band at 3635 cm^{-1} can be assigned to an overlap of CP-MM' and CP-MMa'. However, the predicted intensities are not fully in line with the expected relaxation propensity. Especially in case of CP-MMa' which is not replenished by any other conformer but can easily relax towards CP-MM', less intensity than for CP-MM' would be expected, which also profits from CP-MMa. We co-assign CP-MMa und CP-MMa' to the relatively broad peaks despite the absence of unique evidence for them, because of their likely thermal population based on the predicted low energy. The band at 3662 cm^{-1} is likely caused by CP-MMb since the CP-MMc population cannot be replenished by any other conformer. The very broad band at 3600 cm^{-1} is caused by an overlap of CP-MM, CP-MMa and CP-MMb. A clear band centre cannot be identified, however the band tails off towards higher wavenumbers which is in line with the expected higher intensity for CP-MM. In such a case, the wavenumber assigned to the overlapping conformations is normally the same, but

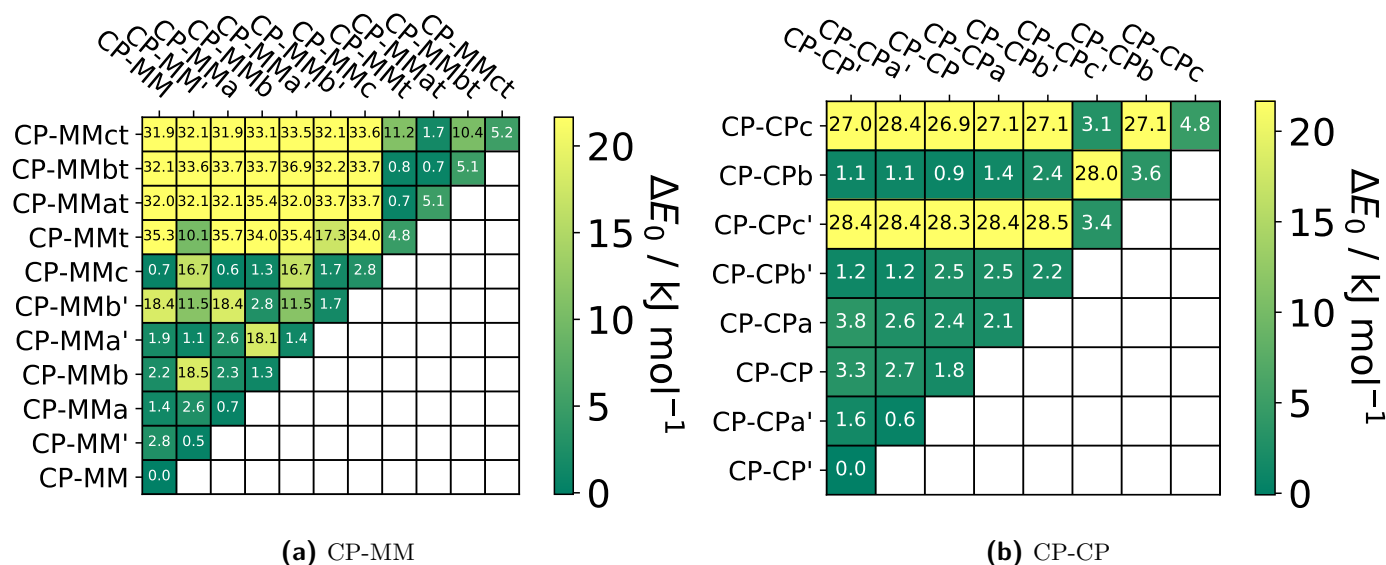


Fig. S20: Overview of the relative zero point corrected energies (diagonal) of the different conformers and barriers for the corresponding interconversion (off-diagonal) at the B3LYP/maTZ level of computation for 1-(1-hydroxy-1-methylethyl)-cyclopentanol (CP-MM) and [1,1'-bicyclopentyl]-1,1'-diol (CP-CP). Barriers are given relative to the meta-stable conformer.

here the tail develops a slight shoulder and therefore two different values are used (see Tab. S36). A slightly less broad signal at 3588 cm^{-1} can be attributed to an overlap of CP-MM', CP-MMa' and CP-MMb'.

In contrast to CP-MM, CP-CP anti-periplanar arrangements are not energetically relevant as can be seen in Fig. S20. Besides 0-F (cf. Fig. S16c) it is also among the rare systems where a primed species is predicted as the most stable conformer. In this instance even the second most stable structure belongs to the primed family of conformers. Furthermore, CP-CPc and CP-CPc' form a conformational family separate from the single connected family of all other conformers, which converges to the two most stable conformers CP-CP' and CP-CPa' predicted by all tested functionals (see Tab. S18).

As can be seen from Fig. S21 the B3LYP $n_D = 4$ predictions significantly deviate from the experimental spectrum towards higher wavenumbers. However, the general signal pattern can still be identified. Similarly to CP-MM, all the bound OH modes can be found in the same wavenumber range whereas the free OH modes differ much more. This can be explained by the fact that for most CP-MM conformers (excluding CP-MMb, CP-MMb' and CP-MMc) the bound OH modes are also on the CP side. The free OH modes of CP-CP' and CP-CPa' can be identified in the experimental spectrum at 3622 cm^{-1} and 3635 cm^{-1} , respectively. However, no significant relaxation of CP-CPa' to CP-CP' takes place opposite to what the barrier indicates. This can be rationalised by the very small energy difference between the two. The band at 3656 cm^{-1} which also overlaps with water and CP-CPc can be assigned to CP-CP with some significant relaxation as indicated by the large predicted intensity. CP-CPc itself is expected to strongly relax to CP-CPc'. The neighbouring broad band at 3650 cm^{-1} can be assigned to an overlap of CP-CPa and CP-CPb. The bound OH modes of CP-CPa and CP-CPb can be assigned to 3603 cm^{-1} and the neighbouring signal at 3600 cm^{-1} to CP-CP. Somewhat less clear is the assignment of the bound OH modes of CP-CP' and CP-CPa' due to the broad nature of the signal around 3592 cm^{-1} . Given the predictions the main signal likely belongs to CP-CPa' whereas the shoulder around 3589 cm^{-1} is caused by CP-CP' with some overlap of CP-CPb' and CP-CPc'. As was already the case for the free OH vibrations this goes against the predicted intensities indicating that the energetic order of CP-CP' and CP-CPa' might be reversed. Within the expected accuracy of the energy predictions, this could easily be the case. The free OH mode of CP-CPb' could be assigned to a signal at 3630 cm^{-1} or 3628 cm^{-1} where the relative shift towards CP-CPa' fits best to the former and is tentatively assigned.

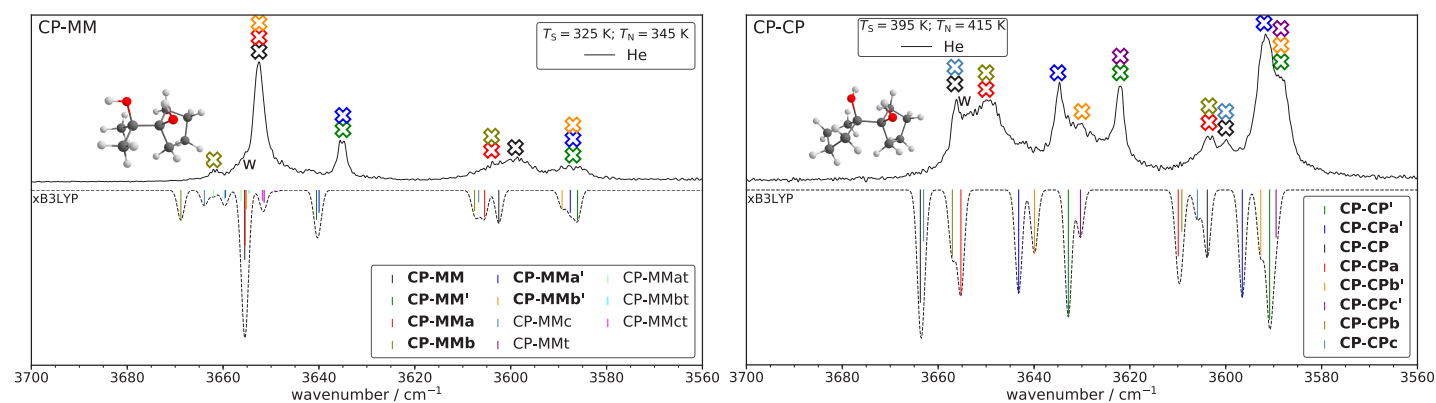


Fig. S21: Experimental spectra (plotted upwards) and simulated spectra (plotted downwards) of 1-(1-hydroxy-1-methylethyl)cyclopentanol (CP-MM) and [1,1'-bicyclopentyl]-1,1'-diol (CP-CP). Saturator (T_S) and nozzle temperatures (T_N) are provided. The simulation is based on B3LYP calculations and Boltzmann weighted according to T_N and the relative energies given in Figs. S20. xB3LYP indicates that the B3LYP fit ($n_D = 4$) was used to simulate the spectrum (see Tab. S38).

4.2 List of Assignments

4.2.1 $n_D = 0$: Primary-Primary

Tab. S22: Overview of the experimental assignments for ethane-1,2-diol (0-0) at the BP86/maTZ, PBE/maTZ, PBE0/maTZ and B3LYP/maTZ level of computation. All values are given in cm^{-1} and unscaled.

conformer \ method	Jet-Raman ^[2,21]	BP86/maTZ	PBE/maTZ	PBE0/maTZ	B3LYP/maTZ
0-0 ₁	3636	3645.72	3657.05	3833.64	3775.45
0-0 ₂	3689	3713.88	3725.04	3891.23	3824.91
0-0' ₁	3623	3622.15	3633.41	3816.42	3759.88
0-0' ₂	3656	3670.95	3681.58	3855.74	3790.80

4.2.2 $n_D = 1$: Primary-Secondary

Tab. S23: Overview of the experimental assignments for propane-1,2-diol (0-M) at the BP86/maTZ, PBE/maTZ, PBE0/maTZ and B3LYP/maTZ level of computation. All values are given in cm^{-1} and unscaled. The first 5 conformations were also correctly assigned based on the jet FTIR spectrum^[7], where the 3669 and 3673 cm^{-1} (FTIR: $\approx 3673 \text{ cm}^{-1}$) as well as the 3625 and 3629 cm^{-1} (FTIR: $\approx 3626 \text{ cm}^{-1}$) transitions were not resolved, but otherwise the wavenumbers agree within 1 cm^{-1} with the sharper Raman transitions of this work.

conformer \ method	Jet-Raman	BP86/maTZ	PBE/maTZ	PBE0/maTZ	B3LYP/maTZ
0-M ₁	3625	3628.16	3639.03	3821.58	3767.12
0-M ₂	3688	3714.99	3726.24	3892.21	3826.27
0-Ma ₁	3629	3636.24	3648.55	3826.29	3770.15
0-Ma ₂	3673	3701.71	3712.04	3879.26	3814.63
0-M' ₁	3613	3606.38	3617.06	3805.25	3752.51
0-M' ₂	3656	3672.95	3683.71	3857.74	3793.08
0-Ma' ₁	3613	3605.86	3617.55	3804.42	3751.36
0-Ma' ₂	3629	3647.71	3658.89	3833.69	3770.90
0-Mb ₁	3629	3639.39	3650.77	3828.46	3772.25
0-Mb ₂	3669	3695.24	3705.89	3875.00	3811.32
0-Mb' ₁	-	3611.53	3623.09	3809.18	3755.54
0-Mb' ₂	3651	3671.24	3681.80	3855.88	3792.13
0-Mc ₁	-	3628.99	3640.06	3819.89	3763.95
0-Mc ₂	3692	3720.96	3732.20	3896.84	3831.30
0-Mc' ₁	-	3608.11	3619.09	3804.80	3750.83
0-Mc' ₂	-	3682.61	3693.10	3868.50	3806.57

Tab. S24: Overview of the experimental assignments for 3,3,3-trifluoro-propane-1,2-diol (0-F) at the BP86/maTZ, PBE/maTZ, PBE0/maTZ and B3LYP/maTZ level of computation. All values are given in cm^{-1} and unscaled.

conformer \ method	Jet-Raman	BP86/maTZ	PBE/maTZ	PBE0/maTZ	B3LYP/maTZ
0-F ₁ '	3575	3556.32	3567.81	3763.70	3716.03
0-F ₂ '	3656	3670.23	3680.49	3854.93	3793.04
0-F ₁	3641	3657.56	3668.62	3840.91	3781.24
0-F ₂	3663	3689.60	3698.88	3865.50	3803.06
0-Fa ₁ '	-	3629.68	3640.53	3820.49	3761.41
0-Fa ₂ '	-	3640.74	3650.13	3824.05	3766.28
0-Fa ₁	-	3655.71	3666.51	3837.69	3779.72
0-Fa ₂	-	3681.01	3690.13	3858.27	3797.60
0-Fb ₁	-	3612.93	3625.19	3812.69	3761.11
0-Fb ₂	-	3715.87	3726.69	3891.07	3825.91
0-Fc ₁	-	3593.16	3606.25	3794.46	3742.13
0-Fc ₂	3689	3721.11	3731.70	3895.05	3829.66

Tab. S25: Overview of the experimental assignments for 3-butene-1,2-diol (0-V) at the BP86/maTZ, PBE/maTZ, PBE0/maTZ and B3LYP/maTZ level of computation. All values are given in cm^{-1} and unscaled.

conformer \ method	Jet-Raman	BP86/maTZ	PBE/maTZ	PBE0/maTZ	B3LYP/maTZ
0-V ₁	3629	3641.24	3652.59	3827.91	3771.35
0-V ₂	3665	3691.46	3702.23	3871.06	3806.92
0-Va ₁	3634	3648.75	3660.29	3834.03	3776.00
0-Va ₂	3661	3687.72	3697.91	3866.40	3804.02
0-Vb ₁	3629	3637.30	3648.86	3827.93	3771.75
0-Vb ₂	3661	3684.32	3695.30	3866.21	3803.63
0-V ₁ '	3596	3594.62	3605.78	3792.58	3742.23
0-V ₂ '	3613	3614.51	3625.75	3808.68	3756.92
0-Vc ₁	3629	3631.34	3642.61	3825.77	3772.25
0-Vc ₂	3687	3713.76	3725.11	3890.84	3825.05
0-Va ₁ '	3610	3613.81	3625.23	3809.88	3754.78
0-Va ₂ '	-	3628.86	3639.87	3816.49	3758.82
0-Vd ₁	3610	3605.62	3616.89	3807.06	3753.98
0-Vd ₂	3687	3714.43	3725.60	3891.03	3824.95
0-Vb ₁ '	-	3608.82	3619.86	3808.30	3756.62
0-Vb ₂ '	-	3671.75	3682.37	3856.64	3792.09
0-Vc ₁ '	-	3607.77	3619.58	3805.51	3751.54
0-Vc ₂ '	-	3645.83	3657.27	3831.97	3769.51

Tab. S26: Overview of the experimental assignments for 1-phenyl-ethane-1,2-diol (0-Ph) at the BP86/maTZ, PBE/maTZ, PBE0/maTZ and B3LYP/maTZ level of computation. All values are given in cm^{-1} and unscaled.

conformer \ method	Jet-Raman	BP86/maTZ	PBE/maTZ	PBE0/maTZ	B3LYP/maTZ
0-Ph ₁	3631	3645.47	3656.47	3831.87	3774.26
0-Ph ₂	3660	3690.68	3701.41	3868.77	3805.36
0-Pha ₁	3618	3619.68	3631.62	3816.88	3764.13
0-Pha ₂	3685	3713.07	3724.37	3890.06	3824.12
0-Ph' ₁	3605	3596.64	3607.80	3798.50	3747.35
0-Ph' ₂	-	3672.74	3683.33	3857.22	3792.99
0-Pha' ₁	3593	3593.07	3603.01	3790.04	3740.77
0-Pha' ₂	3615	3626.53	3640.16	3819.13	3764.15
0-Phb ₁	-	3644.17	3655.69	3833.90	3777.80
0-Phb ₂	-	3683.48	3694.37	3863.65	3802.65
0-Pht ₁	-	3640.44	3652.72	3830.36	3775.49
0-Pht ₂	-	3680.21	3691.29	3862.25	3798.63
0-Phc ₁	-	3607.95	3619.87	3808.78	3754.32
0-Phc ₂	-	3670.37	3681.30	3861.89	3804.30

4.2.3 $n_D = 2$: Primary-Tertiary

Tab. S27: Overview of the experimental assignments for 2-methyl-propane-1,2-diol (0-MM) at the BP86/maTZ, PBE/maTZ, PBE0/maTZ and B3LYP/maTZ level of computation. All values are given in cm^{-1} and unscaled. 0-MM* converges to 0-MM for all functionals besides B3LYP.

conformer \ method	Jet-Raman	BP86/maTZ	PBE/maTZ	PBE0/maTZ	B3LYP/maTZ
0-MM ₁	3623	3626.68	3638.36	3820.24	3766.20
0-MM ₂	3656	3686.73	3696.96	3865.41	3802.98
0-MM' ₁	3607	3596.06	3607.91	3797.89	3746.63
0-MM' ₂	3633	3656.99	3667.94	3841.91	3780.46
0-MMa ₁	3614	3620.20	3631.31	3814.86	3761.28
0-MMa ₂	3691	3720.55	3731.83	3896.41	3830.85
0-MMa' ₁	3607	3602.19	3613.00	3800.48	3748.83
0-MMa' ₂	3667	3683.52	3694.18	3869.67	3807.57
0-MM* ₁	-	-	-	-	3793.63
0-MM* ₂	-	-	-	-	3804.51

4.2.4 $n_D = 2$: Secondary-Secondary**Tab. S28:** Overview of the experimental assignments for *rac*-butane-2,3-diol (rM-M) at the BP86/maTZ, PBE/maTZ, PBE0/maTZ and B3LYP/maTZ level of computation. The values in italic correspond to those of a transition state. All values are given in cm^{-1} and unscaled.

conformer \ method	Jet-Raman	BP86/maTZ	PBE/maTZ	PBE0/maTZ	B3LYP/maTZ
rM-M ₁	3622	3622.14	3634.40	3817.45	3764.06
rM-M ₂	3673	3702.65	3713.30	3880.28	3815.68
rM-M' ₁	3607	3592.37	3603.28	3795.42	3745.41
rM-M' ₂	3630	3649.63	3660.69	3835.36	3773.07
rM-Ma ₁	3610	3618.58	3629.78	3812.01	3758.63
rM-Ma ₂	3673	3700.68	3711.18	3879.49	3816.50
rM-M ₁ [*]	-	<i>3677.32</i>	<i>3687.59</i>	<i>3865.94</i>	3804.45
rM-M ₂ [*]	-	<i>3678.30</i>	<i>3688.58</i>	<i>3866.73</i>	3806.07
rM-Ma' ₁	3598	3591.36	3602.86	3793.20	3742.00
rM-Ma' ₂	3661	3679.68	3689.93	3866.41	3805.81

Tab. S29: Overview of the experimental assignments for *trans*-cyclobutane-1,2-diol (t4-4) at the BP86/maTZ, PBE/maTZ, PBE0/maTZ and B3LYP/maTZ level of computation. All values are given in cm^{-1} and unscaled.

conformer \ method	Jet-Raman	BP86/maTZ	PBE/maTZ	PBE0/maTZ	B3LYP/maTZ
t4-4 ₁	3664	3683.34	3694.13	3863.22	3796.12
t4-4 ₂	3666	3688.05	3699.26	3869.29	3802.10
t4-4' ₁	-	3667.70	3678.21	3852.34	3787.53
t4-4' ₂	3654	3677.22	3687.75	3857.92	3790.75
t4-4 ₁ [*]	3669	3694.68	3705.96	3876.11	3808.64
t4-4 ₂ [*]	3669	3695.71	3706.95	3877.33	3809.84
t4-4t ₁	3674	3699.74	3712.81	3880.16	3813.11
t4-4t ₂	3674	3700.17	3713.23	3880.27	3813.28
t4-4at ₁	-	3670.42	3680.92	3854.04	3788.81
t4-4at ₂	-	3671.93	3682.44	3855.50	3790.17
t4-4at ₁	-	3669.83	3680.35	3854.41	3788.99
t4-4at ₂	-	3686.99	3698.12	3868.84	3801.64

Tab. S30: Overview of the experimental assignments for *trans*-cyclopentane-1,2-diol (t5-5) at the BP86/maTZ, PBE/maTZ, PBE0/maTZ and B3LYP/maTZ level of computation. All values are given in cm^{-1} and unscaled.

conformer \ method	Jet-Raman	BP86/maTZ	PBE/maTZ	PBE0/maTZ	B3LYP/maTZ
t5-5 ₁	3640	3663.73	3673.61	3845.24	3783.15
t5-5 ₂	3672	3699.31	3710.18	3878.22	3812.46
t5-5' ₁	3630	3647.30	3657.27	3833.23	3772.23
t5-5' ₂	-	3651.84	3662.41	3837.94	3775.16
t5-5t ₁	-	3673.87	3685.02	3858.58	3793.94
t5-5t ₂	-	3686.44	3697.33	3868.97	3804.49
t5-5at ₁	-	3668.26	3678.80	3853.88	3789.98
t5-5at ₂	-	3668.48	3679.02	3854.54	3790.65
t5-5bt ₁	-	3692.99	3703.67	3874.52	3810.10
t5-5bt ₂	-	3694.50	3705.18	3875.71	3811.33
t5-5* ₁	-	3691.51	3701.88	3874.71	3809.57
t5-5* ₂	-	3699.32	3709.74	3881.62	3815.94
t5-5ct ₁	-	3673.38	3683.75	3855.97	3793.82
t5-5ct ₂	-	3674.71	3685.56	3858.37	3796.09
t5-5dt ₁	-	3673.37	3684.05	3858.60	3797.72
t5-5dt ₂	-	3687.23	3697.95	3870.73	3806.20

Tab. S31: Overview of the experimental assignments for *trans*-cyclohexane-1,2-diol (t6-6) at the BP86/maTZ, PBE/maTZ, PBE0/maTZ and B3LYP/maTZ level of computation. All values are given in cm^{-1} and unscaled.

conformer \ method	Jet-Raman ^[2]	BP86/maTZ	PBE/maTZ	PBE0/maTZ	B3LYP/maTZ
t6-6 ₁	3628	3641.26	3652.51	3829.15	3773.19
t6-6 ₂	3667	3696.77	3707.04	3875.31	3810.58
t6-6' ₁	3616	3617.44	3628.32	3811.62	3757.47
t6-6' ₂	3628	3651.07	3662.02	3836.96	3774.68

Tab. S32: Overview of the experimental assignments for *cis*-cyclohexane-1,2-diol (c6-6) at the BP86/maTZ, PBE/maTZ, PBE0/maTZ and B3LYP/maTZ level of computation. All values are given in cm^{-1} and unscaled.

conformer \ method	Jet-Raman	BP86/maTZ	PBE/maTZ	PBE0/maTZ	B3LYP/maTZ
c6-6 ₁	3617	3622.59	3633.82	3817.09	3764.35
c6-6 ₂	3660	3685.55	3696.07	3867.48	3804.67
c6-6' ₁	3604	3597.46	3608.50	3798.37	3746.88
c6-6' ₂	3648	3668.51	3679.29	3854.18	3791.20
c6-6a ₁	3613	3622.49	3633.76	3814.53	3759.60
c6-6a ₂	3674	3708.07	3718.49	3883.86	3820.40
c6-6a' ₁	-	3595.44	3606.62	3793.82	3742.06
c6-6a' ₂	-	3661.34	3672.82	3850.58	3794.92

Tab. S33: Overview of the experimental assignments for *trans*-cycloheptane-1,2-diol (t7-7) at the BP86/maTZ, PBE/maTZ, PBE0/maTZ and B3LYP/maTZ level of computation. All values are given in cm^{-1} and unscaled.

conformer \ method	Jet-Raman	BP86/maTZ	PBE/maTZ	PBE0/maTZ	B3LYP/maTZ
t7-7 ₁	3623	3629.28	3640.78	3821.60	3767.20
t7-7 ₂	3664	3694.41	3704.91	3874.00	3810.41
t7-7' ₁	3604	3603.64	3614.46	3802.90	3750.79
t7-7' ₂	3626	3648.95	3659.84	3834.79	3772.60
t7-7a ₁	3608	3607.20	3619.71	3805.99	3753.97
t7-7a ₂	3672	3700.33	3710.56	3877.75	3814.09
t7-7b ₁	3626	3643.37	3653.95	3831.18	3773.92
t7-7b ₂	3662	3691.36	3702.20	3872.08	3807.95
t7-7c ₁	-	3613.37	3625.91	3812.43	3760.55
t7-7c ₂	-	3702.73	3713.37	3880.78	3816.83
t7-7a' ₁	3613	3616.06	3626.21	3811.81	3757.35
t7-7a' ₂	3626	3645.90	3656.58	3832.86	3770.54
t7-7b' ₁	-	3542.84	3555.44	3755.98	3713.52
t7-7b' ₂	-	3648.87	3660.61	3838.84	3778.25

4.2.5 $n_D = 3$: Secondary-Tertiary

Tab. S34: Overview of the experimental assignments for 2-methyl-butane-2,3-diol (M-MM) at the BP86/maTZ, PBE/maTZ, PBE0/maTZ and B3LYP/maTZ level of computation. All values are given in cm^{-1} and unscaled.

conformer \ method	Jet-Raman	BP86/maTZ	PBE/maTZ	PBE0/maTZ	B3LYP/maTZ
M-MM ₁	3617	3616.14	3628.05	3813.65	3762.43
M-MM ₂	3655	3685.10	3695.49	3864.49	3802.82
M-MM' ₁	3602	3587.07	3598.89	3791.82	3743.30
M-MM' ₂	3629	3652.74	3663.92	3838.10	3777.65
M-MMa ₁	3612	3615.20	3627.77	3810.93	3759.24
M-MMa ₂	3675	3706.86	3717.23	3883.50	3819.50
M-MMa' ₁	3602	3588.41	3599.94	3790.68	3742.04
M-MMa' ₂	3642	3660.97	3671.88	3847.90	3788.02
M-MMb ₁	3609	3613.16	3624.65	3809.51	3758.00
M-MMb ₂	3670	3699.38	3709.89	3879.34	3817.06
M-MMc ₁	-	3606.17	3618.11	3804.11	3752.54
M-MMc ₂	3659	3691.38	3701.83	3869.54	3807.82
M-MMb' ₁	-	3589.30	3600.80	3791.64	3742.62
M-MMb' ₂	-	3683.02	3693.70	3870.62	3811.32
M-MMc' ₁	-	3579.28	3591.18	3782.99	3734.63
M-MMc' ₂	-	3665.88	3676.58	3852.60	3793.67

4.2.6 $n_D = 4$: Tertiary-Tertiary**Tab. S35:** Overview of the experimental assignments for pinacol (MM-MM) at the BP86/maTZ, PBE/maTZ, PBE0/maTZ and B3LYP/maTZ level of computation. Dahlqvist *et al.* also provide gas phase values of 3603 and 3648 for MM-MM₁ and MM-MM₂ respectively^[16]. All values are given in cm⁻¹ and unscaled.

conformer \ method	Jet-Raman	FT-IR/Ar ^[16]	BP86/maTZ	PBE/maTZ	PBE0/maTZ	B3LYP/maTZ
MM-MM ₁	3605	3593	3602.50	3614.47	3802.56	3753.52
MM-MM ₂	3658	3642	3690.96	3701.29	3870.05	3808.85
MM-MM' ₁	3591	-	3575.35	3586.65	3780.29	3734.59
MM-MM' ₂	3647	-	3667.50	3678.07	3855.30	3797.67

Tab. S36: Overview of the experimental assignments for 1-(1-hydroxy-1-methylethyl)-cyclopentanol (CP-MM) at the BP86/maTZ, PBE/maTZ, PBE0/maTZ and B3LYP/maTZ level of computation. All values are given in cm⁻¹ and unscaled.

conformer \ method	Jet-Raman	BP86/maTZ	PBE/maTZ	PBE0/maTZ	B3LYP/maTZ
CP-MM ₁	3599	3599.50	3611.34	3799.09	3750.87
CP-MM ₂	3652	3685.16	3696.11	3865.84	3803.92
CP-MM' ₁	3587	3577.19	3587.61	3780.78	3734.43
CP-MM' ₂	3635	3661.94	3671.96	3847.52	3788.93
CP-MMa ₁	3604	3606.09	3617.89	3804.32	3753.83
CP-MMa ₂	3652	3685.55	3695.75	3865.35	3803.88
CP-MMb ₁	3604	3606.26	3618.07	3806.12	3755.93
CP-MMb ₂	3662	3695.95	3706.53	3876.83	3817.25
CP-MMa' ₁	3587	3577.75	3589.04	3782.63	3735.95
CP-MMa' ₂	3635	3656.60	3666.99	3844.74	3788.40
CP-MMb' ₁	3587	3581.50	3592.96	3784.56	3737.66
CP-MMb' ₂	3652	3674.55	3684.49	3861.15	3803.58
CP-MMc ₁	-	3606.08	3617.65	3804.88	3755.07
CP-MMc ₂	-	3682.92	3693.59	3867.76	3812.35
CP-MMt ₁	-	3680.06	3690.56	3861.64	3799.88
CP-MMt ₂	-	3682.31	3692.79	3866.64	3807.97
CP-MMat ₁	-	3685.30	3695.65	3865.81	3804.71
CP-MMat ₂	-	3686.95	3697.28	3868.19	3810.43
CP-MMbt ₁	-	3671.27	3685.19	3861.37	3803.03
CP-MMbt ₂	-	3681.67	3693.97	3866.65	3808.18
CP-MMct ₁	-	3668.05	3678.34	3855.42	3797.59
CP-MMct ₂	-	3669.82	3679.75	3857.51	3800.25

Tab. S37: Overview of the experimental assignments for [1,1'-bicyclopentyl]-1,1'-diol (CP-CP) at the BP86/maTZ, PBE/maTZ, PBE0/maTZ and B3LYP/maTZ level of computation. All values are given in cm^{-1} and unscaled.

conformer \ method	Jet-Raman	BP86/maTZ	PBE/maTZ	PBE0/maTZ	B3LYP/maTZ
CP-CP' ₁	3589	3587.74	3587.74	3788.65	3739.24
CP-CP' ₂	3622	3651.98	3661.97	3838.18	3781.24
CP-CPa' ₁	3592	3598.17	3607.96	3795.98	3744.95
CP-CPa' ₂	3635	3663.24	3673.45	3848.40	3791.60
CP-CP ₁	3600	3603.78	3614.73	3802.63	3752.25
CP-CP ₂	3656	3691.50	3701.98	3871.99	3812.12
CP-CPa ₁	3603	3614.68	3624.49	3809.47	3758.31
CP-CPa ₂	3650	3678.69	3688.87	3861.62	3803.65
CP-CPb' ₁	3589	3585.83	3596.53	3788.79	3741.10
CP-CPb' ₂	3630	3655.54	3665.93	3844.28	3788.30
CP-CPc' ₁	3589	3575.30	3586.78	3784.88	3737.90
CP-CPc' ₂	3622	3645.39	3655.83	3834.99	3778.72
CP-CPb ₁	3603	3610.49	3621.34	3807.47	3757.56
CP-CPb ₂	3650	3683.04	3692.90	3864.14	3805.44
CP-CPc ₁	3600	3602.53	3614.41	3803.78	3754.32
CP-CPc ₂	3656	3690.54	3701.00	3871.68	3811.43

4.3 Fit Parameters

Tab. S38: Fit parameters for B3LYP/maTZ. The parameters in parentheses of the all fit indicate which ones were varied. Fits with $h = 1.00$ can be seen in Fig. S1 for a comparison with PBE0. The sections refer to the main text.

section	n_D	h	$a2 / \text{cm}^{-1}$
4.2	0	1.01	174.6 ± 0.9
	2	1.01	182.0 ± 1.1
	4	1.01	186.1 ± 1.9
	all($a2$)	1.01	180.9 ± 1.6
	all($h, a2$)		1.008 ± 0.065
4.4	0	1.00	136.8 ± 1.0
	1	1.00	140.5 ± 0.6
	2	1.00	144.2 ± 1.1
	3	1.00	146.0 ± 0.9
	4	1.00	148.4 ± 1.7
	all($a2$)	1.00	143.1 ± 0.7
	all($h, a2$)		0.999 ± 0.028

Tab. S39: Corresponding covariance matrices for the fits shown in Tab. S38 illustrating the parameter correlation. The errors (σ) in Tab. S38 can be obtained by diagonalising the matrix and then taking the square root.

section	n_D	hh	$(a2)(a2) / \text{cm}^{-2}$	$h(a2) = (a2)h / \text{cm}^{-1}$
4.2	all($h, a2$)	0.004 248	60 706	-16.058
4.4	all($h, a2$)	0.000 771	11 033	-2.917

Tab. S40: Formally equivalent B3LYP/maTZ fits for different n_D classes, where slightly upscaling ω yields more physical anharmonicity effects for this particular functional and basis set. a_2 is given in cm^{-1} . Also shown for $h = 1.01$ and 1.00 are the results obtained for B3LYP-D3(BJ)/may-cc-pVTZ (B3LYP/mVTZ), computed with GAUSSIAN 16 (REVISION A.03), used in a recent correlation of alcohol wavenumbers^[22]. They are seen to be more or less uniformly shifted from the B3LYP/maTZ results by 20 cm^{-1} , with a slightly smaller spread as a function of n_D . This brings them somewhat closer to the ideal diatomic $h=1.00 / a_2 \approx 2x_{\text{OH,OH}}$ case, where $x_{\text{OH,OH}}$ is the diagonal anharmonicity of an OH oscillator.

$h \backslash a_2$	$n_D = 0$	$n_D = 1$	$n_D = 2$	$n_D = 3$	$n_D = 4$	comment
0.98	61.0 ± 1.1	64.7 ± 0.6	68.7 ± 1.1	70.4 ± 0.8	72.9 ± 1.4	
0.99	98.9 ± 1.1	102.6 ± 0.6	106.4 ± 1.1	108.2 ± 0.9	110.7 ± 1.5	
1.00	136.8 ± 1.0	140.5 ± 0.6	144.2 ± 1.1	146.0 ± 0.9	148.4 ± 1.7	easy to remember
1.00	159.2 ± 1.1	161.8 ± 0.6	164.9 ± 1.2	166.0 ± 0.9	168.2 ± 1.5	B3LYP/mVTZ
1.01	174.6 ± 0.9	178.4 ± 0.6	182.0 ± 1.1	183.8 ± 1.0	186.1 ± 1.9	more physical
1.01	197.3 ± 1.0	199.9 ± 0.6	202.9 ± 1.2	203.9 ± 1.0	206.2 ± 1.7	B3LYP/mVTZ
1.02	212.5 ± 0.9	216.3 ± 0.6	219.8 ± 1.2	221.6 ± 1.0	223.9 ± 2.0	

Tab. S41: Fit parameters for PBE0/maTZ. The parameters in parentheses of the all fit indicate which ones were varied. Despite the strong parameter correlation, the standard deviations for a_2 in one-parameter fits profit significantly from a lowering of h . The $h = 1.00$ fits can be seen in Fig. S1. The sections refer to the main text.

section	n_D	h	a_2 / cm^{-1}
4.2	0	0.84	-417.6 ± 1.0
	2	0.84	-410.6 ± 2.0
	4	0.84	-410.5 ± 1.8
	all(a_2)	0.84	-412.9 ± 1.3
	all(h, a_2)	0.837 ± 0.044	-423 ± 171
4.2 ($h = 1.00$)	0	1.00	198.3 ± 1.9
	2	1.00	203.5 ± 3.2
	4	1.00	201.8 ± 5.2
	all(a_2)	1.00	201.2 ± 2.0
4.4	0	0.84	-417.6 ± 1.0
	1	0.84	-414.9 ± 0.8
	2	0.84	-410.6 ± 2.0
	3	0.84	-411.3 ± 1.1
	4	0.84	-410.5 ± 1.8
	all(a_2)	0.84	-413.1 ± 0.7
	all(h, a_2)	0.835 ± 0.021	-432 ± 81

Tab. S42: Fit parameters for BP86/maTZ. The parameters in parentheses of the all fit indicate which ones were varied. The sections refer to the main text.

section	n_D	h	$a2 / \text{cm}^{-1}$
	0	0.66	-1233.3 ± 1.7
	2	0.66	-1224.7 ± 2.3
4.2	4	0.66	-1226.8 ± 1.9
	all($a2$)	0.66	-1228.2 ± 1.5
	all($h, a2$)	0.664 ± 0.040	1212 ± 147
	0	0.66	-1233.3 ± 1.7
	1	0.66	-1230.5 ± 1.2
	2	0.66	-1224.7 ± 2.3
4.4	3	0.66	-1226.8 ± 1.5
	4	0.66	-1226.8 ± 1.9
	all($a2$)	0.66	-1228.6 ± 0.8
	all($h, a2$)	0.658 ± 0.020	-1235 ± 75

Tab. S43: Fit parameters for PBE/maTZ. The parameters in parentheses of the all fit indicate which ones were varied. The sections refer to the main text.

section	n_D	h	$a2 / \text{cm}^{-1}$
	0	0.67	-1189.2 ± 1.5
	2	0.67	-1180.9 ± 2.3
4.2	4	0.67	-1183.0 ± 2.0
	all($a2$)	0.67	-1184.4 ± 1.5
	all($h, a2$)	0.670 ± 0.040	-1184 ± 147
	0	0.66	-1226.0 ± 1.7
	1	0.66	-1223.2 ± 1.2
	2	0.66	-1217.5 ± 2.3
4.4	3	0.66	-1219.4 ± 1.4
	4	0.66	-1219.5 ± 1.8
	all($a2$)	0.66	-1221.3 ± 0.8
	all($h, a2$)	0.664 ± 0.020	-1206 ± 75

5 Structures

All xyz-files (xmol) are provided in Ref. [23].

5.1 $n_D = 0$: Primary-Primary

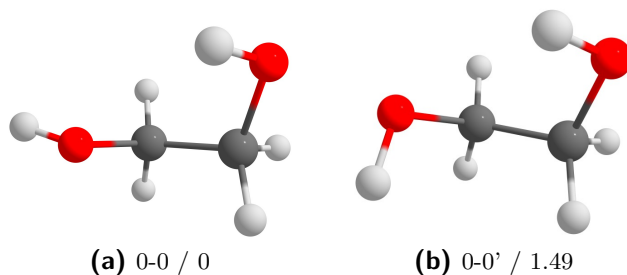


Fig. S22: Structures of ethane-1,2-diol (0-0). Relative zero-point corrected energies at the B3LYP/maTZ level are given in kJ mol^{-1} .

5.2 $n_D = 1$: Primary-Secondary

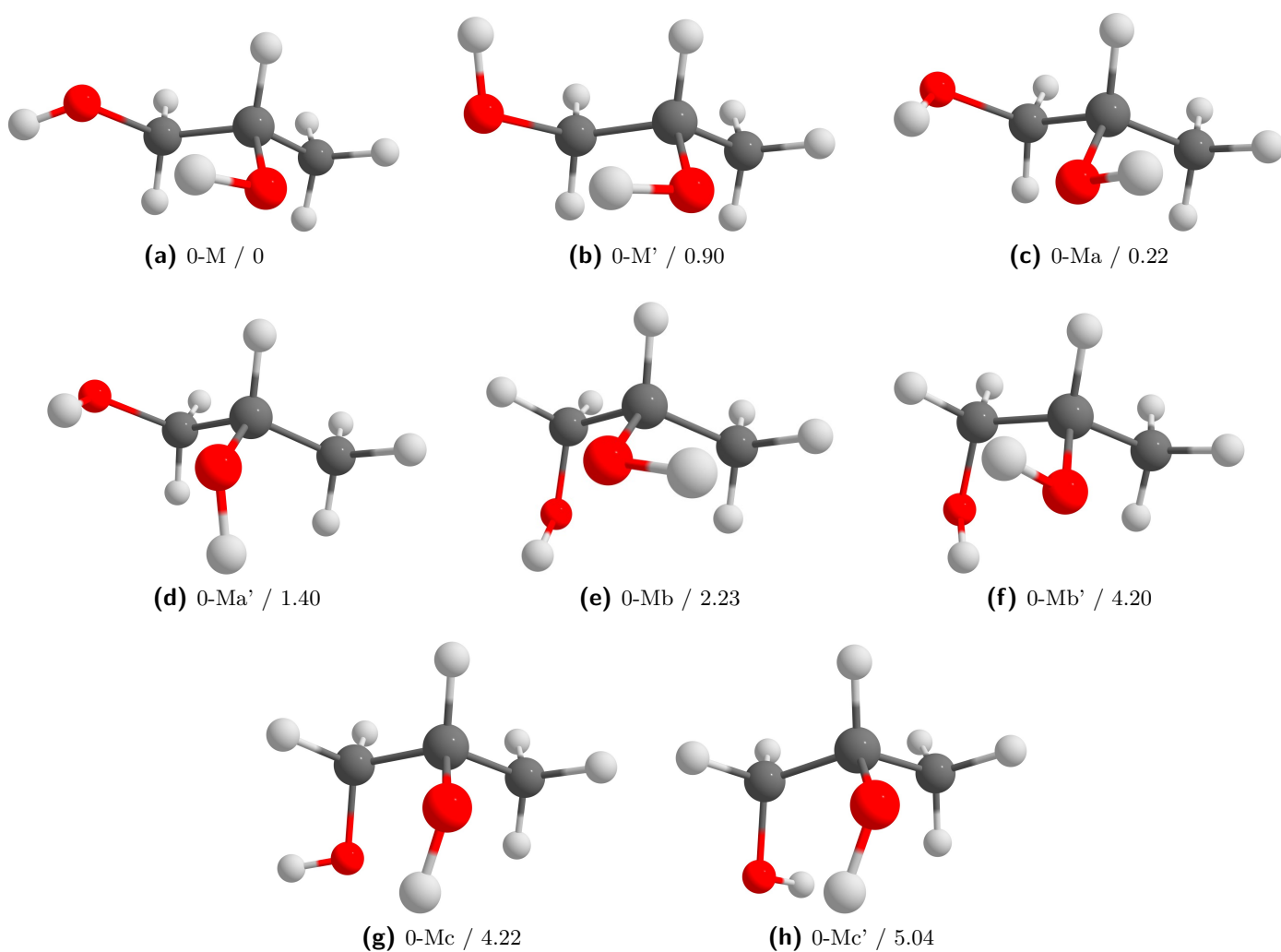


Fig. S23: Structures of propane-1,2-diol (0-M). Relative zero-point corrected energies at the B3LYP/maTZ level are given in kJ mol^{-1} .

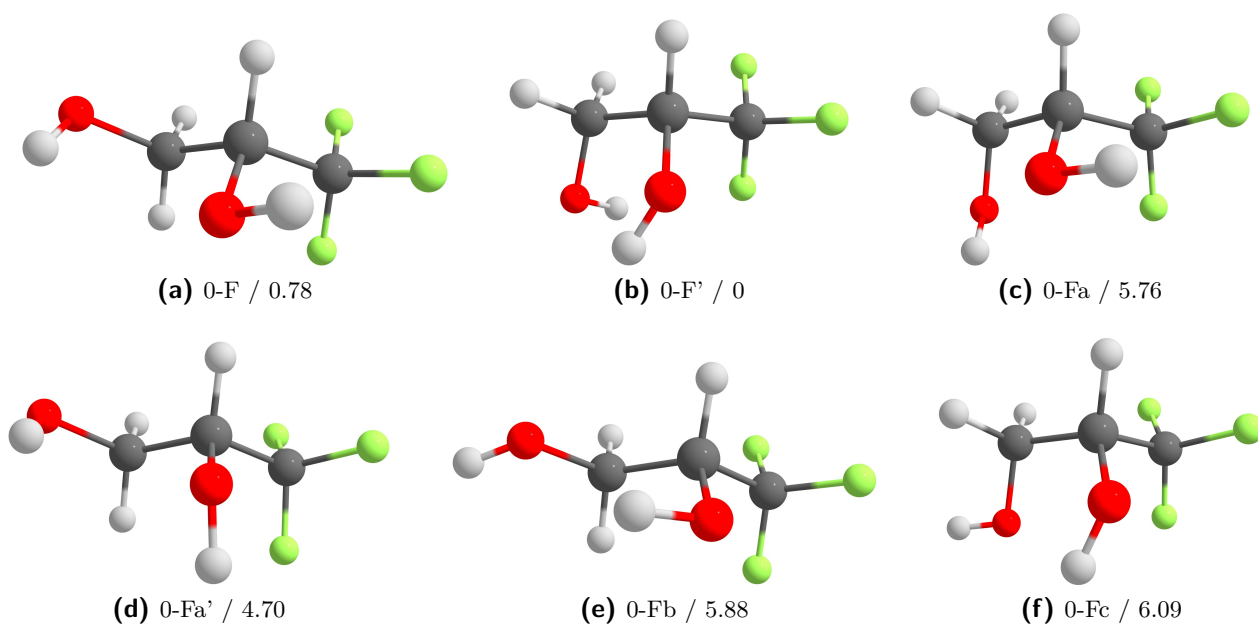


Fig. S24: Structures of 3,3,3-trifluoro-propane-1,2-diol (0-F). Relative zero-point corrected energies at the B3LYP/maTZ level are given in kJ mol^{-1} .

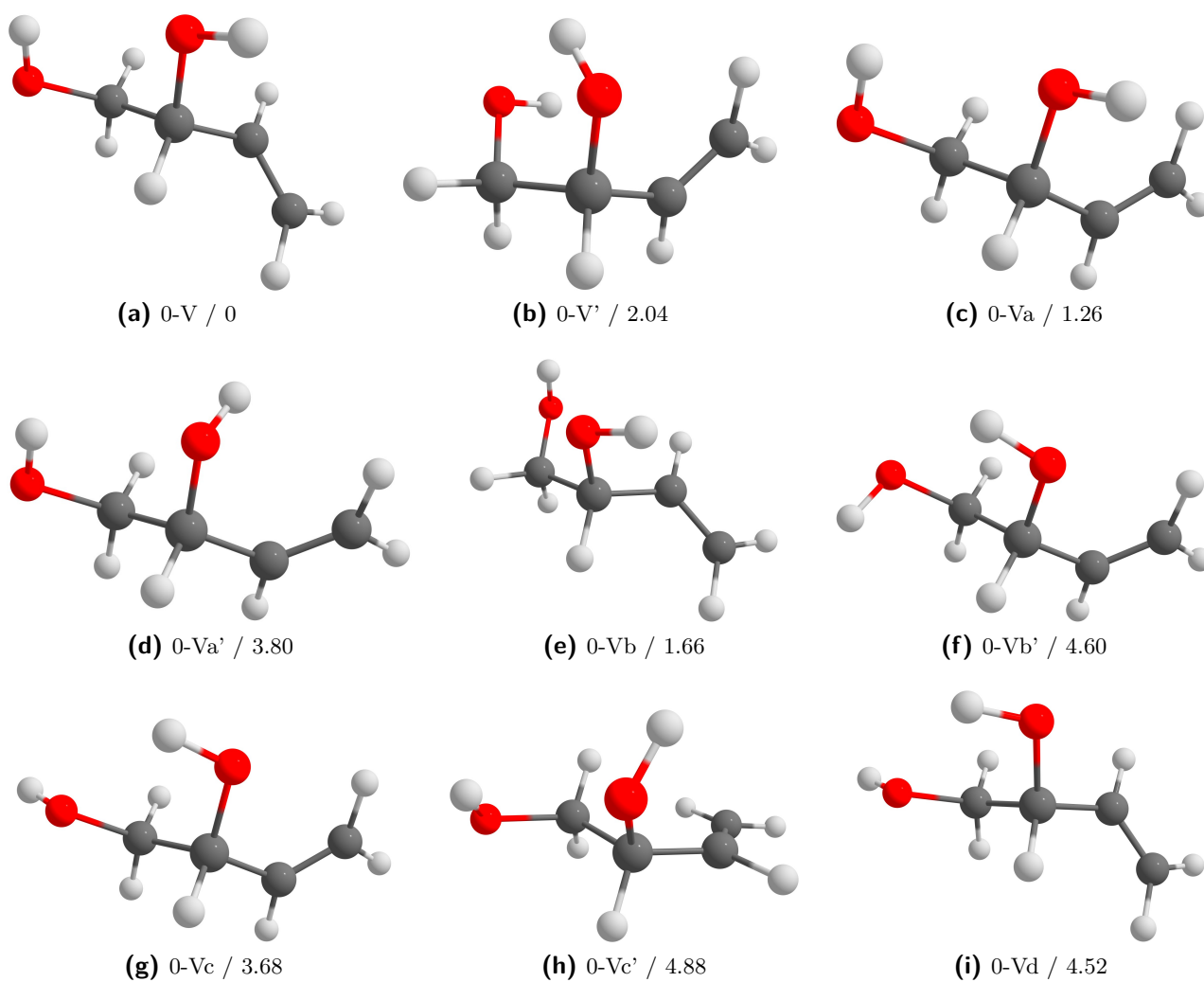


Fig. S25: Structures of 3-butene-1,2-diol (0-V). Relative zero-point corrected energies at the B3LYP/maTZ level are given in kJ mol^{-1} .

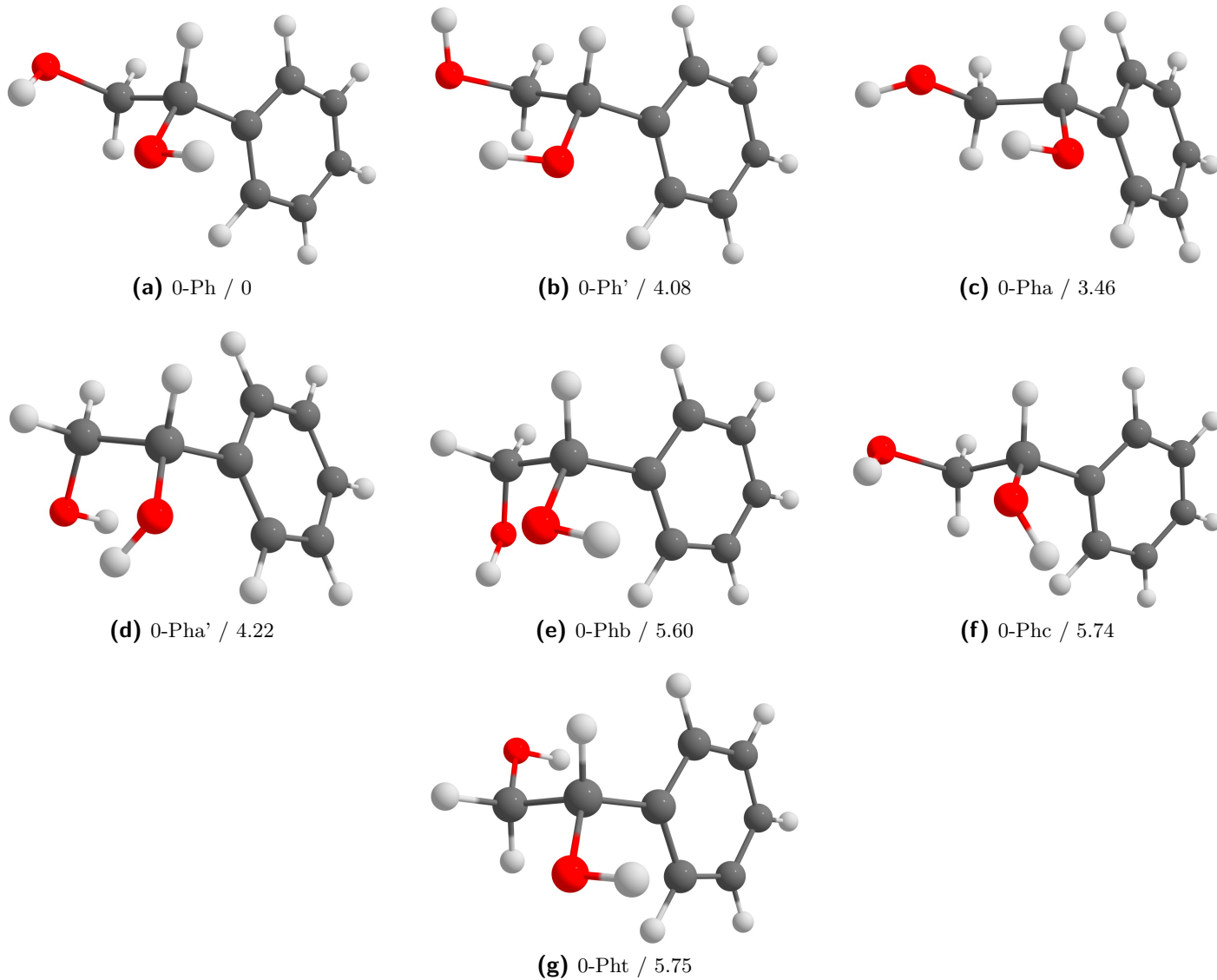


Fig. S26: Structures of 1-phenyl-ethane-1,2-diol (0-Ph). Relative zero-point corrected energies at the B3LYP/maTZ level are given in kJ mol^{-1} .

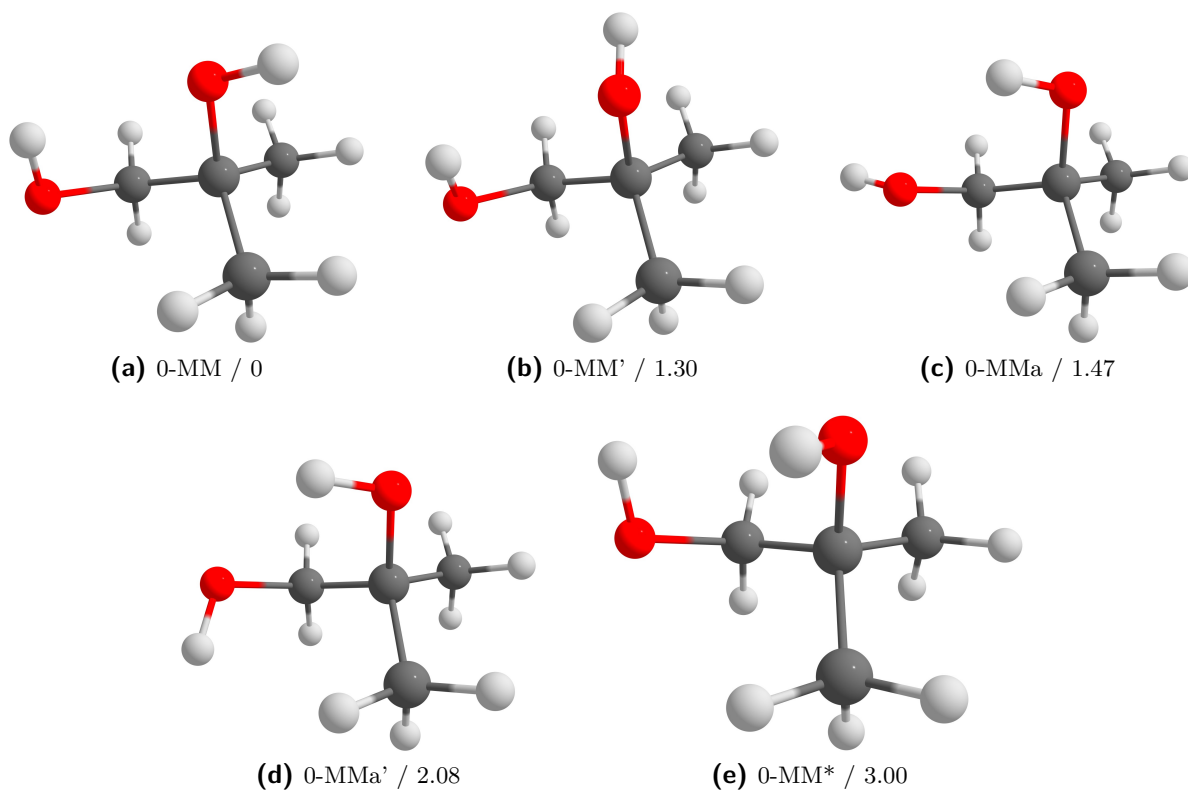
5.3 $n_D = 2$: Primary-Tertiary

Fig. S27: Structures of 2-methyl-propane-1,2-diol (0-MM). Relative zero-point corrected energies at the B3LYP/maTZ level are given in kJ mol^{-1} .

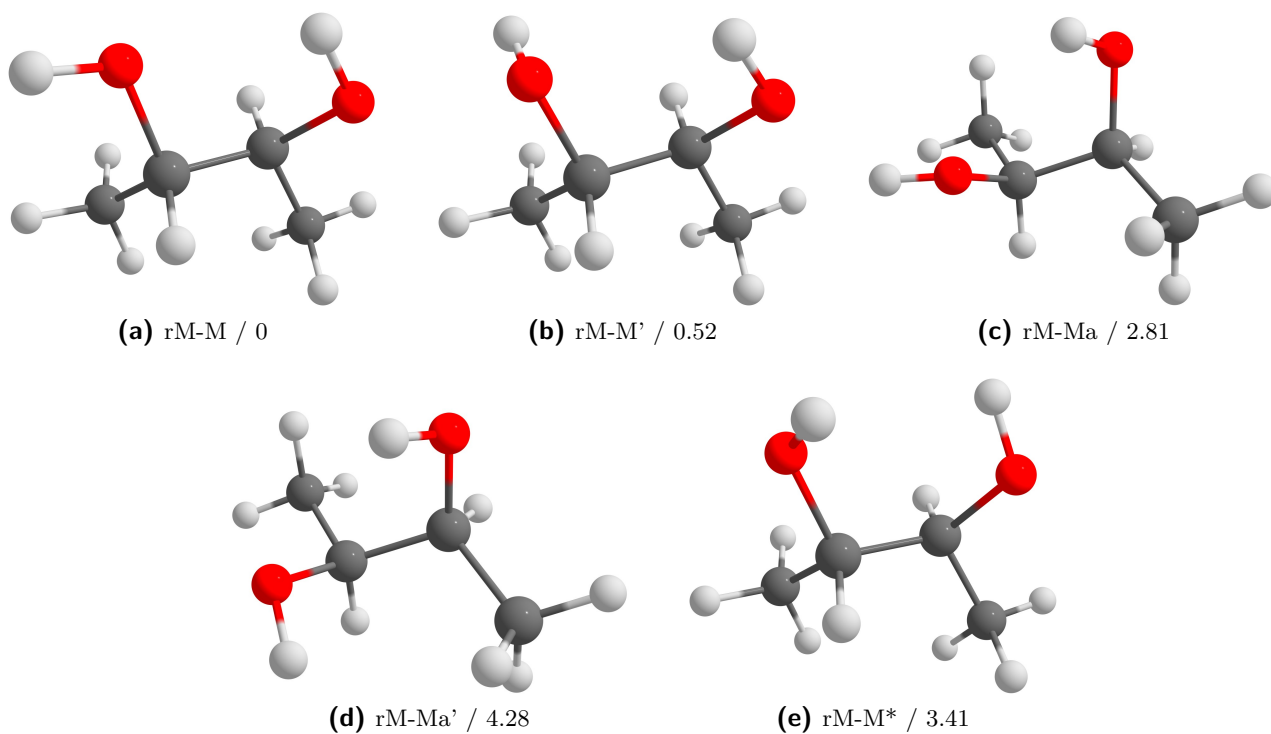
5.4 $n_D = 2$: Secondary-Secondary

Fig. S28: Structures of *rac*-butane-2,3-diol (rM-M). Relative zero-point corrected energies at the B3LYP/maTZ level are given in kJ mol^{-1} .

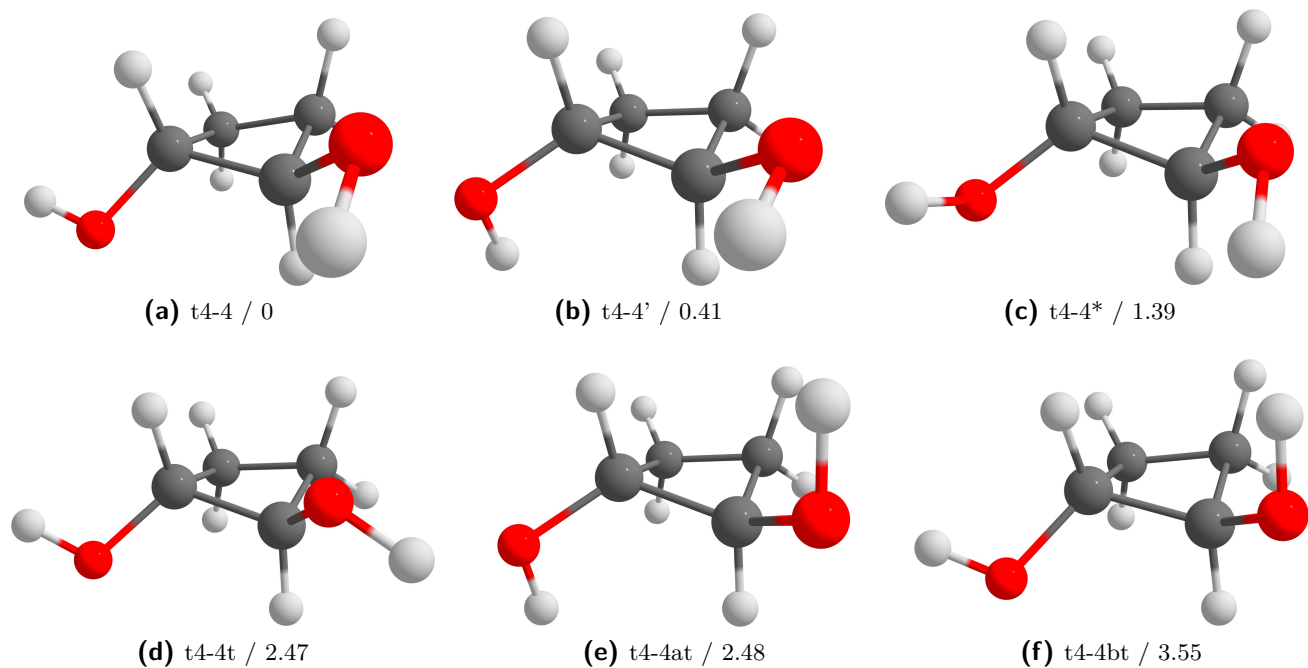


Fig. S29: Structures of *trans*-cyclobutane-1,2-diol (t4-4). Relative zero-point corrected energies at the B3LYP/maTZ level are given in kJ mol^{-1} .

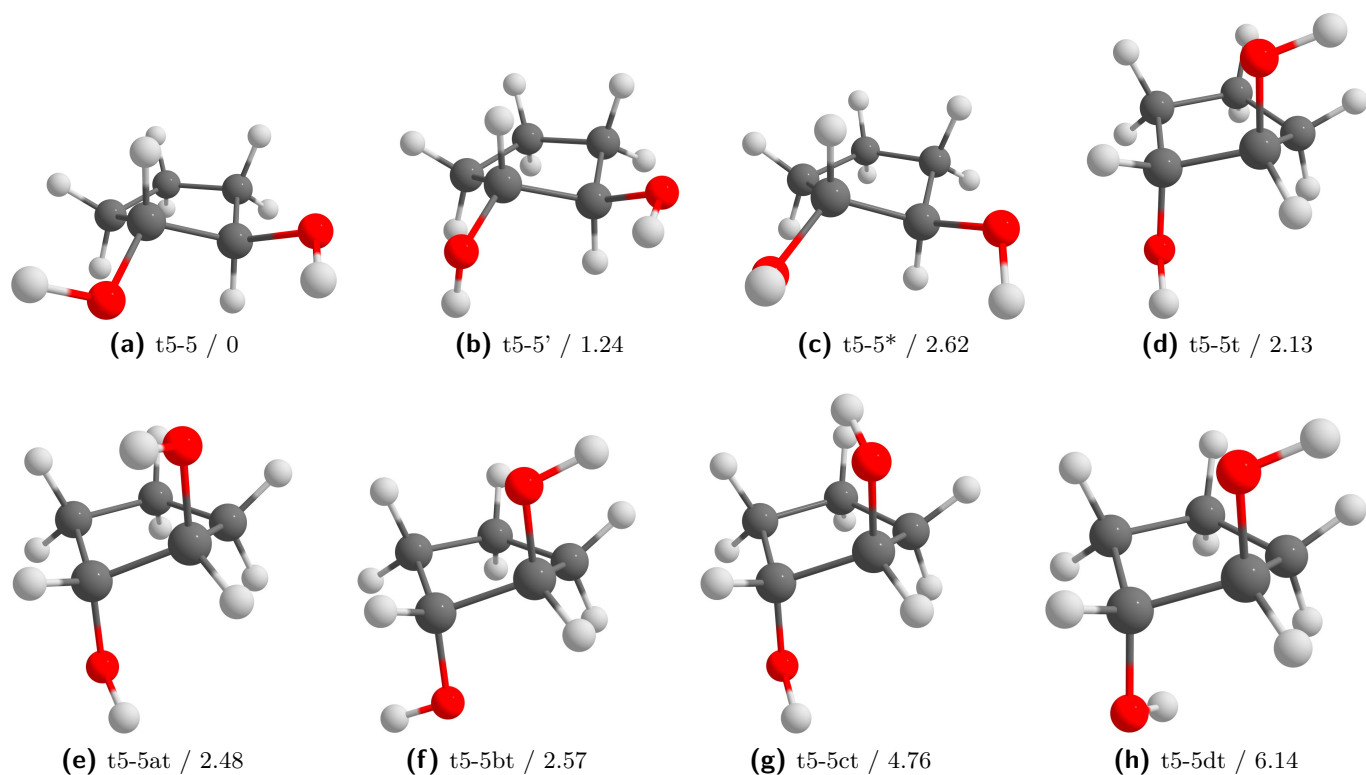


Fig. S30: Structures of *trans*-cyclopentane-1,2-diol (t5-5). Relative zero-point corrected energies at the B3LYP/maTZ level are given in kJ mol^{-1} .

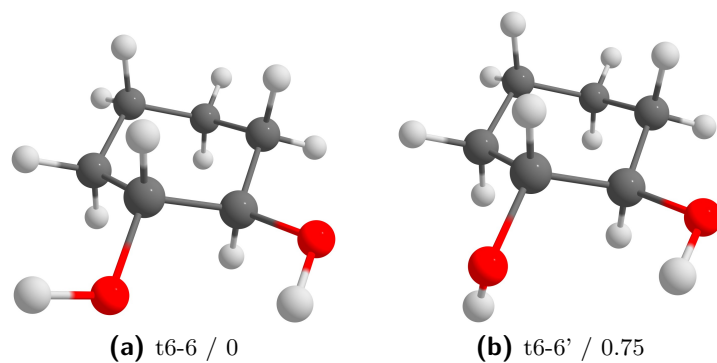


Fig. S31: Structures of *trans*-cyclohexane-1,2-diol. Relative zero-point corrected energies at the B3LYP/maTZ level are given in kJ mol^{-1} .

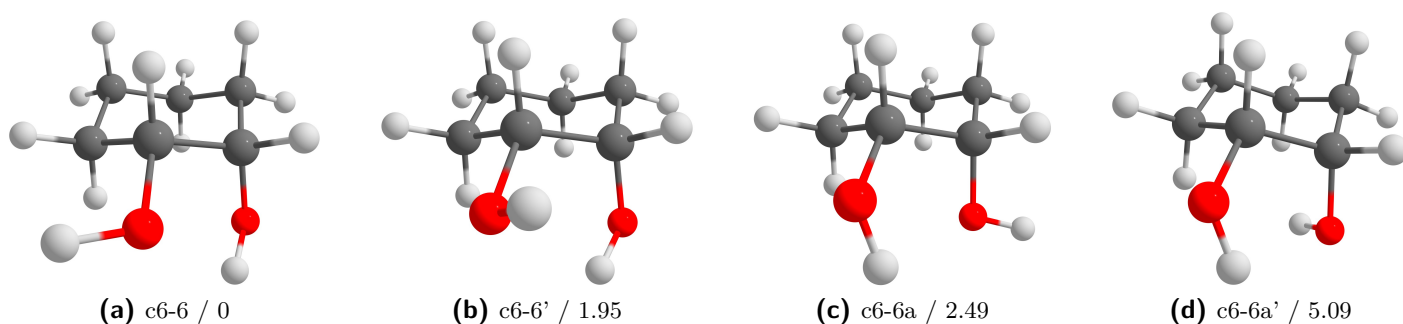


Fig. S32: Structures of *cis*-cyclohexane-1,2-diol. Relative zero-point corrected energies at the B3LYP/maTZ level are given in kJ mol^{-1} .

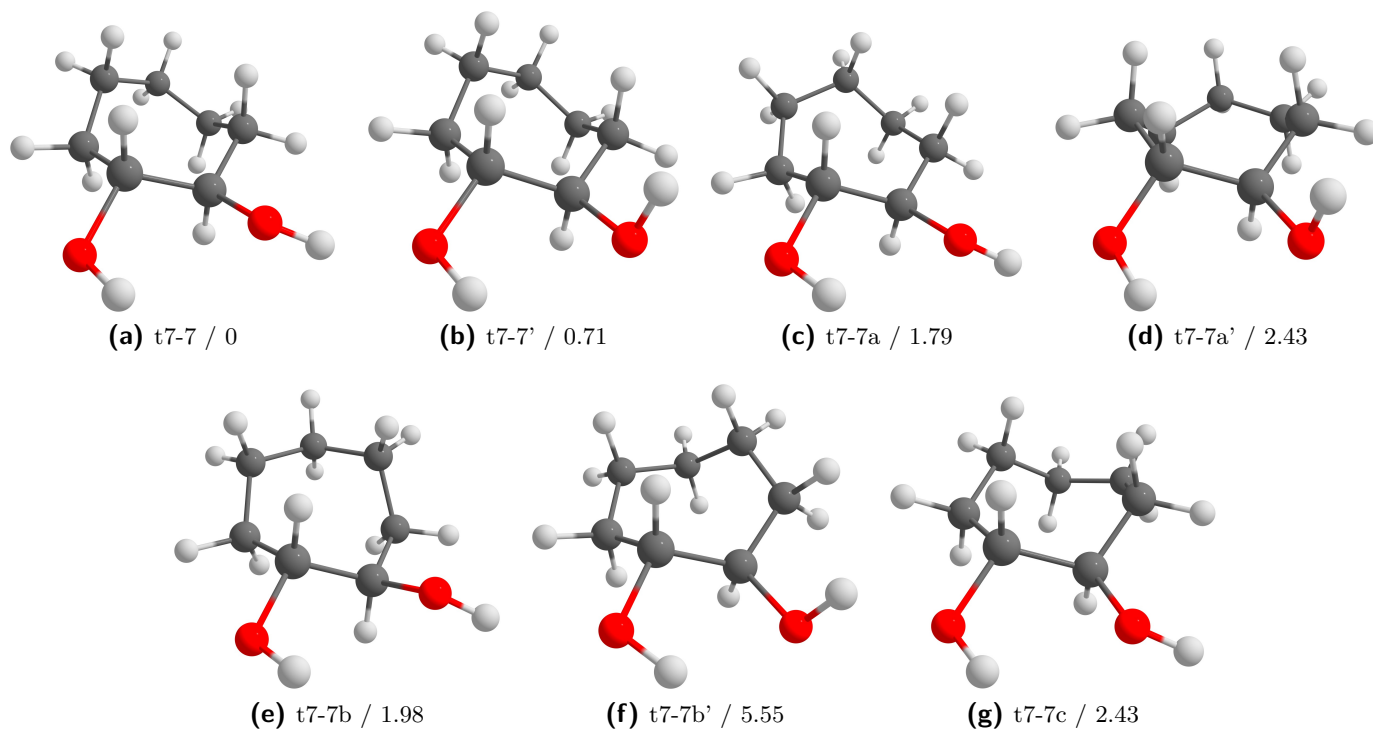


Fig. S33: Structures of *trans*-cycloheptane-1,2-diol (t7-7). Relative zero-point corrected energies at the B3LYP/maTZ level are given in kJ mol^{-1} .

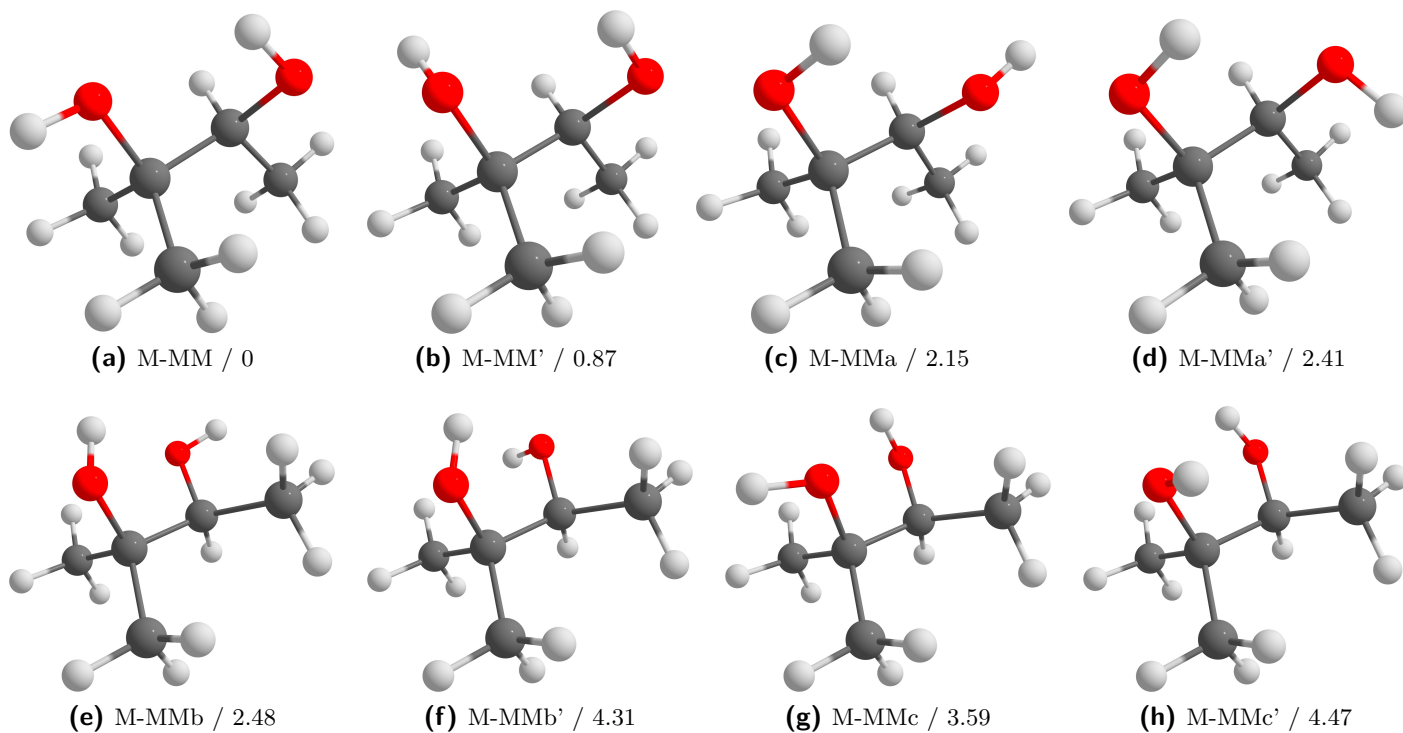
5.5 $n_D = 3$: Secondary-Tertiary

Fig. S34: Structures of 2-methyl-butane-2,3-diol (M-MM). Relative zero-point corrected energies at the B3LYP/maTZ level are given in kJ mol^{-1} .

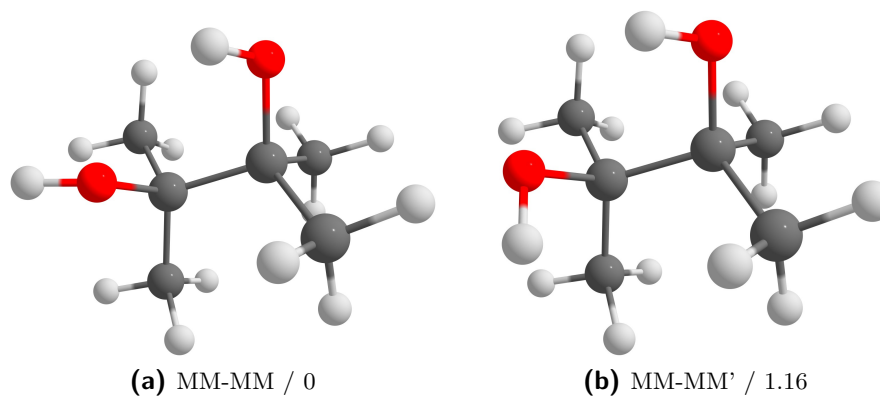
5.6 $n_D = 4$: Tertiary-Tertiary

Fig. S35: Structures of pinacol (MM-MM). Relative zero-point corrected energies at the B3LYP/maTZ level are given in kJ mol^{-1} .

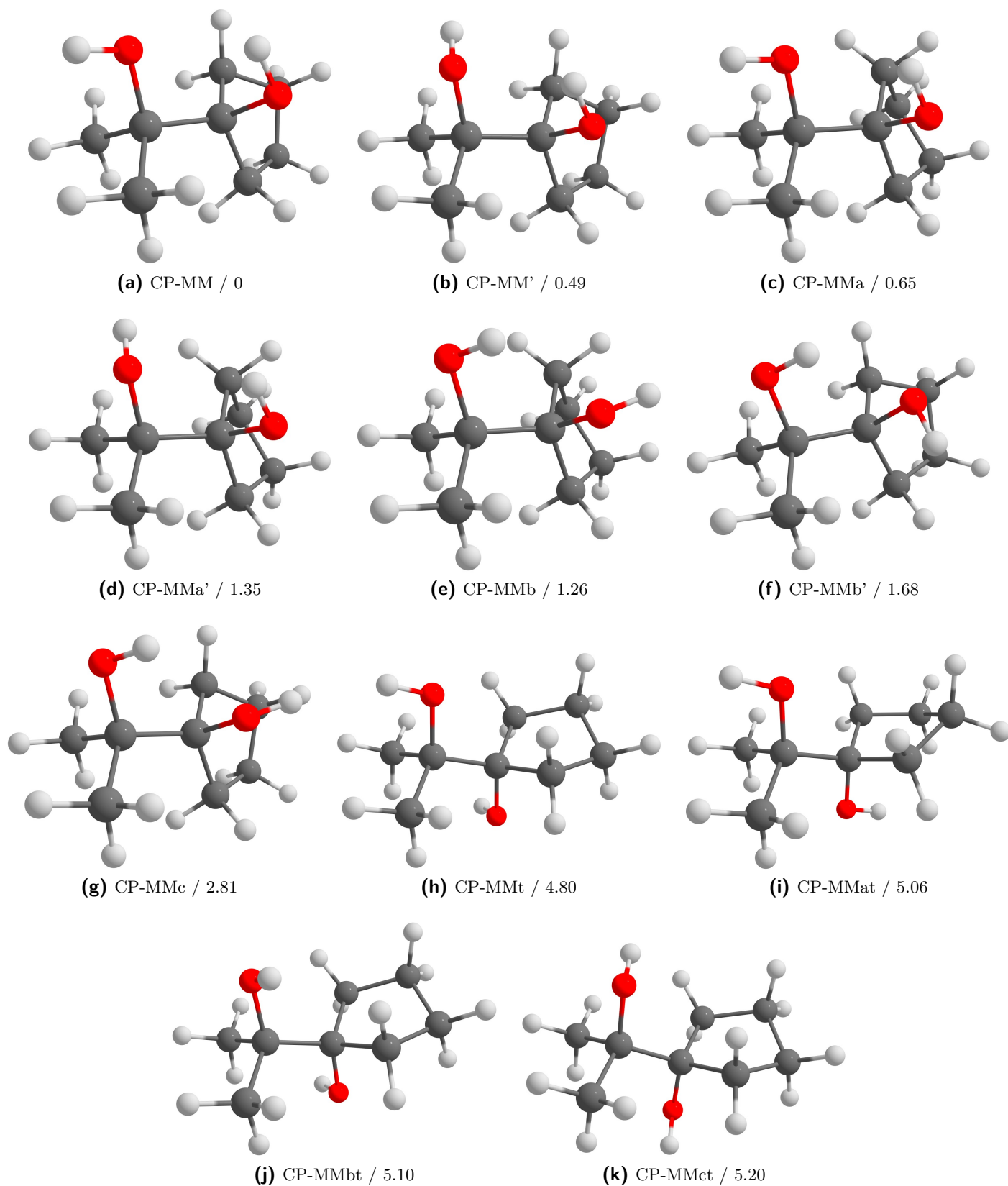


Fig. S36: Structures of 1-(1-hydroxy-1-methylethyl)-cyclopentanol (CP-MM). Relative zero-point corrected energies at the B3LYP/maTZ level are given in kJ mol^{-1} .

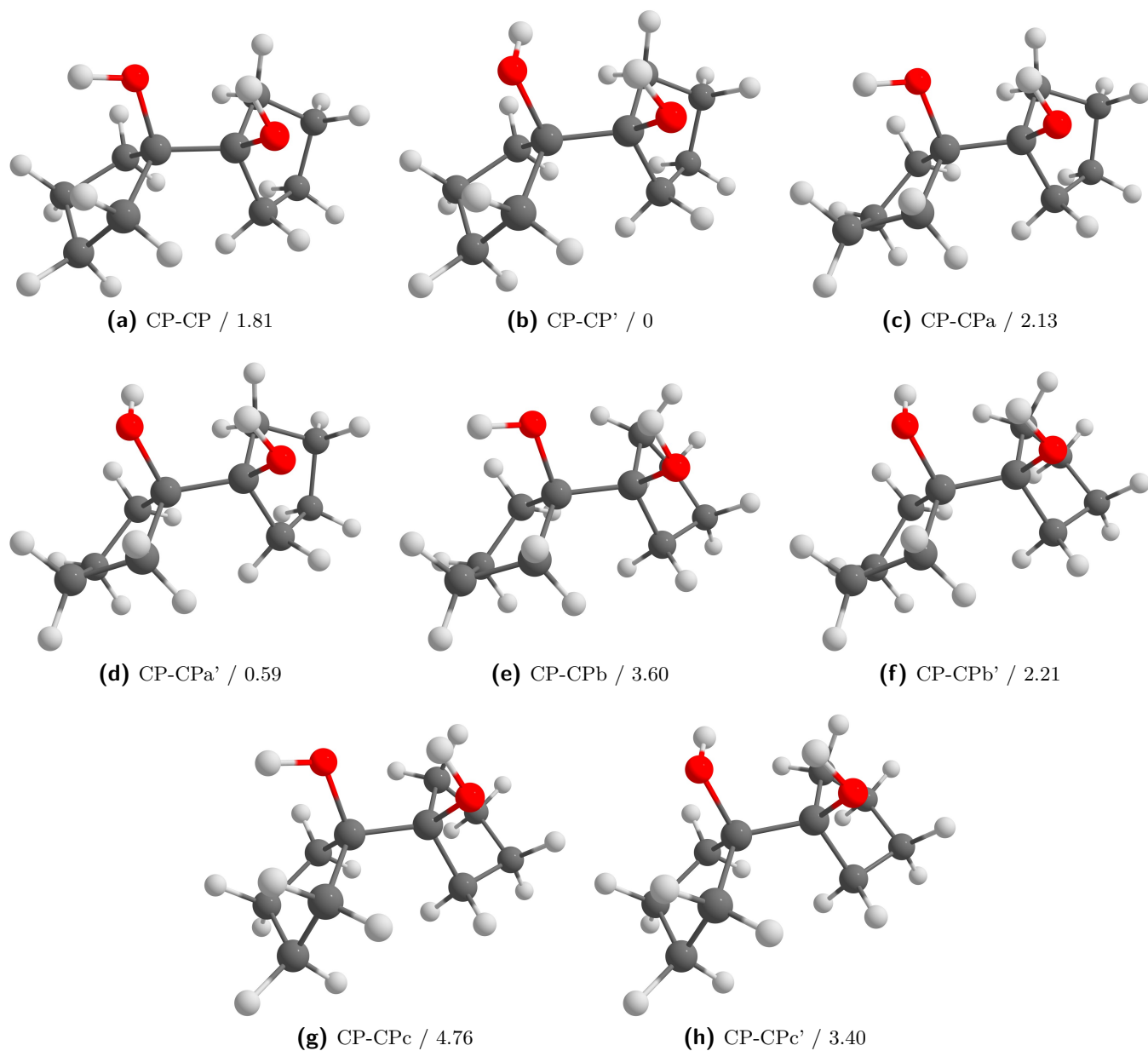


Fig. S37: Structures of [1,1'-bicyclopentyl]-1,1'-diol (CP-CP). Relative zero-point corrected energies at the B3LYP/maTZ level are given in kJ mol^{-1} .

References

- [1] B. Hartwig, M. A. Suhm, "Monomer Raman-Jet Spectra of Diols in the 3700 to 3560 Wavenumber Range", *Göttingen Research Online / Data* **2021**, version V1, DOI: 10.25625/CVAGRL.
- [2] B. Hartwig, M. Lange, A. Poblitzki, R. Medel, A. Zehnacker, M. A. Suhm, "The reduced cohesion of homoconfigurational 1,2-diols", *Phys. Chem. Chem. Phys.* **2020**, *22*, 1122–1136.
- [3] T. J. Lockley, J. I. Hearn, A. K. King, B. J. Howard, "Detection and analysis of a new conformational isomer of propan-1,2-diol by Fourier transform microwave spectroscopy", *J. Mol. Struct.* **2002**, *612*, 199–206.
- [4] F. Lovas, D. Plusquellic, B. H. Pate, J. L. Neill, M. T. Muckle, A. J. Remijan, "Microwave spectrum of 1,2-propanediol", *J. Mol. Spectrosc.* **2009**, *257*, 82–93.
- [5] J. S. Lomas, F. Maurel, A. Adenier, "1H NMR study of the hetero-association of non-symmetrical diols with pyridine; GIAO/DFT calculations on diols", *J. Phys. Org. Chem.* **2011**, *24*, 798–808.
- [6] J. S. Lomas, "1H NMR spectra of ethane-1,2-diol and other vicinal diols in benzene: GIAO/DFT shift calculations", *Magn. Reson. Chem.* **2013**, *51*, 32–41.
- [7] F. Kollipost, "Vibrational dynamics in O–H···O connected aggregates: FTIR spectroscopy from the near to the far infrared"; Original title: "Schwingungsdynamik in O–H···O-verbrückten Aggregaten: FTIR-Spektroskopie vom Nah- bis zum Ferninfraroten", PhD thesis, Georg-August-Universität Göttingen, Germany, **2015**.
- [8] B. E. Arenas, S. Gruet, A. L. Steber, M. Schnell, "A global study of the conformers of 1,2-propanediol and new vibrationally excited states", *J. Mol. Spectrosc.* **2017**, *337*, Spectroscopy and Inter/Intramolecular Dynamics in Honor of Walther Caminati - Part 2, 9–16.
- [9] W. Caminati, "Conformation and hydrogen bond in 1,2-propanediol", *J. Mol. Spectrosc.* **1981**, *86*, 193–201.
- [10] S. Vázquez, R. A. Mosquera, M. A. Rios, C. Van Alsenoy, "AB initio gradient optimized molecular geometry and conformational analysis of 1,2-propanediol at the 4-21G level", *J. Mol. Struct. Theochem* **1989**, *184*, 323–342.
- [11] L. Paoloni, G. Mazzeo, G. Longhi, S. Abbate, M. Fusè, J. Bloino, V. Barone, "Toward Fully Unsupervised Anharmonic Computations Complementing Experiment for Robust and Reliable Assignment and Interpretation of IR and VCD Spectra from Mid-IR to NIR: The Case of 2,3-Butanediol and trans-1,2-Cyclohexanediol", *J. Phys. Chem. A* **2020**, *124*, 1011–1024.
- [12] F. Wang, P. L. Polavarapu, "Predominant Conformations of (2R,3R)-(–)-2,3-Butanediol", *J. Phys. Chem. A* **2001**, *105*, 6991–6997.
- [13] A. J. Lopes Jesus, M. T. S. Rosado, M. L. P. Leitão, J. S. Redinha, "Molecular Structure of Butanediol Isomers in Gas and Liquid States: Combination of DFT Calculations and Infrared Spectroscopy Studies", *J. Phys. Chem. A* **2003**, *107*, 3891–3897.
- [14] A. J. Lopes Jesus, M. T. S. Rosado, I. Reva, R. Fausto, M. E. Eusébio, J. S. Redinha, "Conformational Study of Monomeric 2,3-Butanediols by Matrix-Isolation Infrared Spectroscopy and DFT Calculations", *J. Phys. Chem. A* **2006**, *110*, 4169–4179.
- [15] J. Paul, I. Hearn, B. J. Howard, "Chiral recognition in a single molecule: a study of homo and heterochiral butan-2,3-diol by Fourier transform microwave spectroscopy", *Mol. Phys.* **2007**, *105*, 825–839.
- [16] M. Dahlqvist, M. Hotokka, M. Räsänen, "Structures and vibrational spectra of pinacol: 1. Infrared and matrix infrared spectra of monomeric pinacol. Ab initio calculations on conformers and vibrational frequencies", *Chem. Phys.* **1998**, *229*, 137–147.
- [17] M. Olschewski, J. Lindner, P. Vöhringer, "A Hydrogen-Bond Flip-Flop through a Bjerrum-Type Defect", *Angew. Chem. - Int. Ed.* **2013**, *52*, 2602–2605.
- [18] J. S. Lomas, L. Joubert, F. Maurel, "Association of symmetrical alkane diols with pyridine: DFT/GIAO calculation of 1H NMR chemical shifts", *Magn. Reson. Chem.* **2016**, *54*, 805–814.
- [19] V. Barone, "Anharmonic vibrational properties by a fully automated second-order perturbative approach", *J. Chem. Phys.* **2005**, *122*, 014108.

- [20] M. J. Frisch, G. W. Trucks, H. B. Schlegel, G. E. Scuseria, M. A. Robb, J. R. Cheeseman, G. Scalmani, V. Barone, G. A. Petersson, H. Nakatsuji, X. Li, M. Caricato, A. V. Marenich, J. Bloino, B. G. Janesko, R. Gomperts, B. Mennucci, H. P. Hratchian, J. V. Ortiz, A. F. Izmaylov, J. L. Sonnenberg, D. Williams-Young, F. Ding, F. Lipparini, F. Egidi, J. Goings, B. Peng, A. Petrone, T. Henderson, D. Ranasinghe, V. G. Zakrzewski, J. Gao, N. Rega, G. Zheng, W. Liang, M. Hada, M. Ehara, K. Toyota, R. Fukuda, J. Hasegawa, M. Ishida, T. Nakajima, Y. Honda, O. Kitao, H. Nakai, T. Vreven, K. Throssell, J. A. Montgomery, Jr., J. E. Peralta, F. Ogliaro, M. J. Bearpark, J. J. Heyd, E. N. Brothers, K. N. Kudin, V. N. Staroverov, T. A. Keith, R. Kobayashi, J. Normand, K. Raghavachari, A. P. Rendell, J. C. Burant, S. S. Iyengar, J. Tomasi, M. Cossi, J. M. Millam, M. Klene, C. Adamo, R. Cammi, J. W. Ochterski, R. L. Martin, K. Morokuma, O. Farkas, J. B. Foresman, D. J. Fox, *Gaussian 16 Revision A.03*, Gaussian Inc. Wallingford CT, **2016**.
- [21] F. Kollipost, K. E. Otto, M. A. Suhm, “A Symmetric Recognition Motif between Vicinal Diols: The Fourfold Grip in Ethylene Glycol Dimer”, *Angew. Chem. Int. Ed.* **2016**, *55*, 4591–4595.
- [22] R. Medel, M. A. Suhm, “Predicting OH stretching fundamental wavenumbers of alcohols for conformational assignment: different correction patterns for density functional and wave-function-based methods”, *Phys. Chem. Chem. Phys.* **2021**, *23*, 5629–5643.
- [23] B. Hartwig, M. A. Suhm, “xyz Structure Files of Diols”, *Göttingen Research Online / Data* **2021**, version V1, DOI: 10.25625/VJF95K.